TOPICAL REVIEW • OPEN ACCESS

Pulsar timing arrays-challenges, and current status

OPEN ACCESS
IOP Publishing
Classical and Quantum Gravity
Class. Quantum Grav. **42** (2025) 243001 (92pp) https://doi.org/10.1088/1361-6382/ae19c2

Topical Review

Pulsar timing arrays-challenges, and current status

G M Shaifullah[1,2,3]

[1] Dipartimento di Fisica 'G. Occhialini', Università degli Studi di Milano-Bicocca, Piazza della Scienza 3, I-20126 Milano, Italy
[2] INFN, Sezione di Milano-Bicocca, Piazza della Scienza 3, 20126 Milano, Italy
[3] INAF—Osservatorio Astronomico di Cagliari, via della Scienza 5, 09047 Selargius (CA), Italy

E-mail: golam.shaifullah@unimib.it

Received 30 June 2025; revised 6 October 2025
Accepted for publication 30 October 2025
Published 16 December 2025

Abstract

This review summarises recent progress in pulsar timing array research and the current status of nanohertz gravitational wave astronomy. I outline the techniques enabling decade-long, sub-microsecond-precision timing, present results from PTA collaborations between 2023–2025, and discuss their implications for supermassive black-hole binaries, cosmological sources, and beyond-Standard-Model physics. I also highlight complimentary efforts probing the nanohertz regime.

Keywords: pulsar timing arrays, nanohertz gravitational waves, physics of galaxies, supermassive blackhole binaries, cosmology: gravitational waves

1. Introduction

Neutron stars (NSs) are the compact remnants of massive stars after core-collapse supernovae. Many are observed as *pulsars* via their periodic radio pulses. Typical NS masses lie between $\sim$0.8 and $\sim$2.4 $M_\odot$ [22, 110, 125, 381][4], with radii $\sim$10 km [295, 296, 312]. For present purposes, two broad observational families matter: long-period 'classical' pulsars and recycled millisecond pulsars (MSPs). MSPs, spun up by accretion [18, 54, 373], offer the rotational stability and narrow profiles needed for high-precision pulsar timing [264]. This technique

[4] See also www3.mpifr-bonn.mpg.de/staff/pfreire/NS_masses.html.

can be used to probe pulsars and their companions, including measuring planetary masses and orbital elements [90, 174], while also constraining the stability of atomic time standards [192, 195]. In particular, MSPs serve as laboratories for a wide range of phenomena: they trace propagation effects in the interstellar and interplanetary media, reveal the dynamics of relativistic binaries, and enable sensitive tests of fundamental physics.

One of the most exciting prospects enabled by pulsar timing is the search for nanohertz (nHz) frequency gravitational wave (GW) signals [120, 350] through pulsar timing arrays (PTAs). PTAs are formed by observing a collection of MSPs at intervals of days or weeks over decades. By precisely measuring the times of arrival (TOAs) of the pulses at each epoch of observation and identifying correlated signals among them, we can search for the signature of GWs. PTAs represent the only practical method for detecting GWs in the nHz frequency range, where sources such as supermassive black hole binaries (SMBHBs) and cosmic strings are expected to generate a stochastic GW background (GWB) [169, 228, 352]. Additionally, PTAs have the potential to detect individual GWs from nearby SMBHB systems [210, 354], as well as signals from dark matter ($\mathcal{DM}$) candidates [128].

There are currently six major regional PTAs: the Parkes PTA (PPTA) [165, 275, PPTA] in Australia, the European PTA [235, EPTA], the North American nHz Observatory for GWs [12, 209, 283, NANOGrav], the Indian PTA [307, 307, InPTA], the MeerTIME PTA [293, 370, MPTA], and the Chinese PTA [248, CPTA]. These regional PTAs are part of the international PTA (IPTA) [272, 407], which aims to combine data sets to improve sensitivity to GWs.

As mentioned earlier, PTAs monitor MSPs over long periods to take advantage of their rotational stability [154]. GWs cause a strain on space-time, which in turn modulates the TOAs of these MSPs. This effect manifests as an achromatic modulation in the TOAs, with a characteristic power spectrum that depends on the GW frequency [120, 350]. A cosmic population of nearly circularised SMBHBs would give rise to a stochastic GWB whose power spectrum follows a steep slope, with a spectral index of $\gamma = 13/3$ [323], while flatter spectral indices are expected for populations of eccentric SMBHBs or for backgrounds generated by cosmological sources [83] or from exotic sources. However, detecting these signals is challenging due to noise sources intrinsic to MSPs, interstellar medium (ISM) effects, and errors in observational models [362, 426]. For instance, interstellar plasma causes delays in radio pulses, and timing noise from MSPs can obscure the GWB signal. Other factors such as clock errors and inaccuracies in the Solar System ephemeris (SSE) further complicate detection [392]. Therefore, distinguishing the GW-induced signal from these various noise sources is a key challenge in PTA data analysis.

The hallmark of an isotropic GWB, which distinguishes it from other noise processes, are the spatial correlations between the TOAs of different pulsars, as described by the Hellings–Downs (HD) function [184]. This function predicts a unique correlation pattern based on the angular separation between pulsars, serving as a fingerprint of the GWB. However, detecting these correlations is difficult because the amplitude of the cross-correlations is small, usually below 0.25. The sensitivity of a PTA to these spatial correlations depends on several factors, including the number of pulsar pairs and their distribution in the sky [364, 386].

Ultimately, the detection of the GWB, rather than individual GW signals from SMBHBs, is expected to be the first major achievement of PTA observations [342]. While the stochastic nature of the GWB makes it difficult to identify as a coherent signal, the accumulation of data from multiple PTAs will eventually reveal the low-frequency residual power characteristic of the GWB. Recent results [9, 141, 294, 338, 423] suggest that we are approaching this milestone, although a definitive detection of the HD cross-correlations is still pending. As data sets grow and our understanding of noise sources improves, the detection of nHz GWs will provide

unprecedented insights into the population of SMBHBs and other cosmological phenomena, opening a new window into the GW universe [352, 389].

The first signs of a common-spectrum process, were presented by NANOGrav in their 12.5 year data set, although they did not observe the spatial correlations predicted by the HD function [29]. Similar results were found by other PTAs, including the PPTA and EPTA, without clear evidence of cross-correlation [93, 166]. Despite these challenges, the second data release of the IPTA (IPTA DR2), which combined the data from the three PTAs, showed stronger evidence for the common-spectrum process [21] than the individual PTAs.

These results were followed in 2023 by four PTA collaborations—NANOGrav, EPTA/InPTA, PPTA, and CPTA—reporting evidence for a HD spatially correlated process in their datasets [12, 139, 338, 423], with Bayes-factor support ranging from modest/insignificant in PPTA to significant/decisive in the remaining arrays. In 2024, the MPTA added an independent analysis based on $\sim$4.5 yr of data, again indicating strong evidence for HD correlations [294]. Taken together, the 2023–2024 releases establish a common phenomenology (quadrupolar spatial correlations with a red spectrum) but differ in strength and modelling choices; this diversity motivates the modular, comparative approach adopted below.

1.1. Scope, contributions and layout of this review

This review is designed for rapid, modular use and long-term utility. It (1) assembles a concise, pedagogical pathway from pulsar phenomenology to precision timing—dispersion, scattering, template matching, jitter, and TOA formation—culminating in a consistent notation for the timing model and residuals; (2) lays out the standard PTA inference machinery in one place—the noise taxonomy, the design–matrix representation, the Gaussian-process likelihood, and the strain→redshift→residual response (including the HD kernel)—with typical prior ranges used in practice; (3) surveys current instrumentation and public datasets (PPTA/EPTA+InPTA/NANOGrav/MPTA/CPTA/IPTA) and synthesises the 2023–2024 results indicating a common-spectrum, HD-correlated process, highlighting modelling choices and points of agreement/disagreement *without* performing a new reanalysis; and (4) offers a method-first but practice-oriented treatment of systematics that can mimic or mask a background—ephemerides, time standards, solar wind and IISM, pulse-profile/mode variability, and binary dynamics—with their entry points in the model, array-level diagnostics (monopole/dipole vs. HD), mitigation strategies, and implications for astrophysical/cosmological interpretation and near-term prospects.

Each subsection is largely self-contained, so readers can jump directly to a theme and obtain a minimally consistent summary without scanning the entire manuscript. In scope and emphasis, this work complements and extends prior PTA and GWB reviews by Manchester [272], Lommen [262], Yunes and Siemens [428], Tiburzi *et al* [393], Verbiest *et al* [409], Verbiest and Shaifullah [408], and Shannon and Cordes on timing systematics [362], as well as reviews of SMBHB populations and nHz astrophysics by Burke-Spolaor *et al* and Sesana [75, 352]. For cosmological and beyond-Standard-Model backgrounds, it interfaces with Caprini *et al* [83, 84] and recent overviews such as Bernardo and Wang [53], while providing a balanced, side-by-side comparison of PTA-inferred constraints across models.

For book-length and pedagogical treatments, see Taylor's monograph [388], the PTA chapter by Verbiest, Osłowski and Burke-Spolaor in the *Handbook of GW Astronomy* [406], the classic pulsar handbooks [264, 267], and the foundational monograph [276]. These resources provide comprehensive background; here we focus on a compact, comparative synthesis anchored to the latest PTA data.

Table 1. Summary of symbols and notation used in this review. Quantities are defined on first use.

Symbol	Meaning	Units/notes
c	Speed of light	2.9979×10^8 m s^{-1}; set $c = 1$ in some equations
G	Gravitational constant	6.674×10^{-11} m^3 kg^{-1} s^{-2}
e, m_e	Electron charge, mass	1.602×10^{-19} C; 9.109×10^{-31} kg
DM	Dispersion measure $\int n_e \, dl$	pc cm^{-3}
ν	Radio observing frequency	GHz (unless stated)
f	Fourier/GW frequency	Hz
a	Dispersion constant $e^2/(2\pi m_e c)$	4.1488×10^3 s MHz^2 cm^3 pc^{-1}
τ	Timing residual (data−model)	s
τ_{TM}, τ_{SN}, τ_{GW}	Deterministic, spin-noise, GW terms	s
Δt_{DM}	DM delay	s
τ_{sc}	Scattering broadening	s; $\propto DM^{2.2}\nu^{-4.4}$
$U(t)$	Template pulse profile	Normalized to unit area
W_{int}	Intrinsic pulse width	s
f_J	Fractional jitter amplitude	dimensionless
n	Pulses averaged per TOA	
A_X, γ_X	Amplitude, spectral index (process X)	
$P(f)$, $\Phi(f)$	One-sided PSD	s^2 Hz^{-1}
T	Design matrix (timing model)	
$B(\theta)$, N, $C(\theta)$	Process, noise, total covariances	$C = N + TB(\theta)T^\top$
Γ_{ab}, ζ_{ab}	HD correlation, pulsar separation	ζ rad/deg
$h_{+,\times}$	GW strain polarizations	dimensionless
$h_c(f)$	Characteristic GW strain	dimensionless
$\Omega_{GW}(f)$	GW energy density per ln$f$	dimensionless fraction of ρ_c
H_0	Hubble constant	67.4 km s^{-1} Mpc^{-1}
ρ_c	Critical density $3H_0^2/(8\pi G)$	kg m^{-3}
L	Pulsar distance	pc kpc^{-1}
$\hat{p}$, $\hat{\Omega}$	Unit vectors (pulsar, GW direction)	
N_p	Pulsars in array	
E_I, Q_I, J_I	EFAC, EQUAD, jitter (backend I)	dimensionless/s/s
B_I	Backend noise block	
S/N	Signal-to-noise ratio	dimensionless
Φ_{HD}	HD kernel $\frac{3}{2}x\ln x - \frac{x}{4} + \frac{1}{2}$, $x = (1-\cos\zeta)/2$	
η	Width-efficiency factor $W_{int}/\sqrt{W_{int}^2 + \Delta t_{DM}^2 + \tau_{sc}^2}$	dimensionless
B_{PTA}	Bayes factor (background vs noise)	$\log_{10} B$

The notation and symbols used in this article adopt the most commonly used ones in literature, however, to avoid confusion for readers arriving here from varying backgrounds, table 1 provides a summary of the most relevant definitions.

With this context, in the following sections I review the latest results from PTAs, starting with a review of the properties of pulsars that make them excellent detectors of nHz GWs in section 2. In section 3 I introduce the fundamental technique that enables the detection of such faint signals. There I also introduce the different sources of noise that affect pulsar observations, and the models we utilise in PTA analysis. In section 4.1 I demonstrate the effect of GWs on a set of pulsar TOAs before discussing the properties of the instruments used to collect those data and the latest PTA datasets in sections 5 and 6. In sections 5 and 7, I discuss the GW analysis, and the results obtained by each PTA before discussing the implications of those results for a background driven by astrophysical sources in section 9, from cosmological or other exotic sources in section 11. In section 14, I briefly sketch the future of nHz GWs, focusing on upcoming detection efforts before concluding in section 15.

2. Pulsars and the times of arrival of their pulses

Pulsars are rapidly rotating NSs; massive, compact objects left behind in the aftermath of the supernovae of massive stars, heavier than 8–10 times the mass of the Sun. As the core of the supernova collapses, it is believed to acquire angular momentum, setting up an initial spin which the conservation of angular momentum rapidly boosts. The core itself continues to collapse freely until it reaches a critical drip point, where the inner layers of the core become squeezed to form a quantum pasta of fundamental particles [47, 89], leaving behind a thin crust with a very small fraction of electrons and protons, enveloped in a very rare plasma-sphere.

During this collapse and the subsequent formation of the NS, embedded magnetic fields shrink and give rise to dense magnetospheres corotating with the star. These fields are so strong that they strip away electrons from the surface, forcing them into spirals along the 'frozen-in' magnetic field lines. Any residual plasma in the tenuous atmosphere is also trapped by the ordered field. The result is an environment where relativistic particles are confined, interact collectively, and can in principle give rise to coherent radiation. A diverse range of emission models have been proposed, and while a thorough review is beyond the scope of this article, a short summary of the most popular models follows in section 2.3.

While there are contentions as to the exact process for energy extraction from pulsar angular momentum, a commonly accepted one is that of magnetic dipole radiation, which occurs due to the misalignment between the pulsar's strong magnetic field and its spin axis. This misalignment, combined with rapid rotation, produces beams of radiation that sweep through space, resembling a cosmic lighthouse. When one of these beams sweeps over the Earth, the NS's pulses can be detected, and the object is classified as a pulsar. Because of their high rotational speeds and large moments of inertia, pulsars exhibit highly stable spin rates. Consequently, the recurrence of the observed pulses is extremely regular. This regularity enables a technique known as 'pulsar timing' [264], which can be used to study the various properties of pulsars and their companions, the interstellar and interplanetary media, determining planetary masses and orbital elements [90, 174], and studying the stability of atomic time standards [192, 195].

At present, no single model has achieved consensus. Curvature radiation, plasma instabilities, maser processes, turbulence, and pair discharges each capture parts of the phenomenology, but each also faces significant open issues. The challenge remains to establish a predictive and quantitative theory that can unify the diverse manifestations of radio emission across normal pulsars, MSPs, and magnetars.

Once the radio emission mechanism operates and the NS rotates nearly freely within its tenuous atmosphere, its radiation is directed into a beam that sweeps across the observer's line of sight (LOS). Each rotation results in energy loss through magnetic braking, with angular

momentum radiated away as electromagnetic emission. The signal is therefore detected as a periodic sequence of pulses, modulated by the gradual loss of angular momentum.

2.1. The discovery of pulsars

It was such a series of pulses that were first detected by Jocelyn Bell, using the Mullard Observatory's then newly built low-frequency, high-speed radio scintillation detector [187] leading to the portmanteau 'pulsars' being coined as the name by which we know such radio-bright NSs. Although NSs had been previously suggested by Pacini [313], and even explored theoretically by Gold [163], there was little evidence initially to connect these with the observations of Hewish *et al* [188]. In fact, the original proposal by Hewish and Rees modelled these objects as very rapidly pulsating white dwarfs.

However, apart from their eponymous pulses, the signal of pulsars was used almost immediately to measure the total electron content along the LOS due to the observable frequency dispersion of pulses observed across widely separated frequencies [327]. This marked the first use of pulsars as probes of other astrophysical signals of interest, in this case using the delay between the observed pulse at two frequencies to estimate the electron density of the ionised ISM.

Electromagnetic waves propagating through a cold plasma obey the dispersion relation

$$\omega^2 = \omega_{\rm e}^2 + c^2 k^2, \tag{1}$$

where the electron plasma angular frequency is

$$\omega_{\rm e}^2 = \frac{4\pi n_{\rm e} e^2}{m_{\rm e}}. \tag{2}$$

For typical astrophysical conditions ($n_{\rm e} \sim 10^{-4}$–$10^{4}\,{\rm cm}^{-3}$), the corresponding plasma frequency is $\nu_{\rm e} \equiv \omega_{\rm e}/(2\pi) \simeq 8.98\,{\rm kHz}\,\sqrt{n_{\rm e}/{\rm cm}^{-3}}$, well below usual observing bands [126]. Since $\omega_{\rm e} \ll \omega$ we may expand the group velocity,

$$v_{\rm g}(\nu) \equiv \frac{\partial \omega}{\partial k} = c\left(1 - \frac{\omega_{\rm e}^2}{\omega^2}\right)^{1/2} \simeq c\left(1 - \tfrac{1}{2}\frac{\omega_{\rm e}^2}{\omega^2}\right), \tag{3}$$

so that $1/v_{\rm g} \simeq c^{-1}\left(1 + \frac{1}{2}\omega_{\rm e}^2/\omega^2\right)$ and the frequency–dependent arrival time to a source at distance L is

$$t(\nu) = \int_0^L \frac{{\rm d}l}{v_{\rm g}(\nu)} \simeq \int_0^L \frac{{\rm d}l}{c}\left(1 + \frac{1}{2}\frac{\omega_{\rm e}^2}{\omega^2}\right) = \frac{L}{c} + \frac{1}{2c}\int_0^L \frac{\omega_{\rm e}^2}{\omega^2}\,{\rm d}l. \tag{4}$$

Using $\omega = 2\pi\nu$ and $\omega_{\rm e}^2 = 4\pi n_{\rm e} e^2/m_{\rm e}$ gives

$$t(\nu) - \frac{L}{c} \;\equiv\; \tau(\nu) = \frac{e^2}{2\pi m_{\rm e} c}\,\frac{1}{\nu^2}\int_0^L n_{\rm e}\,{\rm d}l. \tag{5}$$

Defining the dispersion measure (DM) as the line-of-sight (LOS) integral of the electron density with path length in parsecs,

$$\mathrm{DM} \equiv \int_0^L n_{\rm e}\,{\rm d}l \quad \text{with } {\rm d}l \text{ in pc and } n_{\rm e} \text{ in } {\rm cm}^{-3}, \tag{6}$$

we write the dispersive delay compactly as

$$\tau(\nu) \;=\; a\,\frac{\mathrm{DM}}{\nu^2}, \qquad a \;\equiv\; \left(\frac{e^2}{2\pi m_{\rm e} c}\right)({\rm 1pc}). \tag{7}$$

Inserting fundamental constants (Gaussian–cgs) yields the widely used numerical forms

$$a \;=\; 4.148\,808\ \mathrm{ms\ GHz^2\ cm^3\,pc^{-1}} \;=\; 4.148\,808\times10^{3}\ \mathrm{s\ MHz^2\ cm^3\,pc^{-1}}. \tag{8}$$

Accordingly, the excess dispersive delay between two observing frequencies is

$$\Delta t_{\mathrm{DM}} = a\,\mathrm{DM}\left(\nu_1^{-2}-\nu_2^{-2}\right) = \begin{cases} 4.148\,808\ \mathrm{ms\ DM}\ \left(\nu_{1,\mathrm{GHz}}^{-2}-\nu_{2,\mathrm{GHz}}^{-2}\right), \\ 4.148\,808\times10^{3}\ \mathrm{s\ DM}\ \left(\nu_{1,\mathrm{MHz}}^{-2}-\nu_{2,\mathrm{MHz}}^{-2}\right), \end{cases} \tag{9}$$

where frequencies are in GHz (top line, Δt in ms) or in MHz (bottom line, Δt in s). The small expansion parameter $\epsilon \equiv (\omega_{\mathrm{e}}/\omega)^2 \simeq 8\times10^{-11}\,(n_{\mathrm{e}}/\mathrm{cm^{-3}})\,(\nu/\mathrm{GHz})^{-2}$ justifies the Taylor series used above; searches for the ϵ^2 correction have not uncovered a significant detection [164, 398].

Historically, some authors parameterised equation (7) as $\mathrm{DM} = K\nu^2\,\tau(\nu)$ with $K = a^{-1}$ (see [273]), while the Handbook of Pulsar Astronomy adopts $a = 4.148\,808(3)$ ms GHz^2 cm^3 pc^{-1} [263]. Within a given analysis pipeline the specific choice of a (or K) is absorbed by the fitted DM; however, care is required when comparing published DMs unless the adopted convention for a (or K) is explicitly stated.

Finally, it was also relatively quickly identified that the pulses appeared to have characteristic shapes or profiles for each pulsar, and could be searched for by using Fourier transform–based analysis.

2.2. The population of NSs

Significant improvements in radio astronomy, including the ability to record data in digital formats and the development of high speed, broadband instrumentation led to a rapid growth in the number of pulsars being discovered, and a subsequent decrease in the lowest spin periods observed. This is most easily demonstrated by the figure 1, which shows the number of pulsars, of both the millisecond and classical types, as a function of time. As of the date of the preparation of this manuscript, the total number of detected pulsars is greater than ∼4300, including candidate pulsars, as defined in the ATNF pulsar catalogue.

The marked increase towards the right of the plot is due to a multiplicity of factors, including but not limited to significant improvements in the computational resources used for pulsar searching, accompanied by dramatic increases in the sensitivities of radio telescopes used for pulsar searching, as well as the introduction of new searching techniques.

It is expected that the underlying population of pulsars in the Galaxy ranges between 10 000 to 600 000, a significant fraction of which will only become visible once future telescopes such as the square kilometre array (SKA) come online towards the later half of this decade.

Pulsars display a diversity of behaviours and can be classified into several distinct groups based on their observed properties, as summarised in figure 2. The dominant population are adio pulsars (∼4300), which subdivide into slow pulsars [264] and MSPs [18, 54]. They can also be grouped into Galactic and globular cluster pulsars [79, 333, GCPs;]. The vast majority are isolated, while a smaller fraction are found in binaries with a wide range of companions, including ∼30 known double NSs [74, 147, 383, DNS;].

Depending on their radio detectability, pulsars are often classified as radio-loud or radio-quiet [291]. Radio-loud pulsars are characterised by regular pulses, though in some cases these can be intermittently interrupted or absorbed. Transient and intermittency phenomena include rotating radio transients [284, RRATs;], nulling pulsars [58, NullP;], and the handful of intermittent pulsars [234, InterP;]. A minority of objects show no confirmed radio detections

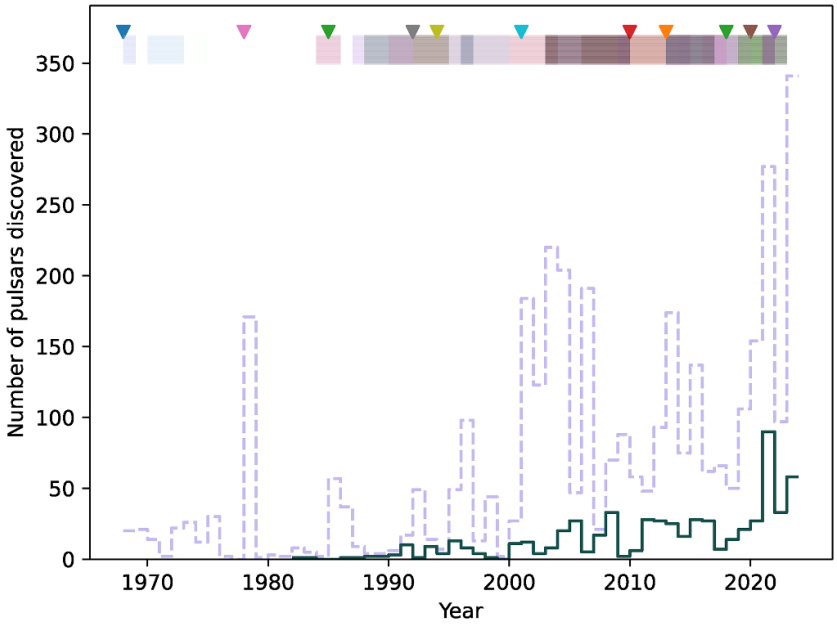

Figure 1. Plot showing the number of discovered pulsars as a function of time. The light, dashed histogram represents Classical pulsars, while the dark solid histogram shows the number of millisecond pulsars discovered per year. The coloured bars and triangles above show 41 surveys listed in the ATNF pulsar catalogue.

(NRAD), though several credible candidates for radio continuum emission exist [45], even if none are firmly established [277].

A number of pulsars are also strong high-energy sources, observed in X-rays [48] and γ-rays [6], and overlapping with rarer magneto-thermal objects such as magnetars [310], anomalous x-ray pulsars [289, AXP;], soft gamma repeaters [222, SGRs;], and thermally emitting isolated neutron stars [399, XINS;]. In these classes, irregular or transient pulses are particularly common, often linked to strong magnetic fields or to interactions with surrounding material.

The directed links in figure 2 encode both taxonomic overlap and possible evolutionary pathways—for example, spin-up in binaries producing MSPs, or magnetar-like activity connecting to high-energy subclasses.

Slow or 'classical' pulsars are typically several million years old [264, see e.g.]. They possess inherited spin periods ranging from tenths of a second to about ten seconds [274, 405], which result from the conservation of angular momentum during the core collapse of the progenitor star. Guided largely by their historical discovery, pulsars are classified by rotation rate as either 'slow' pulsars or millisecond pulsars (MSPs), where the latter rotate at rates much greater than 100 Hz and extend down to sub-millisecond periods [186]. MSPs are thought to have gained additional angular momentum through the accretion of material from a companion star [18, 54, 373]. This process produces much shorter spin periods, generally weaker magnetic fields, and greater rotational stability. These differences between slow pulsars and MSPs are commonly displayed via the P–$\dot{P}$ diagram (figure 3).

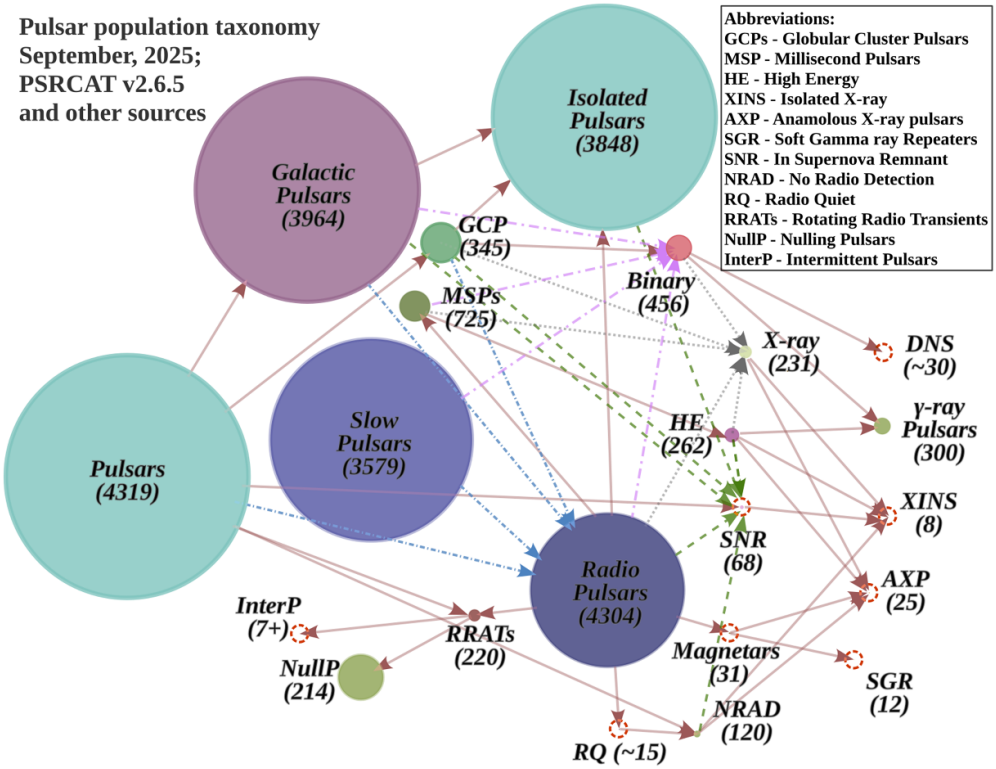

Figure 2. Directed acyclic graph (DAG) representation of the pulsar taxonomy, showing the major observational classes and their subdivisions. Node sizes are proportional to the number of known objects in each class, while edges indicate either taxonomic overlap or plausible evolutionary connections (e.g. recycling channels leading to millisecond pulsars, or magneto-thermal evolution linking magnetars and high-energy pulsars). This schematic highlights both the population statistics and the diversity of phenomenology within the pulsar zoo. The number counts correspond to the ATNF pulsar catalogue (v2.6.3) the McGill Magnetar Catalogue Paulo Freire's globular cluster catalogue and other common references[5].

2.3. The pulsar emission process

As mentioned earlier, the exact process of pulsar emission has yet to be identified. However, a number of competing models have been proposed, which I describe briefly for completeness here. *Curvature radiation models* attribute it to relativistic charges radiating coherently as they move along curved magnetic field lines. These can account for extreme brightness temperatures ($T_{\rm d} \gtrsim 10^{28}$ K), observed polarization geometry, and drifting sub-pulses, although the physical stability and origin of long-lived charge bunches remain uncertain, and nonlinear plasma processes are required [287, 299, 345].

[5] ATNF pulsar catalogue: www.atnf.csiro.au/research/pulsar/psrcat/, McGill Magnetar Catalogue: www.physics.mcgill.ca/∼pulsar/magnetar/main.html; Globular Cluster catalogue: www3.mpifr-bonn.mpg.de/staff/pfreire/GCpsr.html.

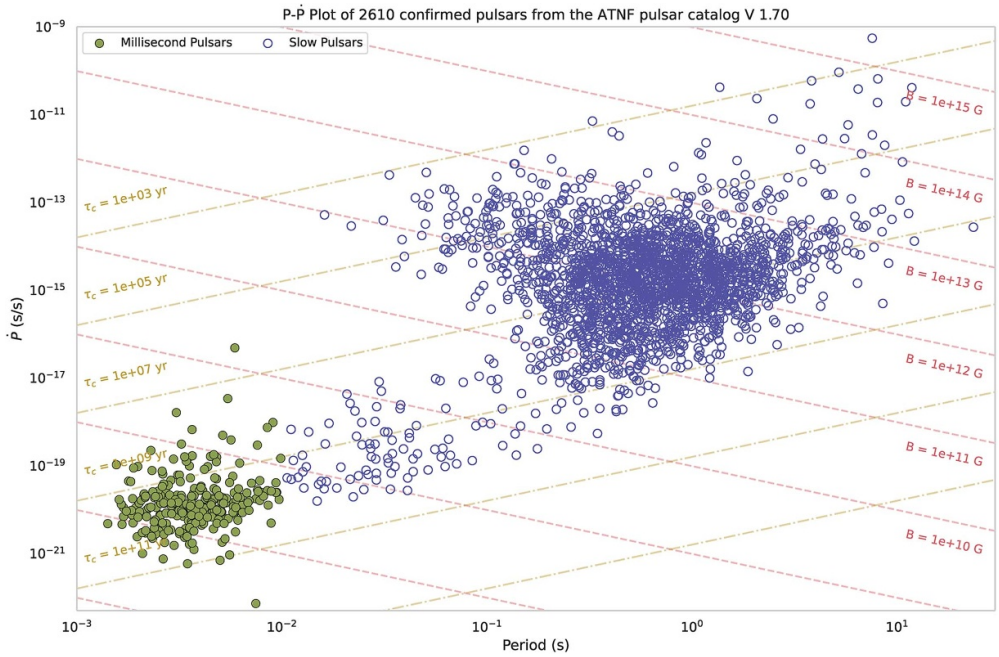

Figure 3. A comparison of slow pulsars and millisecond pulsars. Slow pulsars are typically several million years old and have spin periods ranging from tenths of a second to about ten seconds. In contrast, millisecond pulsars have much shorter spin periods, often in the millisecond range, and generally weaker magnetic fields.

Plasma-instability models invoke beam–plasma interactions that excite Langmuir waves, which through modulational instability form solitons that radiate curvature emission or convert into escaping modes [31, 287, 288]. They provide a natural route to bunch formation and are compatible with emission altitude constraints, but mode conversion into observable radiation has not yet been demonstrated quantitatively, and growth rates are sensitive to uncertain plasma parameters.

Cyclotron and Cherenkov maser models instead rely on resonant beam–plasma interactions in the outer magnetosphere, where negative absorption can amplify X-mode radiation. These mechanisms are attractive for explaining high-altitude or off-pulse emission, giant micropulses, and auroral-like features [27, 223, 288]. However, they often require finely tuned plasma distributions, tend to predict narrowband spectra, and may not easily reproduce the broadband emission seen in most pulsars.

Another proposal is the *strong plasma turbulence* model, where nonlinear Langmuir turbulence can lead to soliton collapse, producing nanosecond-scale bursts. This mechanism is strongly supported in the Crab pulsar, where nanoshot timescales align with theoretical predictions [177, 418]. Its relevance to the broader pulsar population, however, remains uncertain, since the extreme turbulence required has not been clearly identified in ordinary pulsars.

Finally, *unsteady pair-discharge models*, supported by recent particle-in-cell (PIC) simulations, suggest that time-dependent pair creation in gaps can directly launch coherent O-mode waves [322]. This approach links emission to the same pair-production physics that governs global magnetospheric dynamics, and PIC studies reproduce GHz frequencies, polarization, and luminosities broadly consistent with observations. Nonetheless, such simulations remain

computationally limited, with scaling relations and extensions to fully realistic 3D conditions still lacking.

These mechanisms are relevant not only for normal pulsars but also for MSPs, whose weaker fields require alternative pair-creation channels [178], and for magnetars, where transient pair cascades triggered by magnetospheric twists can produce radio emission even beyond the conventional death line [101, 222, 303].

2.4. Pulse emission and profiles

As pulsars rotate, their beamed radio emission sweeps over the Earth, and can be measured as a rapidly varying electromagnetic field by radio telescopes. The one-dimensional profile of intensity is called a *pulse*. The pulse can display long term variations such as those induced by a relative change in the viewing geometry, or short term variations linked to process described earlier or due to scattering by the ISM. Further, the profile can also display variations arising from both the influence of companions, or the effect of nutation and precession, slowly altering the angle at which the LOS meets the beam. Finally, at a granular level, profiles can also be decomposed into a number of microstructures [236, 321], including features such as drifting sub-pulses [46, 127, 419]. Such pulse-to-pulse variations can be effectively modelled as shot noise processes, which when averaged over several rotations modify each average profile as well.

Since each individual pulse is an observational trace through the magnetic field and the trapped ion distribution, and the strong magnetic fields of pulsars imply that at relatively high altitudes this magneto-ionic configuration is largely frozen in, averaging on a number of successive pulse averages to a mean or average profile, which is the time averaged global configuration.

From the standpoint of precision timing, magnetars—with their extremely high surface magnetic fields ($B \sim 10^{14} - 10^{15}$ G)—are generally excluded because their radio emission is frequently intermittent or transient, their average profiles and polarisation properties undergo pronounced evolution across both time and frequency, and their long rotation periods with broad duty cycles limit attainable TOA precision for fixed dwell times; in addition, many reside in complex environments (e.g. supernova remnants/H II regions) that impose large and sometimes variable dispersion and rotation measures, together with strong multi-path scattering. Similarly, classical (non-recycled) or slow pulsars are not preferred for high-precision applications: their longer spin periods and typically wider beams yield poorer radiometer-limited precision, their profiles often evolve strongly with frequency and may exhibit magnetospheric mode changes, and sight lines concentrated toward the Galactic plane tend to suffer enhanced scattering. These considerations motivate a focus on recycled MSPs with short P, narrow and stable average profiles, and comparatively clean lines of sight.

Figure 4 shows example of the variability of the pulse profile of PSR J1713+0747, one of the most precisely timed PTA MSPs. Note especially the small *range* of fluctuations over almost ∼2500 days in the right panel, as also the fact that high sensitivity observations are now capable of detecting fluctuations both within each observation (jittering in the left panel) and temporal profile variations.

Given such high observed stability, we can model each observed pulse as the sum of Gaussian components:

$$U(t) = \sum_{k=1}^{N_c} S_{\max,k} \exp\left(-\frac{(t-\mu_k)^2}{2\sigma_k^2}\right), \tag{10}$$

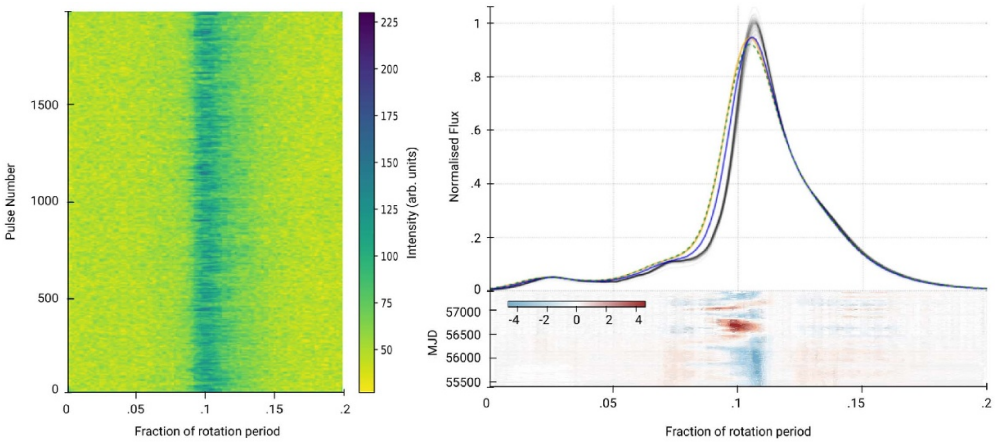

Figure 4. The stability of the pulse profile of PSR J1713+0747, a millisecond pulsar. The left panel demonstrates the short-term (or pulse-to-pulse or single pulse) variability that occurs per rotation. Despite these variations, the centroid of the intensity peak, represented by the dark blue regions, lies within a window of $\ll \pm 1 \times 10^{-6}$ fractional phase, corresponding to pulse-jitter $\simeq$45 ns [315]. The sum of several thousands of rotations recorded at each observing epoch lead to each of the gray average profiles plotted in the top right panel. These profiles, taken from the NANOGrav 11 year data release [28], are typically extremely stable. The bottom panel shows the variation of the profile mapped using units of standard deviation of the average noise in profiles, as a function of the observing epochs. The standard deviation is calculated using the signals in the phase bins where the pulse of the profile is not detected. Epochs when the profile showed significant deviations are marked with yellow, green and blue lines [69]. The composite figure is made from plots which originally appear in [69, 315].

where N_c is the number of Gaussian components [237, typically fewer than 10], $S_{\max,k}$ represents the peak intensity of the k-th Gaussian component, μ_k is the centre of the component, and σ_k is its standard deviation. Let us assume this is the template of the observed profiles.

If the voltage time-series collected by the receiver can be timestamped using a high precision local time standard, the group of photons of the profile can be associated with the time at which they 'arrived' at the telescope. Assuming a fiducial model in which the template is assigned a reference time, the TOA for any given observation can then be calculated by counting the number of rotations that would separate the template and the observed pulse, assuming the only shift required to align the template and the profile is an integer number of rotations and a small offset that can be calculated via the Fourier cross-correlation method [384]. If $\Delta t \ll P$ and neglecting second-order terms; the timing offset Δt is determined by minimizing the phase difference between the observed profile and the template:

$$\Delta t = \frac{1}{2\pi} \frac{\sum_f w(f) \cdot f \cdot \mathrm{Im}\left[\tilde{P}(f)\,\tilde{T}^*(f)\right]}{\sum_f w(f) \cdot f^2}, \tag{11}$$

where $w(f)$ is a weighting function based on the S/N of each harmonic, Im$[\cdot]$ is imaginary part of the cross-correlation, $\tilde{P}(f)$ is the Fourier transform of the observed profile and $\tilde{T}^*(f)$ is the complex conjugate of the Fourier transform of the template.

At any given epoch, the total observed profile $S(t)$ consists of the scaled sum of the Gaussian components, ambient noise, and a constant baseline offset:

$$S(t) = \hat{g}U(t - t_{\rm a}) + n(t) + N_s, \tag{12}$$

where $\hat{g}$ is a scaling factor for the pulse template of equation (10), $t_{\rm a}$ is the pulse arrival time, N_s represents the baseline noise, and $n(t)$ accounts for small noise fluctuations. When expanded around the estimated arrival time $\hat{t}_{\rm a}$ of the group of photons that make up the pulse, the observed signal becomes:

$$S(t) = \hat{g}U(\tau) + \Delta g U(\tau) - \hat{g}\tau U'(\tau) + \hat{N}_s + \Delta N_s + n(\tau), \tag{13}$$

where $\tau = t - \hat{t}_{\rm a}$ is the timing residual, $\Delta g = g - \hat{g}$ represents a small deviation in the scaling factor, and $\Delta N_s = N_s - \hat{N}_s$ reflects a deviation in the baseline noise. Here, $U'(\tau)$ denotes the derivative of $U(\tau)$ with respect to τ. The timing residual τ is estimated by minimizing the mean squared error between the observed signal and the template, yielding:

$$\tau \approx \frac{\int U' n \, d\tau}{\hat{g} \int (U')^2 \, d\tau}. \tag{14}$$

The uncertainty in the arrival time, $\sigma_{t_{\rm a}}$, depends on the noise variance σ_n^2 and is given by:

$$\sigma_{t_{\rm a}} = \frac{\sigma_n / \hat{g}}{\left[\int (U')^2 \, d\tau\right]^{1/2}}. \tag{15}$$

Beyond these effects, both dispersion and scattering in the ISM also affect the observed pulse profile and must be accounted for in the noise budget. Due to ISM turbulence the instantaneous value of DM as defined in equation (6) fluctuates around a mean, and this can further degrade the pulse sharpness and correspondingly, the TOA precision. Rearranging equation (9); we can obtain an expression for the error in the dispersion value of ΔDM, which would introduce a frequency-dependent smearing, with a smearing time $\Delta t_{\rm DM}$ across a bandwidth Δf, given by:

$$\Delta t_{\rm DM} = 8.3\,{\rm ms} \cdot \frac{\rm DM}{f_{\rm c}^3} \cdot \Delta f, \tag{16}$$

where DM is in units of pc cm^{-3}, $f_{\rm c}$ is the centre observing frequency (GHz), and Δf is the bandwidth (MHz). This dispersion-induced smearing broadens the pulse and reduces its sharpness, lowering the observed peak intensity $S_{\rm max}$.

Scattering, which arises from Kolmogorov turbulence in the ISM, adds an exponential tail to the pulse profile. The scatter broadening function $G(t)$ is given by:

$$G(t) = \frac{1}{\tau_{\rm sc}} \exp\left(-\frac{t}{\tau_{\rm sc}}\right) H(t), \tag{17}$$

where $\tau_{\rm sc} \propto {\rm DM}^{2.2} f^{-4.4}$ is the scattering timescale and $H(t)$ is the Heaviside step function ensuring $G(t)$ is non-zero only for $t \geqslant 0$. The combined effects of dispersion and scattering can be described by convolving the intrinsic pulse $U(t)$ with the smearing function $W(t)$ (a boxcar) and the scattering function $G(t)$, resulting in the observed pulse:

$$U_{\rm obs}(t) = \int_{-\infty}^{\infty} \int_{-\infty}^{\infty} U(t') \, G(t - t'') \, W(t'' - t') \, dt' \, dt''. \tag{18}$$

The combined effect of dispersion and scattering reduces the sharpness of the pulse and the effective $S_{\max}$. The reduction factor η, which accounts for these effects, is:

$$\eta = \frac{W_{\rm int}}{\sqrt{W_{\rm int}^2 + \Delta t_{\rm DM}^2 + \tau_{\rm sc}^2}}, \tag{19}$$

where $W_{\rm int}$ is the intrinsic pulse width. The signal-to-noise ratio (SNR) (*S/N*) of the folded profile, accounting for this reduction, becomes:

$$S/N = \frac{\sum_{i=1}^{n} S_{\max,i} \cdot \eta}{\sqrt{\sum_{i=1}^{n} \sigma_i^2}}. \tag{20}$$

Pulse Jitter

Pulse jitter refers to the random phase variation of individual pulses relative to a mean phase aligned with the NS's rotation. Intrinsic pulse shape variations and the finite number of pulses received in an observation cause a TOA bias, known as jitter [317, 362]. It requires a dedicated noise model because its impact depends on pulsar brightness, which varies due to interstellar scintillation (see below), and because it is correlated over the observing bandwidth [104]. Pulse jitter affects the precision of TOA measurements by introducing variability in individual pulse shapes, despite the stability of the average pulse profile. This variation scales with the number of pulses observed and has a frequency-dependent impact due to varying pulse profiles across different radio frequencies [105, 182, 242, 243, 317].

Jitter-induced TOA uncertainty is given by:

$$\sigma_{\rm J} = \left[\frac{f_{\rm J}^2 \int U(t)\, t^2 dt}{n \int U(t)\, dt}\right]^{1/2}, \tag{21}$$

where $f_{\rm J}$ represents the width of the jitter phase PDF in units of the pulse width, n is the number of integrated pulses, and $U(t)$ is the normalized pulse waveform. Jitter effects scale as $1/\sqrt{n}$, meaning they become less significant with a large number of integrated pulses but are important for pulsars with high intrinsic phase instability.

The total timing uncertainty, incorporating noise, dispersion, scattering, and jitter, can be expressed as:

$$\sigma_{\rm total}^2 = \sigma_{t_{\rm a}}^2 + \sigma_{\rm J}^2. \tag{22}$$

Dispersion and scattering are frequency-dependent, with $\Delta t_{\rm DM} \propto f_{\rm c}^{-3}$ and $\tau_{\rm sc} \propto f_{\rm c}^{-4.4}$. Observing at higher frequencies mitigates their effects but reduces sensitivity. Jitter, on the other hand, is independent of frequency but depends on the intrinsic stability of the pulsar's emission. Mitigation strategies include coherent dedispersion, which removes dispersion smearing, and long integrations, which reduce the impact of jitter. Together, these effects influence the observed pulse shape, *S/N*, and timing precision, requiring careful modelling and correction for high-precision pulsar timing experiments.

The role of broad- and narrowband radio frequency interference

System noise fluctuations contribute an additional source of timing uncertainty, primarily arising from variations in the background noise level during observations. These fluctuations

scale inversely with the SNR (*S/N*), as higher *S/N* reduces the relative impact of noise on the observed pulse profile. The timing uncertainty due to system noise is expressed as:

$$\sigma_{\rm sys} = \frac{C_{\rm sys}}{S/N}, \tag{23}$$

where $C_{\rm sys}$ is a scaling factor representing the level of system noise. This uncertainty directly adds to the total TOA precision and becomes significant at lower *S/N*, where system noise dominates over other effects like jitter or scattering.

Random, narrow spikes within the pulse profile introduce irregularities that affect timing precision. These spikes, caused by external interference, add timing uncertainty proportional to the pulse width and inversely proportional to $\sqrt{S/N}$. The contribution of random spikes to the TOA uncertainty is modelled as:

$$\sigma_{\rm spikes} = \frac{C_{\rm spikes} W_{\rm int}}{\sqrt{S/N}}, \tag{24}$$

where $C_{\rm spikes}$ is a scaling factor representing the relative intensity and frequency of the spikes, and $W_{\rm int}$ is the intrinsic pulse width. This effect can significantly degrade timing precision, particularly in cases where random spikes are frequent or have high amplitude relative to the pulse profile. When combined with other broadening effects, such as dispersion or scattering, the presence of spikes further complicates the observed pulse shape. As a result a tremendous effort in pulsar timing goes into ensuring that the observed profiles are free from the effect of RFI, ranging from advanced time and frequency domain techniques [247, 301]. However, the complexity with which RFI appears in data implies particularly strongly affected observations require careful manual inspection and post-processing, or removal from pulsar timing datasets.

2.5. Polarization calibration errors

Incorrect polarization calibration is another potential source of error. Each observation involves correcting for differential gain and phase variations in polarization, as well as changing the parallactic angle. Miscalibration can introduce chromatic noise since polarization profiles depend on frequency [153, 377].

Each of these effects has a varying degree of impact on the achievable TOA precision, and naturally reflects a unique combination of the pulsar, the LOS to it, the instruments used to record the observations and their RFI environment. The commonly used strategy of observing pulsars for long durations and averaging their pulses has been remarkably successful, although with the latest generation of telescopes per pulsar optimised strategies must be used. Figure 5 demonstrates the effect each of the sources of error have on the overall timing precision achieved as a function of the number of individual pulses that have been 'integrated' into the observation. Clearly, pulse jitter, once we are sensitive to it becomes the most important, implying the need for deeper searches for more stable MSPs, along with the continued monitoring of currently observed pulsars.

3. Pulsar timing

In its essence, pulsar timing is the practice of associating a rotation count with every observation of a pulsar, relative to an arbitrary 'zeroth' pulse [263]. This is achieved by building interpolative models fitted against observations, such that the final solution is 'phase-connected'. In other words, pulse profiles at successive observations can be aligned to produce a continuous pulse-train.

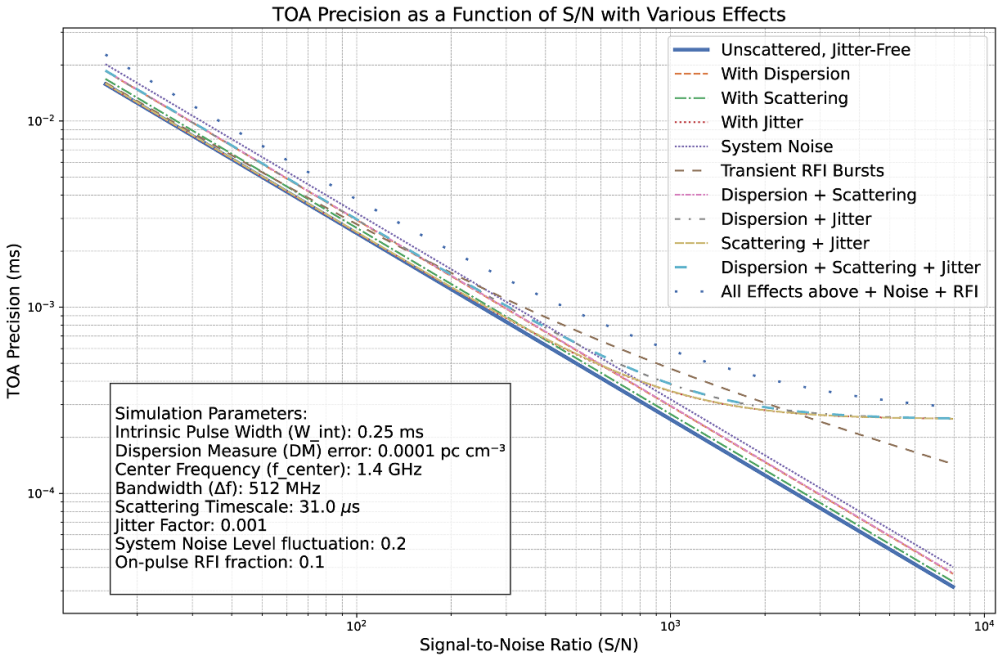

Figure 5. Plot showing the dependence of TOA precision on the S/N of the profile, and the degradation due to some known effects. The simulated pulse has a period of 1 ms and has a full-width half-minimum of .25 of the rotational phase.

This alignment can be achieved through the process of constructing a pulsar timing model, where a number of astrophysical and systematic effects can be accounted for, as sketched in figure 6. For an ideal, isolated pulsar the repetition of pulses is governed solely by the spin-period (F_0) and the rate at which angular momentum is lost as the dipolar magnetic field converts it into emission, typically only accounted for through the first derivative of the spin-period (F_1). Close to the pulsar's surface this would be sufficient to predict the *emitted* pulse-train. However, the *observed* pulse train at Earth bears the imprint of a number of possible sources of deviations from this simplistic behaviour.

Tracing back along the LOS from Earth, these effects include several deterministic effects. The first of these involves the translation of the pulse's site arrival time (SAT or T_{site}) measured at the observatory using precise clocks such as hydrogen masers (H-maser) to the Solar System Barycentre (SSB), which is the nearest and most precisely located inertial frame. This involves first translating the site arrival time (T_{site}) to the arrival time in UTC (T_{UT}) through any intermediate reference timing systems (clock_0, etc), before removing any propagation delays due to terrestrial atmosphere (Tropo).

As the emission propagates within the Solar System, the Shapiro delay ($\Delta_{S_\odot}$) induced by the gravitational potentials of the massive planets also contribute to the measured time of arrival, and the Einstein delay ($\Delta_{E_\odot}$) due to the relativistic frame transformations between the co-moving Earth and the SSB. These are calculated using SSEs such as those provided by the Jet Propulsion Laboratory (NASA-JPL) [316]. The most significant terms of this correction, indicated in the figure 6 include the Shapiro delays from the massive planets Venus, Jupiter, Saturn and Uranus (Ven_{shap}, etc), as well as Roemer and Einstein delays from the Solar

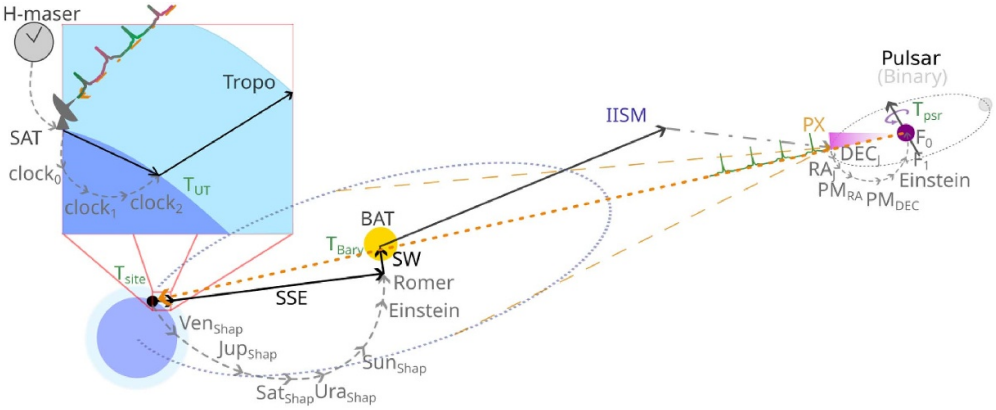

Figure 6. A schematic representation of the pulsar timing model of the MSP J1744−1134 pulsar. Since this is an isolated pulsar no binary terms need to be estimated. The contributions from each of the model terms are calculated relative to the SSB. Hence, the first step involves translating the pulse arrival time ($T_{\rm site}$) at Earth measured using high precision observatory clocks to the Barycentric arrival time ($T_{\rm Bary}$). Subsequently, delays between successive TOAs can be fitted to components from propagation in the turbulent IISM, a measure of the parallax as well as the properties of the pulsar itself such as its location and projected motion on the sky, and its rotational period and rate of angular momentum loss. Each of these delays are calculated through model fitting to 'align' the TOAs as explained in the text, such that the profiles linked to each TOA would appear in sequence, as they would have close to the pulsar. See section 3 for an explanation of the various terms and labels.

System and the retardation due to radio-wave propagation in the interplanetary medium (IPM) (or Solar Wind; SW).

Further corrections for the motion of the Earth ($\Delta_{\rm R_\odot}$), or those due to the mean electron content along the LOS with contributions from the terrestrial ionosphere (Δ_{iono}), the SW (Δ_{SW}) and the average electron column density encountered within the IISM (Δ_{iism}) can also be fitted for. The sum total of the delays due to ionised plasmas is then given by:

$$\Delta_{plasma} = \delta_{iono} + \delta_{SW} + \delta_{iism} \simeq \frac{e^2}{2\pi\, m_{\rm e} c^2}\left(\frac{1}{f^2{}_{low}} - \frac{1}{f^2{}_{high}}\right) DM \tag{25}$$

where DM represents the line integral of the average electronic content along the LOS per parsec cm^{-3};

$$DM \equiv \int_0^L n_{\rm e}{\rm d}l.$$

Although the observed DM includes the contribution of the SW and the ionosphere, since both the SW and ionosphere have independent measurements, *when considering their contributions as delays* these can be split out into the individual contributions [123, 205, 393]. For instance, most pulsar timing packages model the contribution from the SW using a spherical distribution centred on the Sun, with an inverse radius-squared density gradient.

Closer to the pulsar, once again a few relativistic effects become relevant—the Einstein delay due to the pulsar's own Gravitational potential—affects the pulse propagation. In the special case that the pulsar has a companion, additional delays such as the Shapiro delay from

the mass of the companion as well as any possible delays from excess electronic material of the companion, lying along the line of sight.

The delays due to bound companions in particular is easily factorised into the Keplerian parameters of the orbit, the orbital period P_b, the semi-major axis $a_1 \sin i$, the eccentricity e, the longitude of periastron ω, the time of periastron passage T_0. In case the timing precision is very high, the timing model can further include the derivatives of the terms above. For some of MSPs, especially those with massive companions, relativistic effects need to be included as well. The most commonly used models for pulsar timing assume GR [61, 112], and the timing of the double pulsar *J0737−3039* system, which sets the strongest limit on the validity of GR at low post Newtonian orders, suggests that this is a sufficient approximation.

Finally, pulsars are among some of the fastest moving astrophysical objects, and the motion of the pulsar itself can induce a delay in the pulse arrival time. Thus, corrections for the pulsar's proper motion ($\mathrm{PM_{RA,DEC}}$), the location of the pulsar, defining the orientation of the LOS and the parallax (PX), which is a proxy for the distance to the pulsar must all be factored into the total delay.

3.1. Pulsar timing models

Each of the delays listed above can be connected to a number of physical parameters, whose values for a given pulsar and the LoS to it can be determined using a *pulsar timing model*. The timing model is iteratively improved as more observations are made, and the best-fit values of the parameters are updated. For an isolated pulsar, the most important constraints include the spin period P, the period derivative $\dot{P}$, the position of the pulsar on the sky, the proper motion, and the parallax. For a pulsar in a binary system, the timing model includes the Keplerian parameters of the orbit, the mass function, and the Shapiro delay parameters. For all pulsars, the timing model includes the mean DM along the LOS to the pulsar. As more data is acquired, temporal variations in these parameters can be also modelled as derivatives.

Since the Earth is not an inertial frame, the timing model is referred to the nearest one, which is the SSB. This requires external knowledge of the masses of Solar System objects and their orbital parameters, which have been determined to fairly high precision for instance by the NASA Jet Propulsion Laboratory [316, and references therein] and the l'Institut de Mecanique Celeste [151, IMCCE]. Pulsar timing models thus include a reference SSE, often one of the longer term models of the JPL development ephemerides (DEs) (e.g. DE440 for the latest PTA results.)

The timing model must also include a chain of clock corrections to enable the transfer of the TOA from the local observatory to the SSB, through an intermediate frame, the geo-centre. The clock corrections include the observatory clock corrections, the Earth's rotation, and the Earth's orientation in space, usually provided by the international earth rotation and reference systems service (IERS). To account for the Earth's orientation, the timing model includes the earth orientation parameters (EOPs), which are updated regularly by the IERS.

Beyond the parameters connected to the pulsar, its environment and the LOS dependant features, a number of additional parameters are required to 'complete' the timing model. The first of this is the necessity to include an additional component for the propagation delay suffered by the pulses in the Solar Wind. This component is traditionally modelled as a spherically symmetric distribution, whose density decreases with the square of the inverse of the radial distance of the LOS, whose properties are controlled through a seed value of the SW density at 1 AU.

Figure 7 shows an example of applying a phase connected timing solution to a set of TOAs (in the top panel), leaving behind a set of timing 'residuals'. The timing residuals are the focus

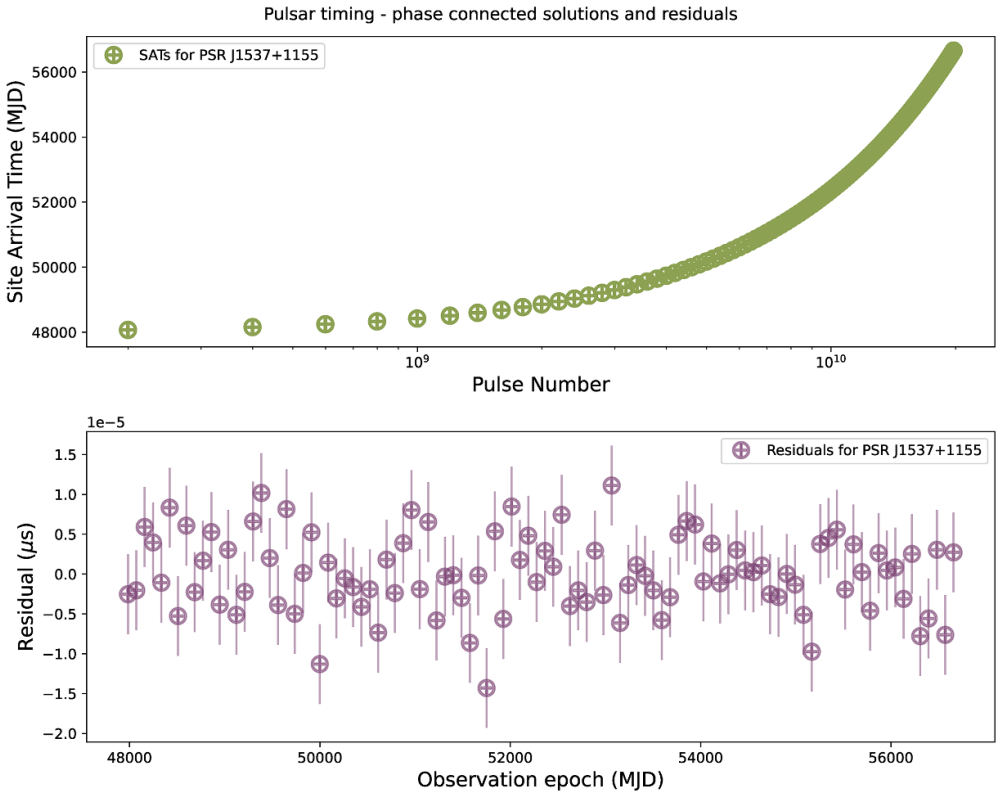

Figure 7. The top panel shows a sequence of synthetic TOAs generated using the PINT pulsar timing package, plotted against the rotation count associated with each TOA. The lower panel shows the timing residuals from the same set of TOAs after it has been fitted with the timing model.

of all downstream (after successful timing models have been obtained) analysis, since all of our signals of interest and the other nuisance terms must be modelled within them.

3.2. Extending the pulsar timing model to account for stochastic noise processes

PTAs extend pulsar timing to ensembles (arrays) of pulsars to search for correlated signals such as low-frequency GWs [184, 350]. The search for a stochastic GWB in pulsar timing data involves estimating a correlated signal common to the pulse TOAs recorded for different pulsars. Detecting this faint signal, which injects delays of a typical amplitude in the timing residuals of $\ll$100 ns, is made even more challenging due to a number of deterministic and stochastic effects that can mask it.

Following the previous sections, for each pulsar in a PTA, we can now create the timing model for the observed pulse TOAs (d) that accounts for multiple contributions:

$$d = \tau_{\rm TM} + \tau_{\rm WN} + \tau_{\rm SN} + \tau_{\rm DM} + \tau_{\rm CN} + \tau_{\rm GW}. \tag{26}$$

- $\tau_{\rm TM}$: The deterministic timing model characterizing the pulsar's properties as described in the previous section.
- $\tau_{\rm WN}$: Stochastic white noise induced by instrumental thermal noise and intrinsic pulsar noise.

- $\tau_{\rm SN}$: Stochastic red noise due to rotational irregularities or spin noise.
- $\tau_{\rm DM}$: Stochastic variations from changes in DM and other plasma along the LOS.
- $\tau_{\rm CN}$: Stochastic common noise, such as errors in the SSEs or time standard inaccuracies.
- $\tau_{\rm GW}$: The stochastic contribution from the GWB.

3.3. White noise

White noise (<1 day time scales) cannot produce GWB-like signals, but it must be modelled to estimate the precision of timing model parameters. Most analyses use the parameters EFAC and EQUAD [129, 251] both of which attempt to correct for underestimation of the TOA error-bars due to the effect of varying system noise in the observing system. These modify the measurement uncertainty σ_i of a TOA as:

$$\sigma_{t_{\rm a}}^2 \rightarrow {\rm EFAC}^2 \left(\sigma_i^2 + {\rm EQUAD}^2\right). \tag{27}$$

As described in section 2.4, correlated WN across epochs can introduce additional uncertainties in the TOA error-bars. These are often modelled using ECORR parameters. While the original motivations for the ECORR parameters were to model the effect of jitter on sets of narrowband TOAs, they can also model other short-timescale correlated processes, such as RFI or time variable scattering [243, 363]. From equations (22) and (27), the total TOA error now becomes:

$$\sigma_{t_{\rm a}}^2 \rightarrow {\rm EFAC}^2 \left(\sigma_i^2 + {\rm EQUAD}^2\right) + \sigma_{\rm J}^2. \tag{28}$$

As PTA datasets often rely on observations collected with a variety of observing systems at different telescopes, the white noise parameters can often number in the dozens, especially for some of the most well-timed pulsars. As a result, these parameters are typically only evaluated for each pulsar dataset, and then analytically marginalised over during the searches for common signals.

3.4. Rotational irregularities (spin noise)

Spin noise, also called timing noise or intrinsic noise, results from changes in the pulsar's rotational behaviour, possibly due to interactions between the NSs crust and superfluid core [215, 286]. It is well known in young, slowly spinning pulsars [191], but is also present in MSPs with an amplitude that is related to the pulsar spin-down rate [317]. This intrinsic noise is generally adequately modelled with a power-law spectrum, and represented in data either as long-term correlations between the TOAs, with a non-diagonal covariance matrix [100, 403], or using a Fourier expansion with the coefficients constrained to follow the assumed power spectrum [252].

The spin noise can be modelled using a Fourier basis and described by a two-parameter power-law model:

$$\phi_{\rm SN}\left(\nu, A_{\rm SN}, \gamma_{\rm SN}\right) = \frac{A_{\rm SN}^2}{12\pi^2}\left(\frac{1}{1\,{\rm yr}}\right)^{-3} \nu^{-\gamma_{\rm SN}}, \tag{29}$$

where $A_{\rm SN}$ and $\gamma_{\rm SN}$ are the amplitude and spectral index.

The prescriptions both assume that spin noise originates from a stationary process. This assumption may be appropriate if such spin noise originates from superfluid turbulence within the NS [286], or fluctuations within the pulsar magnetosphere, but it may be a poor approximation if such noise arises from, e.g. switches between metastable equilibria of the magnetosphere [234, 268, 395].

3.5. Effects of the ionised ISM

The ionised ISM is turbulent [26] and contains structures that act as lenses [106]. Radio waves from a pulsar encounter a continually changing electron density and bend proportionally to the inverse square of the observing radio frequency ν^{-2}. The wide range of observational consequences includes dispersive delays, strong intensity variations (scintillation), broadening of pulses due to multipath scattering, and higher-order effects, such as apparent position shifts [68, 103, 340].

DM variations. As introduced earlier, DM variations are a key frequency-dependent propagation effect in pulsar timing, occurring when radio pulses travel through the ionised ISM, IPM, and Earth's ionosphere. This results in a delay in pulse arrival times that varies with the frequency (ν) of the emission, proportional to the DM divided by ν^2. As the Earth, pulsar, and ISM move relative to one another, changes in the free electron content necessitate DM estimation for each observation. While dispersive delays are included in pulsar timing models, other time-dependent propagation effects are not.

DM variation contributes potentially hundreds of degrees of freedom to a pulsar timing model. One approach uses DMX parameters [118] to tabulate DM measurements from TOAs within discrete time segments. Another makes use of a constrained stochastic model for DM(t) (see spin noise above), which has fewer effective degrees of freedom but can only model stationary DM variations, which is generally insufficient to capture observed variations [100, 251, 426]. These different approaches to DM modelling can produce discrepant results: NANOGrav, using DMX [29], and the PPTA, using the stochastic model [337], find marginally different values for spin noise for pulsars common to the two PTAs (see below).

Currently, the most successful technique is the use of a constant mean DM term for each MSP, accompanied by (up to) two time derivatives followed by a Gaussian process model that absorbs the remaining DM-variations induced noise with an excellent degree of flexibility [244].

Scattering variations. Multipath propagation introduces additional delays that deviate from the ν^{-2} dispersive delay, causing pulse shape distortions. This effect, known as scattering, broadens the pulse shape with an exponential tail described by the pulse broadening function (PBF). The broadening generally follows a $\nu^{-4.4}$ scaling, though the exact index depends on the medium's properties. Scattering primarily delays the pulse in low-scattering regimes, and some pulsars exhibit prominent scattering, especially those with high DM or those observed at lower radio frequencies [185].

Ray path differences at different radio frequencies can cause the signal to traverse different sets of electrons, leading to slightly different DMs at each frequency. Precise characterization of this frequency-dependent DM at each epoch requires more precision than current analyses allow [104].

Refraction from multipath propagation causes the pulsar's observed sky position to vary, adding a geometric delay proportional to ν^{-4}. Additionally, variations in the angle of arrival create delays scaling as ν^{-2} and are covariant with dispersive delays [154].

Pulsar scintillation. Scintillation results from the interference of multiple ray paths in the extremely compact pulsar images. It is observed as modulation of the dynamic spectrum, called diffractive interstellar scintillation (DISS). The effect is characterised by coherence bandwidth ($\Delta\nu_d$) and coherence timescale (Δt_d), both inversely proportional to the pulsar's distance.

While DISS stochastically changes the PBF, it limits TOA precision, particularly at lower frequencies [241]. For nearby MSPs, coherence timescales and bandwidths are often similar to the total observation time (around 30 min) and observing bandwidths, leading to a 'finite scintle' effect. This phenomenon is covariant with pulse jitter but can be disentangled due to its strong frequency dependence [107, 242]. Although scintillation parameter measurements could inform the analysis, they are not currently applied.

In summary, the monitoring, measurement, and interpolation of IISM-induced residuals is an observationally and computationally expensive endeavour and a source of unmodelled error. Although PTAs have managed to reduce these effects to the $\lesssim 1\,\mu$s level, significant improvements can be achieved by adding sensitive low frequency data [123, 205].

3.6. Solar wind effects

The solar wind, a stream of charged particles from the Sun's corona, creates an ionised IPM with an electron density that decreases with distance from the Sun [278]. As Earth orbits the Sun, the LOS to a pulsar passes through different parts of the IPM, resulting in annual DM variations. Traditional solar wind modelling involves assuming a spherically symmetric electron density as a function of the Sun-pulsar separation angle [129].

The solar wind's impact on DM depends on the pulsar's proximity to the ecliptic plane, with those close to the ecliptic showing sharp DM peaks at minimum solar separation [123, 393]. This results in a chromatic and spatially correlated signal among pulsars [392]. However, the solar wind is not perfectly spherical or static, varying over the 11 year solar cycle [207]. These variations, along with differences between 'fast' and 'slow' solar wind densities, render simple spherical models inadequate at PTA precision levels [180, 270, 378, 393, 394]. Uncorrected solar wind variations can contribute correlated noise to pulsars [392].

3.7. Pulse profile variations

Pulse profile variations induce apparent variations in TOAs and cannot be easily mitigated. Observed variations in PSR J1643−1224 [361] and PSR J0437−4715 [311] have been attributed to a transient magnetospheric reconfiguration, while alterations in the pulse profile of PSR J1713+0747 may be associated with rapid apparent DM variations and recovery [258]. Mode changing involves shifts in the average pulse profile between discrete states over varying timescales. A dramatic form is 'nulling', where a pulsar temporarily ceases emission. Nulling is mostly observed in slow-period pulsars but not yet in MSPs, likely due to detection challenges [35, 202]. However, mode changing has been detected in a few MSPs [271, 292, 414]. These variations contribute noise similar to pulse jitter in timing measurements, and further research is ongoing to assess their impact on pulsar timing.

3.8. Orbital period variations

Many pulsars observed by PTAs are in binary systems, usually with white dwarf companions [23, 152]. While these systems generally conform to Keplerian models, some display post-Keplerian parameters and require more complex modelling due to orbital irregularities.

MSPS in low-eccentricity 'black widow' systems [359] experience tidal and wind effects cause measurable orbital variations. For these, higher-order orbital frequency derivatives can be detected. Some pulsars also show significant red noise with a shallow spectral index, suggesting minimal mismodelling impact on GW analyses. While many black widow systems exhibit stable orbits, others show more noise due to irregular angular momentum transfer [38,

60]. However, the noise has little effect on GW sensitivity since the orbital periods are much shorter than the GW signal's timescales [62].

PSR J1024−0719 is in a wide-binary system where a complete orbit cannot be measured. Its orbital motion is modelled as a second derivative in the pulsar's spin frequency, but the presence of red noise implies that unmodelled orbital variations could contribute to the total noise budget [44, 220].

Lastly, there are two known pulsars in triple systems. One, PSR J0337+1715, is being timed by NANOGrav and requires higher-order general relativistic effects in its timing model. Despite its complexity, PSR J0337+1715 shows minimal excess noise beyond template-fitting uncertainties, indicating the potential significance of triple systems in future PTA studies [25, 332, 391].

3.9. SSEs

TOAs measured at an observatory must be transformed to the quasi-inertial reference frame of the SSB using a planetary ephemeris. Notable ephemerides include NASA's DE, most recently DE441 [316], and the Observatoire de Paris's INPOP series, most recently INPOP19a [151]. The primary source of uncertainty in these ephemerides arises from inaccuracies in planetary mass measurements, particularly those of the outer planets, which introduce a sinusoidal signature in the timing residuals of pulsars. This signature appears as a dipolar signal in PTAs [392].

The orbital periods of the giant planets range from 11.9 to 164.8 years, corresponding to frequencies of about 0.4–2.7 nHz. This range overlaps with the frequencies probed by PTAs for the GWB. To mitigate the impact of these uncertainties on PTA analyses, the orbital parameters in the ephemeris are perturbed, and results are compared across different ephemeris models [93, 402]. These adjustments enable the PTA analyses to produce consistent results, regardless of the ephemeris version used.

Additionally, PTA data sets have been used to search for non-GW common noise signals and place limits on the masses of outer planets, large asteroids, and even undiscovered planets in the outer Solar System [77, 90, 174].

3.10. Full design-matrix construction

Having discussed dominant stochastic processes in PTA datasets, we now build a single 'design' matrix per pulsar that spans all *deterministic* and *stochastic* basis functions except white noise, which remains in the covariance. For brevity, the discussion here is very simplified and readers are encouraged to explore the detailed analyses of van Haasteren [175, 403, etc], Lentati [254] and Taylor [388]. For pulsar I, we define

$$T_I \equiv \left[G_I^C \quad F_I^{\mathrm{SN}} \quad F_I^{\mathrm{DM}} \quad F_I^{\mathrm{CN}} \quad F_I^{\mathrm{GW}} \right], \tag{30}$$

with matching parameter vector

$$b_I = \begin{pmatrix} a_I \\ \epsilon_I \\ \delta_I \\ \gamma_I \\ \zeta_I \end{pmatrix}, \tag{31}$$

where

$$\begin{aligned} a_I &: \text{ coefficients for the timing-model basis } G_I^C\ (\tau_{\rm TM}), \\ \epsilon_I &: \text{ amplitudes for the spin-noise basis } F_I^{\rm SN}\ (\tau_{\rm SN}), \\ \delta_I &: \text{ amplitudes for the DM-variation basis } F_I^{\rm DM}\ (\tau_{\rm DM}), \\ \gamma_I &: \text{ coefficients for the common-noise basis } F_I^{\rm CN}\ (\tau_{\rm CN}), \\ \zeta_I &: \text{ amplitudes for the GWB basis } F_I^{\rm GW}\ (\tau_{\rm GW}). \end{aligned} \tag{32}$$

The global parameter vector stacks all pulsars:

$$b = \begin{pmatrix} b_1 \\ \vdots \\ b_N \end{pmatrix}. \tag{33}$$

Each block produces one of the six τ-terms:

$$\begin{aligned} \tau_{\rm TM}^{(I)} &= G_I^C\, a_I, & \tau_{\rm SN}^{(I)} &= F_I^{\rm SN}\, \epsilon_I, \\ \tau_{\rm DM}^{(I)} &= F_I^{\rm DM}\, \delta_I, & \tau_{\rm CN}^{(I)} &= F_I^{\rm CN}\, \gamma_I, \\ \tau_{\rm GW}^{(I)} &= F_I^{\rm GW}\, \zeta_I, \end{aligned} \tag{34}$$

hence

$$\tau_I \;=\; T_I b_I \;=\; \sum_{X\in\{\rm TM,\,SN,\,DM,\,CN,\,GW\}} F_I^X\, b_I^X \quad \left(\text{with } F_I^{\rm TM} \equiv G_I^C\right). \tag{35}$$

Stacking all N pulsars,

$$T = \text{blockdiag}\,(T_1, \ldots, T_N), \qquad b = \begin{pmatrix} b_1 \\ \vdots \\ b_N \end{pmatrix}, \tag{36}$$

so that

$$\tau \;=\; T b. \tag{37}$$

The white-noise term $\tau_{\rm WN}$ is not in T but enters through the covariance

$$N = \text{blockdiag}\,(N_1, \ldots, N_N), \qquad N_I = E_I^2 W_I + Q_I^2 I + J_I, \tag{38}$$

where E_I (EFAC) rescales formal TOA uncertainties W_I, Q_I (EQUAD) adds quadrature white noise, and J_I (ECORR/jitter) contributes an epoch-correlated white-noise term (block-diagonal across observing epochs/backends).

3.10.1. Gaussian-process likelihood. We place zero-mean Gaussian priors on the linear coefficients b:

$$p\,(b \mid \theta) = \mathcal{N}\,(0, B\,(\theta)), \tag{39}$$

where B is block-diagonal across processes. For Fourier-sum bases, each block is diagonal with entries set by the one-sided residual power spectral density (PSD) evaluated at $f_k = k/T_{\rm span}$:

$$B\,(\theta) = \text{blockdiag}\big(\Phi^{\rm TM}, \Phi^{\rm SN}\,(\theta_{\rm SN}), \Phi^{\rm DM}\,(\theta_{\rm DM}), \Phi^{\rm CN}\,(\theta_{\rm CN}), \Phi^{\rm GW}\,(\theta_{\rm GW})\big). \tag{40}$$

For a stationary power law, the residual PSD is

$$P_X(f;A_X,\gamma_X) = \frac{A_X^2}{12\pi^2}\left(\frac{f}{f_{\rm yr}}\right)^{-\gamma_X} f^{-3}, \qquad f_{\rm yr} \equiv 1\,{\rm yr}^{-1}, \tag{41}$$

and Φ^X is diagonal with elements $P_X(f_k)$ (up to a known normalization that depends on the chosen Fourier convention). For the GWB, spatial correlations enter via the HD overlap-reduction matrix Γ, so that

$$\Phi^{\rm GW}(\theta_{\rm GW}) \;\to\; \Phi^{\rm GW}(\theta_{\rm GW}) \otimes \Gamma, \qquad \Gamma_{ab} = \Gamma(\zeta_{ab}). \tag{42}$$

The conditional likelihood of the residuals d given b is

$$p(d \mid b, M) = \frac{1}{\sqrt{|2\pi N|}} \exp\left[-\tfrac{1}{2}(d-Tb)^\top N^{-1}(d-Tb)\right]. \tag{43}$$

Analytically marginalizing over b yields the Gaussian *marginal* likelihood

$$p(d \mid \theta, M) = \frac{1}{\sqrt{|2\pi C(\theta)|}} \exp\left[-\tfrac{1}{2} d^\top C(\theta)^{-1} d\right], \quad C(\theta) = N + TB(\theta)\,T^\top. \tag{44}$$

3.10.2. Prior choices and typical PTA ranges. We adopt weakly informative priors on the hyperparameters θ that follow standard PTA practice. Representative choices are:

- **White noise** (per backend/receiver): $E_I \sim \mathcal{U}(0.1,5)$; $\log_{10} Q_I/{\rm s} \sim \mathcal{U}(-9,-5)$; $\log_{10}{\rm ECORR}_I/{\rm s} \sim \mathcal{U}(-9,-5)$.
- **Spin noise** (per pulsar): $\log_{10} A_{\rm SN,I} \sim \mathcal{U}(-20,-10)$; $\gamma_{\rm SN,I} \sim \mathcal{U}(0,7)$; number of Fourier modes $K_{\rm SN} \in [30,50]$ with $f_k = k/T_{\rm span}$.
- **DM variations** (per pulsar): $\log_{10} A_{\rm DM,I} \sim \mathcal{U}(-20,-8)$; $\gamma_{\rm DM,I} \sim \mathcal{U}(0,7)$; chromatic index fixed to ν^{-2} in the basis (and optionally a separate ν^{-4} 'scattering' term with an analogous prior).
- **Common processes (clock/ephemeris)**: common-spectrum red noise (monopole) and/or BAYESEPHEM-like terms with zero-mean Gaussian priors centered at the reference ephemeris and widths set by published uncertainties; for a phenomenological monopole process, $\log_{10} A_{\rm CN} \sim \mathcal{U}(-20,-11)$, $\gamma_{\rm CN} \sim \mathcal{U}(0,7)$.
- **Stochastic GWB**: $\log_{10} A_{\rm GWB} \sim \mathcal{U}(-20,-11)$ (typical narrower choices: $[-18,-12]$); either fix $\gamma_{\rm GWB} = 13/3$ (SMBHB prior) or set $\gamma_{\rm GWB} \sim \mathcal{U}(0,7)$. The corresponding residual PSD uses equation (41), and spatial correlations follow Γ (HD).

Priors on linear timing-model parameters a_I are taken to be broad Gaussians (or implicit via generalized least squares), ensuring that deterministic timing fits are absorbed into $G_I^C a_I$ before stochastic inference.

3.10.3. Posterior inference and model comparison. Bayes' theorem gives the joint posterior over hyperparameters:

$$p(\theta \mid d, M) \;=\; \frac{p(\theta \mid M)\, p(d \mid \theta, M)}{p(d \mid M)}. \tag{45}$$

We explore $p(\theta \mid d, M)$ using Monte Carlo samplers (e.g. parallel-tempered Markov-chain-Monte-Carlo (MCMC) or nested sampling) and report posteriors for amplitudes and spectral indices of each process. Model evidences $p(d \mid M)$ enable Bayes-factor comparisons between,

for example, (i) a common-spectrum, spatially *uncorrelated* red-noise model and (ii) a HD *correlated* GWB model, or between fixed-$\gamma_{\rm GWB} = 13/3$ and free-$\gamma_{\rm GWB}$ hypotheses.
Notes on implementation. Fourier bases use $f_k = k/T_{\rm span}$ with $k = 1, \ldots, K$, low-frequency cutoff $1/T_{\rm span}$, and K chosen so that $f_{\rm K}$ spans the band where red power is informative; results are robust to reasonable choices of K provided convergence diagnostics are satisfied. The mapping between PSD normalizations and Φ^X depends on the precise basis normalization; our implementation follows the convention that the diagonal entries of Φ^X equal the one-sided residual PSD $P_X(f_k)$ (up to a known factor that is absorbed consistently into F_I^X).

This formalism is readily leveraged to search for signals of interest: the linear coefficients b are analytically marginalized, leaving an exact Gaussian likelihood in θ; posterior sampling over θ yields credible intervals for process amplitudes/spectra and Bayes factors for spatial correlations characteristic of a GWB.

3.11. Pulsar timing packages

Pulsar timing has been greatly simplified as a technique through the development of timing packages. Typically, these make use of the linearised least squares based fitting to perform frequentist parameter estimation of the different pulsar timing model terms. Typically linked with pulsar data processing at individual telescopes, the earliest tools include packages such as PSRTime[6] (used at Jodrell Bank) and Tempo [305]. While Tempo continues to be used by some timers even today, the most commonly used high-precision timing packages capable of handling timing residuals of the order of a few tens of nanoseconds at present are Tempo2 [129] and PINT [266].

TEMPO2 [129, 194] is a widely used software package for high-precision pulsar timing. It was developed as an evolution of the older TEMPO package, with the goal of improving accuracy, flexibility, and performance in pulsar timing data analysis. TEMPO2 is primarily written in C/C++, although some Python interfaces are available to facilitate scripting and integration with other tools. It implements advanced clock corrections, ephemerides, and timing models, and it also provides a range of plugins for visualization and extended data analysis. The software is highly extensible, allowing for incorporation of new timing models and reference frames as scientific needs evolve. Supported by an international community of pulsar astronomers, TEMPO2 is widely adopted and maintained[7], making it a long-standing and trusted solution. Users have access to public documentation, and the large existing user base provides additional resources and references for learning and troubleshooting.

PINT is a Python-based pulsar timing package designed to offer a modern, open-source, and user-friendly framework for analysing pulsar timing data. It integrates seamlessly with popular Python data-science libraries, such as NumPy, SciPy, and Astropy, and is straightforward to install (e.g. via `pip`). PINT is actively developed and tested by collaborations including the North American nHz Observatory for GWs (NANOGrav). The code features robust unit tests, continuous integration, and a modular structure that accommodates clock corrections, parameter modelling, and error propagation. This architecture also facilitates quick adaptation of new timing models and methods for ongoing research. Maintained on GitHub with frequent updates, PINT benefits from detailed tutorials and thorough documentation, making it accessible to users seeking a Python-centric scientific workflow.

[6] www.jb.man.ac.uk/∼pulsar/observing/progs/psrtime.html.
[7] https://bitbucket.org/psrsoft/tempo2/.

While Tempo2 and PINT are excellent tools for frequentist analysis, and both even offer additional methods for fitting for stochastic signals, Bayesian analysis to search for the noise models in each pulsar are often carried out using stochastic sampling (MCMC or Nested Sampling) based Bayesian analysis. These tools are indispensable and form the core of every PTA analysis.

TempoNest [253][8] is an extension of the TEMPO2 pulsar timing software package that incorporates Bayesian inference techniques for parameter estimation. Specifically, it utilises the `MultiNest` [149] and `PolyChord` [176] nested-sampling algorithms to explore high-dimensional parameter spaces in a more robust and statistically principled manner than standard least-squares or grid-based approaches. TempoNest aids in deriving posterior distributions for pulsar and timing model parameters, thereby accounting for uncertainties and model degeneracies. It is written in a mix of C/C++, Python, and Fortran, integrating closely with the underlying TEMPO2 libraries.

Enterprise (short for 'Enhanced Numerical Toolbox Enabling a Robust Pulsar Inference Suite') [136] is a Python-based software toolkit designed for advanced data analysis and Bayesian inference. Enterprise is particularly geared toward searching for the stochastic signals in the timing residuals of MSPs. Enterprise combines high-level Python functionality with sophisticated Bayesian sampling methods to enable flexible modelling of pulsar timing data.

It implements a parallel-tempered MCMC (PTMCMC) sampler by default, with optional interfaces to nested-samplers (e.g. dynesty) for evidence estimation. Crucially, Enterprise exploits the block-structured covariance of a PTA: each pulsar's noise contributions form a diagonal-plus-low-rank matrix while the common-process terms introduce off-diagonal blocks. By applying the Sherman–Morrison–Woodbury identity and sparse-Cholesky routines, Enterprise reduces the computational cost of inverting an $N_{\rm tot} \times N_{\rm tot}$ residual covariance from $\mathcal{O}(N_{\rm tot}^3)$ to near $\mathcal{O}(N_{\rm max}^3 + N_{\rm tot}^2)$, where $N_{\rm max}$ is the largest single-pulsar TOA count. This sparse-matrix inverter, coupled with batched likelihood evaluations across tempering chains, makes joint inference over dozens of MSPs—and their spatially correlated GWB or clock errors—tractable in high performance computing cluster environments. Unlike TempoNest's focus on per-pulsar noise characterization, Enterprise is engineered for PTA-wide model selection and signal recovery, offering a library of noise and GW strain models that plug seamlessly into its sampling workflows.

4. The pulsar timing residual from GWs

Once phase-connected timing solutions and a satisfactory stochastic–noise model are established, the inference of a stochastic GWB proceeds from the post-fit residuals. The working null hypothesis is an astrophysical background from a cosmological population of SMBHBs, which predicts a power-law characteristic strain ($h_{\rm c}(f)! \propto! f^{-2/3}$) together with the quadrupolar HD spatial correlation. The inference framework is, however, source-agnostic: the same linear response and cross-correlation formalism applies to backgrounds of cosmological origin (inflationary tensors, scalar-induced GWs, first-order phase transitions, cosmic strings, domain walls). In the subsections below, we set out the strain field and its mapping to timing redshifts and residuals, the associated angular correlation kernel, and the relation between strain spectra and the energy-density parameter ($\Omega_{\rm gw}(f)$); we then specialise to the SMBHB case and briefly comment on cosmological alternatives.

[8] https://github.com/LindleyLentati/TempoNest.

4.1. GW strain

The GW strain tensor $h_{ij}(t,\vec{x})$ can be expressed as a superposition of plane waves with different frequencies f and propagation directions $\hat{k}$:

$$h_{ij}(t,\vec{x}) = \sum_{A=+,\times} \int_{-\infty}^{\infty} \mathrm{d}f \int_{S^2} \mathrm{d}\hat{k}\, h_A\left(f,\hat{k}\right) \epsilon_{ij}^{A}\left(\hat{k}\right) \mathrm{e}^{-2\pi i f\left(t-\frac{\hat{k}\cdot\vec{x}}{c}\right)}. \tag{46}$$

For a GW propagating in the $\hat{z}$-direction, the polarization tensors are:

$$\epsilon^{+} = \begin{pmatrix} 1 & 0 & 0 \\ 0 & -1 & 0 \\ 0 & 0 & 0 \end{pmatrix}, \quad \epsilon^{\times} = \begin{pmatrix} 0 & 1 & 0 \\ 1 & 0 & 0 \\ 0 & 0 & 0 \end{pmatrix}. \tag{47}$$

In general, for a GW propagating in direction $\hat{\Omega}$, the polarization tensors are:

$$\epsilon_{ij}^{+} = \hat{m}_i \hat{m}_j - \hat{n}_i \hat{n}_j, \quad \epsilon_{ij}^{\times} = \hat{m}_i \hat{n}_j + \hat{n}_i \hat{m}_j, \tag{48}$$

where $\hat{m}$ and $\hat{n}$ are unit vectors orthogonal to $\hat{\Omega}$, forming an orthonormal basis.

4.2. Pulsar timing residuals

The effect of a GW on the pulsar timing residual $r(t,\hat{e})$ is calculated by integrating the redshift fluctuations $z(t,\hat{e})$:

$$r(t,\hat{e}) = \int_0^t \mathrm{d}t'\, z(t',\hat{e}), \tag{49}$$

where t is the observation time and $\hat{e}$ is the unit vector pointing from Earth to the pulsar.

The redshift fluctuation $z(t,\hat{e})$ is given by:

$$z(t,\hat{e}) = \frac{1}{2} \frac{\hat{e}^i \hat{e}^j}{1+\hat{k}\cdot\hat{e}} \left[h_{ij}\left(t,\vec{0}\right) - h_{ij}\left(t - \tfrac{L}{c}\left(1+\hat{k}\cdot\hat{e}\right), L\hat{e}\right)\right], \tag{50}$$

where L is the distance to the pulsar and $h_{ij}(t,\vec{x})$ is evaluated at Earth ($\vec{x}=\vec{0}$) and at the pulsar ($\vec{x}=L\hat{e}$).

Substituting the expression for h_{ij} and integrating over frequencies and directions, the timing residual becomes:

$$r(t,\hat{e}) = \sum_{A=+,\times} \int_{-\infty}^{\infty} \mathrm{d}f \int_{S^2} \mathrm{d}\hat{k}\, h_A\left(f,\hat{k}\right) \frac{1-\mathrm{e}^{-2\pi i f \frac{L}{c}\left(1+\hat{k}\cdot\hat{e}\right)}}{2\pi i f\left(1+\hat{k}\cdot\hat{e}\right)} F^A\left(\hat{e},\hat{k}\right) \mathrm{e}^{-2\pi i f t}, \tag{51}$$

where $F^A(\hat{e},\hat{k})$ is the antenna pattern function:

$$F^A\left(\hat{e},\hat{k}\right) = \frac{1}{2}\hat{e}^i \hat{e}^j \epsilon_{ij}^{A}\left(\hat{k}\right). \tag{52}$$

4.3. The Hellings and Downs correlation

For a stochastic GWB, the GW amplitudes satisfy:

$$\left\langle h_A\left(f,\hat{k}\right) h_{A'}^{*}\left(f',\hat{k}'\right)\right\rangle = \delta_{AA'}\delta\left(f-f'\right)\delta^2\left(\hat{k}-\hat{k}'\right)\frac{1}{2}S_h(f), \tag{53}$$

where $S_h(f)$ is the one-sided PSD and $\langle\cdots\rangle$ denotes an ensemble average.

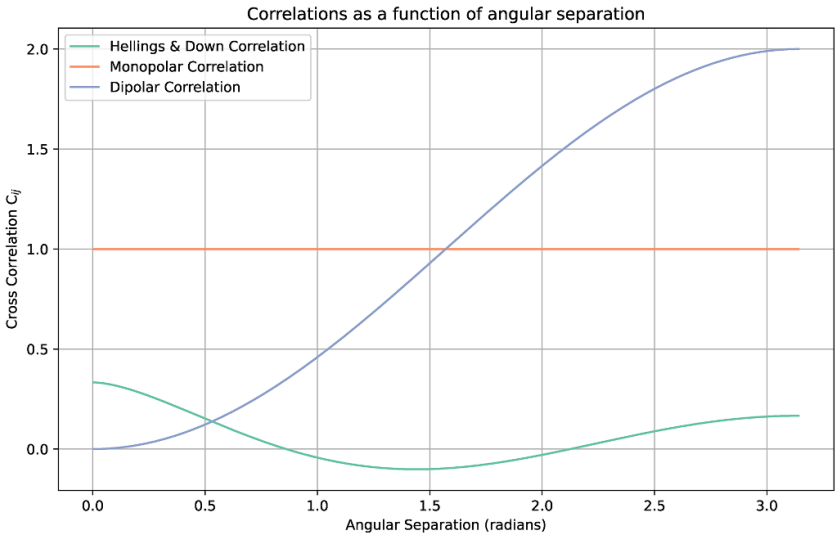

Figure 8. The ideal correlation response of a uniformly distributed pulsar timing array to monopolar, dipolar and quadrupolar (GW) signals.

The cross-correlation between timing residuals from two pulsars a and b is:

$$\langle r_{\rm a}(t)\, r_b(t)\rangle = \int_0^\infty {\rm d}f\, S_h(f)\, \Gamma(\zeta_{ab})\, \frac{\sin^2(\pi f T)}{(\pi f)^2}, \tag{54}$$

where T is the observation time, ζ_{ab} is the angular separation between pulsars a and b, and $\Gamma(\zeta_{ab})$ is the Hellings and Downs correlation function:

$$\Gamma(\zeta) = \frac{3}{2}\left[\frac{1-\cos\zeta}{2}\ln\left(\frac{1-\cos\zeta}{2}\right) - \frac{1-\cos\zeta}{6} + \frac{1}{3}\right]. \tag{55}$$

This function encapsulates the expected quadrupolar correlation between pulsars due to GWs and is pivotal in detecting the SGWB using PTAs. Figure 8 shows plots of an HD-correlated process, along with correlations arising from monopolar or dipolar processes, which often indicate systematics and other, possible non-GWB sources (see e.g. [392]).

4.4. Phinney's theorem and GW energy density

Phinney's theorem [323] relates the GW energy density to the observable background. The total energy density in GWs is:

$$\mathcal{E}_{\rm gw} = \rho_{\rm c} c^2 \int {\rm d}(\ln f)\, \Omega_{\rm gw}(f), \tag{56}$$

where $\rho_{\rm c} = \frac{3H_0^2}{8\pi G}$ is the critical mass density of the universe and $\Omega_{\rm gw}(f)$ is the GW energy density fraction per logarithmic frequency interval.

Considering a population of sources emitting GWs with energy ${\rm d}E/{\rm d}(\ln f_r)$ at source-frame frequency f_r, the observed energy density is:

$$\mathcal{E}_{\rm gw} = \int {\rm d}z N(z) \int {\rm d}(\ln f_r)\, \frac{{\rm d}E}{{\rm d}(\ln f_r)}\, \frac{1}{1+z}, \tag{57}$$

where $N(z)$ is the comoving number density of sources at redshift z, $f_r = f(1+z)$ relates observed frequency f to source-frame frequency f_r, and the factor $1/(1+z)$ accounts for redshifted energy.

By equating the two expressions for $\mathcal{E}_{\rm gw}$, we derive:

$$\Omega_{\rm gw}(f) = \frac{1}{\rho_{\rm c} c^2} \int {\rm d}z N(z) \frac{{\rm d}E}{{\rm d}(\ln f_r)} \frac{1}{1+z}. \tag{58}$$

4.4.1. Application to SMBHBs. For circular SMBHBs, the energy emitted per logarithmic frequency interval is:

$$\frac{{\rm d}E}{{\rm d}(\ln f_r)} = \frac{(\pi G)^{2/3}}{3} \mathcal{M}^{5/3} f_r^{2/3}, \tag{59}$$

where $\mathcal{M}$ is the chirp mass of the binary. Substituting this into $\Omega_{\rm gw}(f)$, we obtain:

$$\Omega_{\rm gw}(f) = \frac{(\pi G)^{2/3}}{3\rho_{\rm c} c^2} \mathcal{M}^{5/3} f^{2/3} \int {\rm d}z N(z) (1+z)^{-4/3}. \tag{60}$$

This shows that $\Omega_{\rm gw}(f) \propto f^{2/3}$ for a population of inspiraling SMBHBs.

4.5. Stochastic GWB from SMBHBs

The most anticipated source of GWs at nHz frequencies is the cosmic population of SMBHBs. As galaxies merge, the SMBHs at their centres form binary systems (i.e. SMBHBs) that eventually coalesce, emitting gravitational radiation. The overall GW signal from these binaries can be approximated as a stochastic background, dominated by the few nearby, massive sources [354].

The GW energy density parameter, $\Omega_{\rm gw}(f)$, is related to the characteristic strain spectrum, $h_{\rm c}(f)$, by:

$$\Omega_{\rm gw}(f) = \frac{2\pi^2}{3H_0^2} f^2 h_{\rm c}^2(f), \tag{61}$$

where H_0 is the Hubble constant (in units of $\rm s^{-1}$). The characteristic strain $h_{\rm c}(f)$ is often modelled as a power law:

$$h_{\rm c}(f) = A \left(\frac{f}{f_{\rm ref}}\right)^{\alpha}, \tag{62}$$

where A is the amplitude at a reference frequency $f_{\rm ref}$, and α is the spectral index. For a population of inspiraling SMBHBs, $\alpha = -2/3$, leading to $h_{\rm c}(f) \propto f^{-2/3}$ and, consequently, $\Omega_{\rm gw}(f) \propto f^{2/3}$. The amplitude and shape of this background depend on the SMBHB population, the Galaxy merger rate, and the dynamics of binary evolution.

The amplitude of the GWB provides valuable information about the merger history of galaxies and the post-merger dynamics of SMBHBs [138, 229, 353]. It can be expressed as:

$$h_{\rm c}(f) = A_{\rm GWB} \left(\frac{f}{f_{\rm yr}}\right)^{-2/3}, \tag{63}$$

where $A_{\rm GWB}$ is the amplitude of the GWB at the reference frequency $f_{\rm yr} = 1\,{\rm yr}^{-1}$. The 'final parsec problem' [297] concerns how these binaries lose sufficient energy to eventually merge. A confirmed detection of a GWB from SMBHBs would directly indicate that these binaries do merge, offering insights into their evolution and resolving this problem.

4.5.1. GWs from the early universe. While SMBHBs are the primary candidate for the observed signal, several processes occurring in the early universe could also generate a stochastic GWB at nHz frequencies. One of the most important sources is primordial GWs from inflation, where quantum fluctuations of the gravitational field were stretched to macroscopic scales during the rapid expansion of the universe [170, 344, 374]. The power spectrum of these GWs depends on the inflationary model and can be written as:

$$P_h(k) = A_{\rm s}\left(\frac{k}{k_{\rm ref}}\right)^{n_{\rm t}} \tag{64}$$

where $P_h(k)$ is the tensor power spectrum, $A_{\rm s}$ is the amplitude, k is the wave number, $k_{\rm ref}$ is the reference wave number, and $n_{\rm t}$ is the tensor spectral index. These primordial GWs would provide direct evidence of the physics of inflation, a period of rapid expansion in the early universe.

Other early universe processes, such as phase transitions, cosmic strings, and magnetohydrodynamic turbulence, can also generate GWs. For example, cosmic strings, predicted by many grand unified theories (GUTs), would produce a characteristic GW spectrum due to the formation and decay of string loops [113, 410]. The characteristic strain from cosmic strings follows a power-law spectrum:

$$h_{\rm c}(f) \propto f^{-7/6} \tag{65}$$

The detection of GWs from these early universe sources would offer a unique window into the conditions and physics at the earliest moments of the universe, potentially probing energy scales far beyond those accessible by particle accelerators.

4.5.2. Ultracompact Dark Matter and other non-GW contributions. In addition to GWs, other processes can produce correlated timing residuals in pulsar timing data. For example, imperfections in the SSEs can introduce dipolar correlated noise, while errors in the terrestrial time standard can result in monopolar noise [392]. These effects need to be carefully accounted for in PTA analyses.

Another potential source of correlated delays in pulsar timing data is ultralight $\mathcal{DM}$ (UL$\mathcal{DM}$), also known as fuzzy $\mathcal{DM}$. UL$\mathcal{DM}$ could form coherent scalar fields that oscillate at frequencies proportional to the $\mathcal{DM}$ particle mass, leading to harmonic modulations in pulsar arrival times [227]. The modulation frequency would be related to the mass of the ultralight boson m_ϕ as:

$$f_{\rm mod} \sim \frac{m_\phi c^2}{h} \tag{66}$$

where h is Planck's constant, and c is the speed of light. The detection of such modulations could provide direct evidence of the nature of $\mathcal{DM}$ and its interaction with baryonic matter.

5. PTAs—the detector

The main objective of PTA experiments so far has been to identify a stochastic GWB using the spatial correlations between MSPs' pulse TOAs [184]. As discussed earlier, these GWs could arise from inspiraling SMBHBs, with the characteristic strain following a $f^{-2/3}$ power law [323].

The detection process relies on recovering the HD correlation pattern [184, HD], which distinguishes it from the pulsar-correlated behaviour of noise sources such as pulsar spin noise,

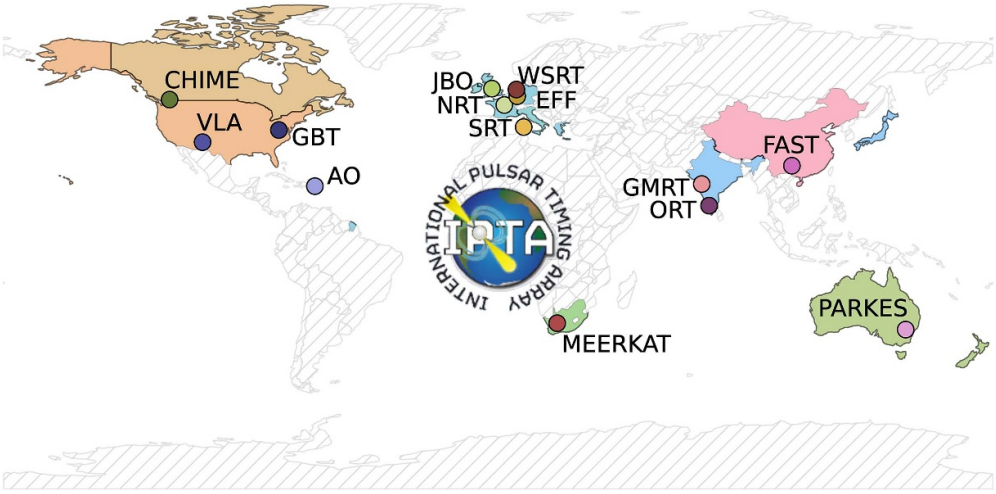

Figure 9. The IPTA combines data from the regional PTAs, coloured by the geographical regions within which their primary telescopes (filled circles) operate.

IISM effects, and SSE errors [392]. The sensitivity of a PTA to spatial correlations depends on the number and angular distribution of pulsars in the array and their timing stability [364]. Hence PTAs monitor many MSPs whose deterministic timing models leave residuals typically $\lesssim 1\,\mu$s and do not exhibit rapid variations (e.g. glitches or strongly varying orbital configurations).

Multiple collaborations operate long-term MSP monitoring campaigns worldwide. Currently there are six operational PTAs: the EPTA, NANOGrav, the PPTA, the InPTA, the CPTA and the MPTA. Because PTAs are tied to specific facilities, they are geographically constrained (see figure 9). The 'regional' PTAs combine data under the aegis of the IPTA. In the following (section 6) I summarise the latest datasets and per-PTA setup nuances; here I only provide a compact overview of instrumentation.

5.1. Telescopes and receivers of PTAs

Characterising receivers and backends requires significant effort and computational resources. While a minimal setup might appear attractive, the noise-model dependence of PTA datasets means diversity in observing systems is an effective way to detect or rule out systematics and to separate common red processes from instrument-specific effects. A summary of commonly used systems is provided in table 2. Detailed, per-PTA configuration and processing choices are deferred to section 6.

The EPTA employs a heterogeneous set of facilities across Europe, namely Effelsberg (100 m), Lovell (76 m), Nançay (94 m effective aperture), Westerbork (14×25 m dishes), and the Sardinia 64 m telescope. These operate across P-, L-, S- and C-bands with bandwidths ranging from $\sim$100 MHz to 500 MHz (see table 2). In combination, they form the large European array for pulsars (LEAP), which provides a coherent aperture equivalent to a single $\sim$194 m dish, used monthly for $\sim$20 pulsars. This diversity in systems provides a powerful check against instrumental systematics. Further detail on the receivers, backends and their calibration is given in the EPTA DR2 release [139].

Table 2. Summary of telescopes, receivers, operational centre frequencies, and bandwidths used by the different PTA collaborations.

PTA	Telescope	Receiver	Center frequency (MHz)	Bandwidth (MHz)
EPTA	Effelsberg	L-band	1350	1100–1600
	Effelsberg	S-band	2850	2600–3100
	Lovell	L-band	1500	1300–1700
	Nançay	L-band	1350	1100–1700
	Westerbork	P-band	350	310–390
	Westerbork	L-band	1500	1300–1700
	Sardinia	L-band	1550	1300–1800
	Sardinia	C-band	6500	5900–7100
InPTA	uGMRT	Band 3	400	300–500
		Band 5	700	550–850
NANOGrav	Green Bank	820 (P-band)	820	700–900
	Green Bank	1400 (L-band)	1400	1200–1700
	Arecibo	430 (P-band)	430	300–500
	Arecibo	1400 (L-band)	1400	1100–1700
	VLA	L-band	1500	1300–1700
PPTA	Murriyang	820 (P-band)	820	700–900
	Murriyang	1400 (L-band)	1400	1200–1700
MPTA	MeerKAT	L-band	1284	856–1712
		UHF-band	816	544–1088
CPTA	FAST	19-Beam L-band	1250	1050–1450
		Ultra-Wideband (UWB)	—	250–3000

The InPTA is centred on the upgraded giant metrewave radio telescope (uGMRT) in India, which consists of thirty 45 m dishes operated in phased-array mode. Observations are typically made in Bands 3 (300–500 MHz) and 5 (550–850 MHz), with bandwidths of 200 MHz routinely deployed. These low- and mid-frequency data are particularly effective for tracking DM variations, complementing the higher frequency ranges of other PTAs. The InPTA DR1 publication provides a full description of these observing strategies and backend systems [382].

NANOGrav relies on three major US facilities: the 100 m Green Bank Telescope, the 305 m Arecibo dish (until its collapse in 2020), and the 27×25 m dishes of the Very Large Array (VLA). Timing is performed mainly at 327, 430, 820 and 1400 MHz bands, with bandwidths that grew from tens of MHz with older backends to several hundred MHz with the later PUPPI/GUPPI systems (up to 800 MHz at the VLA). These systems together supported the 68 pulsars in the NANOGrav 15 year dataset, described in detail in [9].

The PPTA uses the 64 m Parkes 'Murriyang' telescope, with the ultra–wideband Low (UWL) receiver providing continuous coverage from 704–4032 MHz. This setup eliminates the need for multiple narrowband systems, though CASPSR and PDFB4 continue to operate at 820 and 1400 MHz for consistency with earlier releases. Typical cadences are three weeks on 24–30 pulsars, with median RMS residuals at or below $\sim1\,\mu$s. Full details of the receiver chain and processing are given in the PPTA DR3 release [433].

The CPTA is based at the Five-hundred-metre Aperture Spherical Telescope (FAST). Most observations use the central beam of the 19-beam L-band receiver (1050–1450 MHz), providing sub-μs RMS on bright MSPs such as PSR J1713+0747. A wideband receiver covering 250–3000 MHz is also available, extending spectral leverage for profile modelling and scattering studies. The observing cadence is bi-weekly for most pulsars, with higher-cadence campaigns for the most stable timers. Receiver and backend details are presented in the CPTA DR1 paper [423].

Finally, the MPTA makes use of the MeerKAT array in South Africa, comprising 64×13.5 m dishes phased for pulsar timing. Pulsars are observed in the L-band (856–1712 MHz) and UHF band (544–1088 MHz), with data recorded on the PTUSE backends. The coherent-dedispersion pipeline delivers sub-banded TOAs with typical uncertainties of $\sim$0.5–1 μs. This infrastructure underpins the expansion of the MPTA dataset to nearly 90 pulsars in its latest release [294].

6. The latest PTA data releases

This section summarises the major data releases made by the individual PTAs between 2023 and 2025, where each dataset showed significant evidence for an HD-correlated process. As PTAs tend to have significant variance in the methods used to observe and process the pulsar data, and in the choices of noise model components and other analysis steps, each data release is summarised separately. Instrumental specifics are outlined earlier (section 5) and in table 2.

6.1. EPTA (and InPTA) data release 2 (DR2)

The EPTA observatories run heterogeneous recording and processing in complex RFI environments, requiring extensive data curation and iterative noise modelling. To maximise sensitivity to a stochastic GWB, a source-selection scheme was adopted using the S/N_A^2 statistic [342, 369], enhanced by a coupling-matrix formalism [341, 369] to retain discrimination between HD, dipolar, and monopolar spatial correlations. This yielded 25 pulsars (from 42 in DR1) able to recover 90%–98% of the full-array sensitivity to a simulated GWB with amplitude 3×10^{-15} at $1\,\mathrm{yr}^{-1}$ and spectral index $\gamma=13/3$, while retaining $\geqslant$95% sensitivity to monochromatic sources. Instrumentation is summarised in section 5 and table 2.

- *Observations and instrumentation:* Data from six European facilities were combined, including LEAP observations (equivalent aperture $\sim$194 m at 1.4 GHz).
- *Data processing:* DR2 incorporated coherent-dedispersion backends, increasing bandwidth and sensitivity over legacy systems. Telescope-specific pipelines applied calibration and RFI excision (e.g. ROACH-based backends with polarisation calibration and median-filter/spectral-kurtosis methods; matrix template matching for Nançay).
- *TOA generation and timing:* `tempo2`-compatible ephemerides and TOAs were produced per telescope and transferred to a central repository. Combination used both standard manual procedures [119, 407] and a semi-automated scheme. For each pulsar, 'jumps' were fitted per sub-band/backend, using the NUPPI 1420 MHz sub-band as reference; discrete time offsets were corrected via the `TIME` keyword. Overlaps between legacy/new and LEAP/non-LEAP data were pruned to avoid duplication while retaining bands constraining DM.
- *Outlier removal/cleaning:* Automated and manual checks removed TOAs with residuals beyond 10 $\times$ the RMS and observations with calibration issues, corrupted polarisation, or systematic trends.

6.2. The InPTA data release 1

The InPTA first public release contains data products for 14 pulsars observed from 2018 to 2021, with `Tempo2`-compatible TOAs and DM variations derived via both narrowband and wideband techniques. Instrumental context is in table 2.

- *Observations and instrumentation:* Bi-weekly cadence using uGMRT phased subarrays for simultaneous multi-band observations. Early cycles used Bands 3/4/5 with 100 MHz bandwidth; later cycles used Bands 3/5 with 200 MHz bandwidth.
- *Data processing:* Most Band 3/5 data were coherently dedispersed using a real-time pipeline [117]. GWB data [339] were converted with `pinta` [379] to partially folded PSRFITS; folding used IPTA DR2 ephemerides [319]. RFI mitigation used RFIClean [269]. Backend delays dependent on observation settings were corrected via the `be:delay` header field and applied with `pat`/`pptoa`.
- *TOA/DM estimation and timing: Narrowband*—high-*S/N* templates (cycle 41), iterative handling of profile evolution and DM; sub-banded ToAs in Bands 3/5 with epoch DM from `DMcalc` [238]; final timing with `TEMPO2`. *Wideband*—fiducial DM from narrowband analysis; Band 3 portraits with PulsePortraiture [318] to jointly estimate ToAs/DMs, tuning eigenprofiles and channelisation for *S/N* vs. profile evolution.

6.3. The NANOGrav 15 year data set

The NANOGrav 15 year data set includes narrowband and wideband TOAs and parameterised timing models for 68 pulsars, with configuration files for timing analysis notebooks and additional support files (e.g. telescope clock offset measurements). Raw telescope data products and analysis code are also available from the same repository. Instrumentation is summarised earlier (section 5; table 2).

- *Scope:* Timing data for 68 MSPs (an increase of 21 from NG12). Pulsars with suitable timing precision ($\leqslant 1\ \mu$s scatter in daily-averaged residuals) were added to the regular schedule. Short baselines were excluded as they do not significantly contribute to low-frequency GW detection.
- *Data processing:* Standardised steps produced calibrated profiles and TOAs:

  (i) Exclusion of corrupted/unusable files.
  (ii) Removal of artefacts from the analogue-to-digital converter scheme used by (*P/G*)UPPI receivers.
  (iii) RFI excision and calibration.
  (iv) Time/frequency averaging into 1.6–32 MHz channels and sub-integrations up to 30 min.

- *TOA generation and timing:* TOAs were generated via profile–template time-shift measurements; parameterised timing models are provided alongside TOAs.
- *Outlier removal/cleaning:* Automated outlier identification and removal in residuals, followed by additional quality checks. After final cuts, the narrowband data set contained 676 465 TOAs (34.6% cut), and the wideband set contained 20 290 TOAs (21.6% cut).

6.4. The Parkes PTA

The PPTA Data Release Three (PPTA DR3) includes reprocessed data from previous releases along with new UWL receiver observations (see table 2). In this release, narrowband pulsar timing is employed, where TOAs are derived from sub-banded data using frequency-dependent pulse portraits. This approach allows for the correction of DM variations while accounting for the intrinsic frequency dependence of the pulse profiles. It also unifies legacy and UWL data. DR3 includes calibrated pulse profiles and dynamic spectra of recent observations.

The majority of the observations in PPTA DR3 were recorded using the Medusa astronomy signal processor, which coherently dedisperses the data stream and folds the data at the known pulsar period. The raw data files produced are relatively large, so they are split into three time segments for easier archiving. In the data processing pipeline, these segments are combined back into a single observation file for each observation. When Medusa was not available, legacy backends (CASPSR, PDFB4) were used as fallback systems and to measure timing offsets relative to UWL for continuity. While 95% of the observations were recorded between MJD 58256 and 58752 (18 May 2018 to 26 September 2019), some observations with earlier instruments continued until the end of the dataset, enabling direct comparison of legacy and UWL data.

- *Scope and key features:* 25 pulsars described in earlier PPTA papers are included, with one (PSR J1732−5049) excluded due to high uncertainties. Six new binary pulsars and one solitary pulsar are added after commissioning the UWL receiver.
- *Observing and calibration (instrumentation in table 2):* The UWL system replaced the earlier multi-receiver strategy for DM correction. Sessions include calibration with a nearby reference position and observations of a primary flux calibrator. Data were recorded in PSRFITS and processed primarily with Medusa, with CASPSR/PDFB4 used where necessary.
- *Data processing:* PFITS and PSRCHIVE were used for UWL observations. RFI flagging employed PFITS and MeerGuard. UWL data were split into eight bands to align with previous releases, each further divided into sub-bands for timing.
- *TOA generation and timing:* ToAs were formed by cross-correlating idealised profile templates with each observation. Wideband profiles were generated, and ToAs were measured using Fourier-domain Monte Carlo (FDM) within PSRCHIVE.
- *Outlier removal/cleaning:* Median ToA uncertainties range from nanoseconds to microseconds across pulsars. Timing residuals were initially formed using previously published ephemerides, and observations with poor *S/N* were excluded.

6.5. CPTA data release 1

The CPTA DR1 contains TOAs and timing models for 57 pulsars [423]. The dataset spans April 2019 to September 2022 with observations using the FAST central L-band beam (see section 5; table 2). Most MSPs were observed approximately every two weeks; for PSR J1713+0747, post–MJD 59319 data were excluded due to an abrupt profile-change event [211, 240, 365, 422].

- *Observations and instrumentation:* FAST central beam in the 1.0–1.5 GHz range; cadence typically fortnightly with higher cadence for the most stable timers.

- *Data processing:* Search-mode ROACH2 recording, folded offline into 30 s sub-integrations with DSPSR [404]; RFI cleaning, polarisation calibration, and integration with PSRCHIVE [199]. Final products typically have 64 frequency channels (∼7.8 MHz); two pulsars were reduced to 16 channels to manage data volume.
- *TOA generation and cleaning:* Final profile integrations were usually 20 min or $< 2.5\%$ of the binary period. TOAs were generated by cross-matching against standard total-intensity templates; sub-integrations with *S/N* < 8 were removed ($< 5.2\%$ of total).

6.6. The MPTA data release 2

The MPTA operates under the MeerTime LSP [36, 37], utilising the MeerKAT telescope (instrumentation in table 2). The dataset spans February 2019 to August 2024 (MJD 58526 to 60157).

- *Observations and instrumentation:* L-band receiver (856–1712 MHz) with PTUSE backends [37]. Integration times were tuned per pulsar to reach a band-averaged uncertainty of 1 μs. If achievable faster, a standard 256 s integration was used to increase sample size [370], improving sensitivity to a stochastic GWB [364].
- *Data processing:* Coherent dedispersion at a nominal DM and folding at the topocentric period. PSRFITS archives [199]—8 s sub-integrations, 1024 phase bins, four polarisations. Early data used 928 channels; later 1024. The `meerpipe` pipeline applied RFI excision via `meerguard` (a `coastguard` variant [247]). For 1024-channel data, the outer 48 MHz at each band edge were discarded to align with 928-channel data and remove bandpass roll-off. All observations were averaged to 32 frequency channels for this release. Observations longer than 3000 s were split to match the median length per source to avoid timing-model errors.
- *TOA generation and timing:* Arrival times were measured with the FDM algorithm in PSRCHIVE [199], using PulsePortraiture templates [318] at 32-channel resolution.
- *Outlier removal/cleaning and release contents:* TOAs with *S/N* < 8 were dropped (∼10% of measurements). The release expands the sample to 83 pulsars (from 78 in [293]) and includes 245,907 arrival-time measurements with a median sub-banded uncertainty of 3.1 μs (band-averaged ∼0.5 μs). Products include `Tempo2`-compatible TOAs and uncertainties, IPTA metadata [193], profiles and portraits, and the ephemerides used (DE440; BIPM 2022 TT). Three pulsars were excluded for poor timing precision (PSR J1103−5403—excess white noise [304]; PSR J1756−2251—strong timing noise [148]; PSR J1705−1903—orbital phase-dependent noise [302]). Eight new pulsars were added: PSRs J0101−6422, J1231−1411, J1514−4946, J1804−2717, J1804−2858, J1843−1448, J1911−1114, and J2236−5527.

6.7. The third data release of the IPTA

Across the individual data releases summarised in table 3, sensitivity at the lowest GW frequencies is set primarily by time span: The EPTA+InPTA DR2 $\sim$ 24.5 yr of data to reach $f_{\mathrm{GW,\,low}} \approx 1.3$ nHz whereas NANOGrav's 15.9 yr spans 1.99 nHz and the shorter modern arrays (InPTA, MPTA) sit at $\gtrsim$ 7–9 nHz. Sample size varies: CPTA (57), NANOGrav (68) and MPTA (88) deliver the largest single-PTA pulsar counts, while PPTA DR3 (24) and EPTA + InPTA DR2 (25) trade numbers for long, well-calibrated baselines and ultra-wideband coverage. Radio frequency ranges are complementary: PPTA's UWL (704–4032 MHz) fills the high-frequency gap, MPTA covers 856–1412 MHz, and InPTA supplies the low-frequency

Table 3. Summary of PTA datasets, number of pulsars, time spans, gravitational wave lower frequency limits, and radio frequency ranges.

PTA	Dataset	PSRs	Tspan (years)	$f_{\rm GW,low}$ (nHz)	$f_{\rm radio}$ (MHz)
EPTA	DR2	25	24.5	1.29	283–5107
NANOGrav	15 yr	68	15.9	1.99	302–3988
PPTA	DR3	24	18.1	1.75	704–4032
CPTA	DR1	57	2.3	13.8	1050–1450
InPTA	DR1	15	3.5	9.05	300–1460
MeerKAT	DR2	88	4.5	7.04	856–1412
IPTA	DR3	121	∼25	1.29	30–5107

Table 4. Summary of PTA data.

PTA name	Total pulsars $T_{\rm span}$ (yr)	Median	Median TOA precision (μs)
NANOGrav	68	$7.6^{+8.3}_{-5.2}$	$0.5^{+2.6}_{-0.5}$
EPTA + InPTA	25	$16.1^{+2.5}_{-8.4}$	$2.8^{+2.5}_{-8.5}$
PPTA	28	$26.3^{+8.4}_{-1.8}$	$2.4^{+2.3}_{-7.7}$
CPTA	57	$2.2^{+1.1}_{-1.3}$	$1.0^{+0.1}_{-0.2}$
MPTA	88	$3.8^{+0.7}_{-0.5}$	$0.8^{+0.1}_{-0.6}$

leverage (300–1460 MHz). Median ToA precisions in table 4 indicate sub-μs performance for the largest modern sets – NANOGrav, MPTA and the FAST-driven CPTA – with EPTA + InPTA and PPTA showing $\sim$ few-μss medians reflecting heterogeneous legacy content and long baselines. In short, the arrays are complementary: NANOGrav and MPTA contribute scale and uniformpipelines, PPTA anchors wideband calibration, CPTA provides extreme S/N on key MSPs, and InPTA supplies low-frequency DM sensitivity.

Leveraging this complementarity to increase PTA sensitivity to unprecedented levels, the forthcoming third data release of the IPTA(IPTA-DR3) combines the data from each, to obtain a time span of ∼25 yr, with 130 pulsars to reach $f_{\rm GW,\,low} \approx 1.26$ nHz. Along with the long lever arm (lowest f_{GW}), the IPTA-DR3 will combine the differing distributions of MSPs in each PTAs shown in figure 10 to maximise the sky coverage obtained.

Across the individual data releases, sensitivity at the lowest GW frequencies is set primarily by time span: IPTA DR3 combines ∼25 yr and 121 pulsars to reach $f_{\rm GW,low} \approx 1.29$ nHz (matching EPTA's DR2 lowest bin), whereas NANOGrav's 15.9 yr spans 1.99 nHz and the shorter modern arrays (InPTA, MPTA) sit at $\gtrsim$7–9 nHz. Sample size varies: NANOGrav (68) and MPTA (88) deliver the largest single-PTA pulsar counts, while PPTA DR3 (24) trades number for long, well-calibrated baselines and ultra-wideband coverage. Radio frequency ranges are complementary: PPTA's UWL (704–4032 MHz) fills the high-frequency gap, MPTA covers 856–1412 MHz, and InPTA supplies the low-frequency leverage (300–1460 MHz). Median ToA precisions in table 4 indicate sub-μs performance for the largest modern sets (NANOGrav, MPTA) and FAST-driven CPTA, with EPTA + InPTA and PPTA showing ∼few-μs medians reflecting heterogeneous legacy content and long baselines. In short, the arrays are complementary: IPTA aggregates the long lever arm in time (lowest $f_{\rm GW}$), NANOGrav and MPTA contribute scale and uniform pipelines, PPTA anchors wideband calibration, CPTA provides extreme *S/N* on key MSPs, and InPTA supplies low-frequency DM sensitivity.

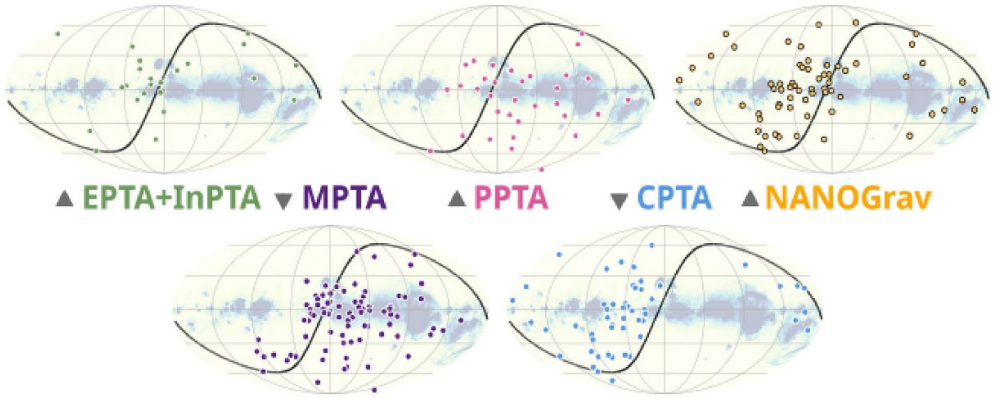

Figure 10. Sky locations of the pulsars currently in the datasets of PTAs.

7. PTA results

In June 2023, 4 PTAs released the strongest evidence till date for the presence of a nHz GWB, followed by the MPTA in 2025. Figure 11 presents a summary of all published determinations of the GW strain amplitude, when modelled a simple power law, referred to a frequency of 1/year.

These results, while appealing, require careful interpretation. For instance, all PTAs rely on modelling the significant noise terms in the individual pulsars as a power law, with or without chromaticity. This implies that without independent means of confirmation, or in the absence of sensitive data, the RN and DM noise models can exchange power between them. This is especially concerning, as portions of the individual pulsar red noise can appear as a common process [432] although detailed simulations demonstrate that this does not impact the detectability of GWB, only introducing some small biases in the recovered maximum likelihood estimates of the power laws used to describe the GWB [159].

Further, while the posteriors on the GWB can be compared to some degree, the final estimates reflect many systematic properties unique to the data collecting and processing employed by each PTA. In other words, while the agreement between PTAs is quite good, interpreting any differences is difficult as it necessitates disentangling the contributions from difficult to diagnose PTA-specific systematics.

EPTA and InPTA power-law search and GWB analysis

EPTA+InPTA reported results using the data set named EPTA DR2new+. This set comprises 10.3 years of EPTA observations for 25 pulsars, with an additional 3.5 years of InPTA observations for 10 of these pulsars, spanning a total of about 11 years. Legacy EPTA data was excluded due to the limitations of narrow radio bandwidths and potential contamination of GWB signals by the covariance between DM variations and achromatic red noise. EPTA+InPTA reported a Bayes factor (BF) of about 60 in favour of HD correlated GWB over common uncorrelated red noise (CURN), corresponding to a false-alarm probability of $\sim 10^{-3}$ (3σ). Assuming a power law with a fixed spectral index of 13/3, they recovered an amplitude of $(2.5 \pm 0.7) \times 10^{-15}$ at a reference frequency of 1 yr^{-1} (median and 90% confidence interval).

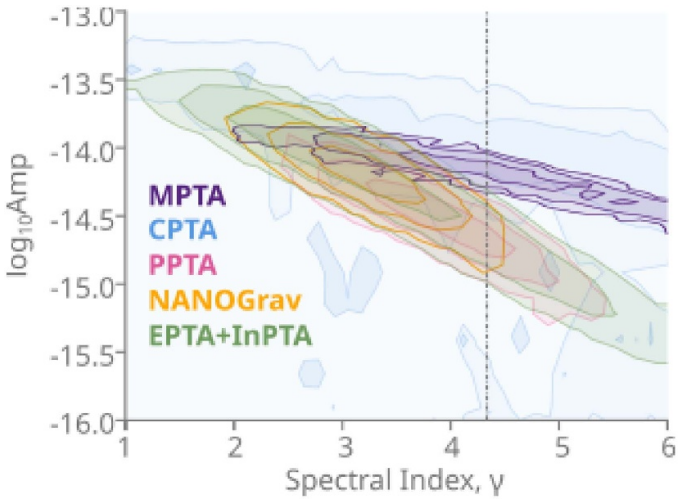

Figure 11. Comparision of the 2D posteriors on the amplitude and spectral of a common, correlated process in the datasets of five PTAs.

The EPTA conducted a search for a GW signal using their most constraining data, the DR2new+ dataset. In their analysis, (Lentati *et al* [252]) they focused on a power-law search, estimating the amplitude (A) and spectral index (γ) of the signal at a reference frequency of $1/10\,\mathrm{yr}^{-1}$. Working at this frequency helps reduce the degeneracy between these parameters, improving the precision of the constraints.

The team fit their model to the nine most constraining low-frequency bins, comparing the results to various phenomenological models [342, such as those by]. The study also explored accretion effects on SMBHBs, examining scenarios of equal Eddington accretion for both black holes or preferential accretion on the secondary black hole. These scenarios are informed by empirical relations between galaxies and SMBHBs, [167, 230, 282, such as those by].

In exploring possible SMBHB populations, EPTA trimmed down to around 108 ad-hoc models, preserving the broad properties of the full set. This allowed for an efficient search while maintaining consistency with astrophysical observations.

NANOGrav 15 year data set

NANOGrav analysed its 15 year data set, which contains observations of 68 pulsars (excluding one with less than 3 years of observations). The reported BF was approximately 200 in favour of HD-correlated GWB over CURN, with a false-alarm probability ranging between 10^{-3} and 5×10^{-5} (3σ–4σ), depending on the background estimation method. Assuming a power law with a fixed spectral index of 13/3, NANOGrav recovered an amplitude of $(2.4^{+0.6}_{-0.7}) \times 10^{-15}$ at a reference frequency of 1 yr^{-1} (median and 90% confidence interval).

The NANOGrav 15 year data set provides evidence for a stochastic GWB based on timing residuals that were correlated across 67 pulsars. The correlations fit the HD pattern is expected for such a background. A Bayesian analysis showed overwhelming support for a GWB model with a power-law spectrum, with a BF exceeding 10^{14} compared to a model with independent pulsar noise. When comparing the GWB model to a simpler uncorrelated common power-law spectrum model, BFs ranged from 200 to 1000 depending on the spectral modelling approach.

In addition, a frequentist analysis was conducted using a weighted sum of inter-pulsar correlations, yielding p-values between 5×10^{-5} and 1.9×10^{-4}, corresponding to significances between 3.5σ and 4σ. This further supported the presence of a common correlated signal in the pulsar timing data.

The inferred GW signal, consistent with a power-law spectrum proportional to $f^{-2/3}$, matches the expected signal from a population of SMBHBs. The strain amplitude, when evaluated at a reference frequency of $1\,\mathrm{yr}^{-1}$, lies within the 90% credible interval predicted for such a signal. Although this is consistent with astrophysical models for SMBHBs, alternative cosmological sources cannot yet be excluded.

PPTA DR3 and anisotropic GWB search

PPTA used the third data release of their observations, consisting of 32 pulsars over an 18 year span. Two pulsars were excluded due to data insufficiency and steep red noise. A BF of approximately 1.5 in favour of HD-correlated GWB over CURN was reported, with a false-alarm probability of 0.02 (2σ). Assuming a power law with a fixed spectral index of 13/3, PPTA recovered an amplitude of $(2.0^{+0.2}_{-0.3}) \times 10^{-15}$ at a reference frequency of 1 yr^{-1} (median and 68% confidence interval).

The PPTA DR3 was first used to search for an isotropic stochastic GW background. This involved measuring the characteristics of a common-spectrum process across the pulsar array. Using only pulsar autocorrelations and the DE440 SSE, the amplitude of the common-spectrum process was determined to be $\log_{10} A_{\mathrm{CRN}} = -14.51$ and the spectral index $\gamma = 3.87$. When marginalizing over possible SSE errors, the amplitude was slightly steeper, at $\log_{10} A_{\mathrm{CRN}} = -14.56$ and $\gamma = 4.02$, though evidence for these errors was weak.

For a fixed spectral index of $\gamma = 13/3$, the amplitude was found to be $\log_{10} A_{\mathrm{CRN}} = -14.69 \pm 0.05$, translating to a strain amplitude of $A = 2.04^{+0.25}_{-0.22} \times 10^{-15}$ for an isotropic GWB. A new technique analysing only the spatial correlations indicated consistency with an isotropic GWB at this amplitude, with a false-alarm probability of $p \lesssim 0.014$, corresponding to approximately 2σ significance.

However, some characteristics of this common-spectrum process raise questions under the assumption of an isotropic GWB. Three pulsars disfavour a $\gamma = 13/3$ process at the measured amplitude, suggesting that the common-spectrum process might not act like a noise floor typical of a GWB. These pulsars seem to contribute positively to HD correlations when the common noise is introduced, potentially indicating issues in the pulsar noise models.

Additionally, the amplitude of the common noise appears to vary over time, which cannot be fully explained by increasing sensitivity. Early parts of the dataset placed upper limits on the amplitude, which are in tension with the current measurements. Similar nonstationarity issues have been observed in previous searches by NANOGrav and PPTA, but the significance of this tension is debated due to differences in datasets and analysis methods.

Furthermore, there is no Bayesian support for HD correlations when both autocorrelations and cross-correlations are analysed. However, when using cross-correlations alone, there is some model support ($\Delta \log_{10} \mathcal{L}^{\mathrm{HD}}_{\mathrm{CRN}} = 1.1$) for the HD spatial correlations, with a significance consistent with the earlier p-value.

Some of these anomalies may be explained by invoking anisotropy in the SMBHB population, as simulations suggest significant variance in the GWB spectrum [342]. The recovered amplitude of the common noise is near the maximum expected for a GWB originating from SMBHBs [431]. Eccentricity in nearby sources or unresolved local populations may also explain the apparent nonstationarity in the noise. Further analyses involving larger datasets,

such as those from the IPTA, may help resolve these questions and strengthen the significance of any observed spatial correlations.

The CPTA DR1 and GWB search

CPTA inferred a GWB characteristic amplitude of $\log A_{\rm c} = -14.4^{+1.0}_{-2.8}$ for a spectral index in the range $\alpha \in [-1.8, 1.5]$ and $\log A_{\rm c} = -14.7^{+0.9}_{-1.9}$ when fixing $\alpha = -2/3$. The statistical significance of the HD correlation over a constant-value correlation was 4.6σ (P-value of 4×10^{-6}) around 14 nHz. However, the data could not distinguish between different models of SMBHB formation and evolution due to the short time span of the CPTA data. A Bayesian analysis preferred HD correlation with a BF of 66 over a dipole correlation.

The inferred characteristic GWB amplitude is $\log_{10} A_{\rm c} = -14.4^{+1.0}_{-2.8}$ for a spectral index in the range $\alpha \in [-1.8, 1.5]$, and $\log_{10} A_{\rm c} = -14.7^{+0.9}_{-1.9}$ when α is fixed at $-2/3$. These measurements are consistent with theoretical predictions [285, 352], but due to the short data span, it is not possible to distinguish between different models of SMBHB formation and evolution.

While the GWB amplitude aligns with signals detected by other PTAs, it appears 0.4–0.5 dex higher. There is speculation that a single power-law model with $\alpha = -2/3$ may not fully describe the GWB, particularly at higher frequencies observed by CPTA, suggesting the possibility of a spectral 'bump' around 10^{-8} Hz. The statistical significance of the HD correlation is 4.6σ at around 14 nHz, with a p-value of 4×10^{-6}.

To infer spatial correlations, the authors measured pulsar pairwise correlations at single frequencies, bypassing assumptions about the GWB spectral shape. This method, which is not affected by uncorrelated noise or clock errors, shows limited statistical significance due to the focus on single frequencies. Future work aims to integrate multiple frequencies to improve the accuracy of the spectral index measurement.

The current analysis cannot completely rule out a dipole origin of the correlations, though Bayesian methods show a preference for the HD correlation with a BF of 66 in favour of HD over dipole models. Although the statistical significance of CPTA DR1 is still below the IPTA detection threshold of 5σ, independent regional PTA results may confirm these findings. The CPTA plans to join the IPTA in the future, which is expected to improve sensitivity, and the upcoming CPTA DR2 in 2026 should provide more accurate GWB parameter estimates. These efforts signal the opening of the nHz GW observation window.

Searching for the GWB in the MPTA DR2

The MeerKAT PTA (MPTA) reported varying results depending on noise modelling. When assuming a common achromatic signal with HD correlations, the recovered amplitude was $\log_{10} A_{\rm HD} = -14.28^{+0.23}_{-0.30}$ at a spectral index of $\gamma = 1.00^{+4.50}_{-0.93}$. However, no significant support for HD correlations was found, with $\log_{10}$ BFs suggesting ambiguity in favouring HD correlations. Their best-fit signal under the most significant model had an amplitude of $h_{\rm c,yr} = 7.5^{+0.8}_{-0.9} \times 10^{-15}$, which decreased when evaluated at $\alpha = -2/3$.

While the first MPTA data release (Miles *et al* 2024) found a CURN signal in the data, with a power-law amplitude $\log_{10} A^{\rm ER}_{\rm CURN} = -14.25^{+0.21}_{-0.36}$ and spectral index $\gamma^{\rm ER}_{\rm CURN} = 3.60^{+1.31}_{-0.89}$. A frequentist analysis using the DATA model measured a signal-to-noise ratio (*S/N*) of 4.6 for an all-sky angularly correlated signal, with a characteristic strain amplitude of $\log_{10} A^{\rm DATA}_{\rm CURN} = -14.12^{+0.04}_{-0.05}$. Various models (ER, ALT) provided slightly different results, but none had high enough *S/N* for further frequentist analysis.

Table 5. Summary of Bayes factors and detection significances for various PTAs.

PTA	Bayes factor (HD/CURN)	Detection significance (σ)
EPTA+InPTA	$\sim$60	3
NANOGrav	$\sim$200	3–4
PPTA	$\sim$1.5	2
CPTA	$\sim$66 (HD/Dipole)	4.6
MPTA	$<$13.4 (upper limit)	N/A

7.1. Summary

Taken at face value, the BFs in table 5 show the strongest HD-versus-CURN preference in the NANOGrav ($\sim$200; 3–4σ) and EPTA+InPTA ($\sim$60; $\sim$3σ) analyses, with CPTA reporting a similar strength but for a different comparison (HD versus dipole; $\sim$66; 4.6σ). PPTA's evidence is marginal (HD/CURN $\sim$1.5; $\sim$2σ), and MPTA is inconclusive ($<$13.4; no quoted significance). The heterogeneity matters: the quoted Bayes factors compare different pairs of models (HD/CURN or HD/dipole) and use PTA-specific processing and priors, so they are not strictly commensurate. Nonetheless, the pattern is consistent with an emerging HD-correlated process across multiple PTAs, with significance set by each array's time span, number of pulsars, and cleaning choices discussed above.

8. Comparing three PTA results through the IPTA

The results from the three of the PTA collaborations; NANOGrav, EPTA+InPTA and PPTA were further compared and contrasted under the aegis of the IPTA. As indicated in the resulting article [390], the analysis makes use of several simplifying assumptions and does not provide the expected sensitivity of the upcoming third data combination of the IPTA will. Further, this investigation is built on techniques such as factorised likelihood analyses and 'simple' noise models to allow for a rapid assessment. However, it does allow us to investigate several features of the results from individual PTA results.

To assess the compatibility of the estimates of the power law model parameters of the GWB, their posterior distributions have been previously compared using the Mahalanobis distance, assuming multivariate Gaussian distributions [21]. However, such distance measures often rely on comparing the one-dimensional histograms of the parameter values leading to a loss of information and subsequent incorrect estimation of the agreement (or lack thereof) between the final posteriors. In [390], a more sophisticated tension metric [334], is used to assess the tension between posterior distributions in a non-Gaussian framework. This method creates a 'difference distribution' between posteriors and evaluates the probability that the difference is zero, converting this into a Gaussian-equivalent σ value.

A comparison of GWB parameters was performed using this method, particularly focusing on the spectral slope, γ, and the characteristic amplitude, $A_{\log_{10}}$. By combining the posterior distributions from EPTA+InPTA, NANOGrav, and PPTA, improvements in parameter estimation were achieved, albeit without fully accounting for dependencies due to shared pulsars across PTAs. Visual representations of these posterior distributions, including power-law fits consistent with the GWB data, confirm a good agreement between the different PTAs, with tensions measured to be less than 1σ across all comparisons, demonstrating strong consistency.

When evaluating the sensitivity of each PTA to the GWB, sensitivity curves offer a robust metric to assess detector performance. These curves, computed using the `hasasia` package [179], highlight how each PTA's sensitivity varies with frequency. NANOGrav, with its larger pulsar count, exhibits superior mid-frequency sensitivity, while EPTA+InPTA and PPTA, with their higher observational cadences, show better performance at higher frequencies. The longer timing baselines of the latter ($\sim$24.5 and $\sim$18 yr, respectively) also allow them to probe slightly lower frequencies than the NANOGrav 15 yr dataset.

A standardised noise model was applied across all PTAs to facilitate a fair comparison of GWB properties, focusing on the CURN amplitude. The factorised likelihood method allowed for efficient parallel analysis of individual pulsars, leading to the posterior distributions for the amplitude of CURN. The results showed broad agreement across the PTAs, with the new estimates aligning closely with the previously reported GWB amplitudes.

An additional analysis using dropout factors (DFs) assessed the contribution of individual pulsars to the common signal. This cross-validation technique revealed that many pulsars had DFs close to unity, indicating their support for the common signal. However, discrepancies for some pulsars, driven by differences in observational time baselines, were also noted. Notably, pulsars like J1744−1134 exhibited tension with the common signal across different PTAs, raising questions about how noise modelling and observational differences affect results.

Finally, a comparison of inter-pulsar correlations using the optimal statistic method provided further insights into the detection significance of cross-correlated GWB signals. This method calculates the SNR (*S/N*) for GWB-induced inter-pulsar correlations. Across the PTAs, the results varied slightly due to differences in noise modelling approaches, with NANOGrav showing an increase in *S/N*, while EPTA+InPTA experienced a decrease. These variations highlight the sensitivity of results to noise models and the observational data used.

9. An astrophysical GWB from the cosmic population of SMBHBs

Having discussed the various PTA datasets and the significance of an HD-correlated signal in their datasets, we can now turn to the impacts of these results, starting with the implications for an SMBHB driven 'astrophysical' GWB. The cosmic population of SMBHBs is one of the main astrophysical sources expected to generate a nHz GWB detectable by PTAs. The GW strain squared $h_{\rm c}^2(f)$ from the ensemble is derived from the cosmic merger rate as a function of redshift z, primary mass m_1, mass ratio q, and eccentricity e:

$$h_{\rm c}^2(f) = \int_0^\infty {\rm d}z \int_0^\infty {\rm d}m_1 \int_0^1 {\rm d}q \, \frac{{\rm d}^5 N}{{\rm d}z\,{\rm d}m_1\,{\rm d}q\,{\rm d}e\,{\rm d}\ln f_{{\rm K},r}} \times \frac{{\rm d}t_r}{{\rm d}\ln f_{{\rm K},r}} \, h^2\left(f_{{\rm K},r}\right) \sum_{n=1}^{\infty} \frac{g\left(n, e\left(f_{{\rm K},r}\right)\right)}{(n/2)^2}\Bigg|_{f_{{\rm K},r}=\frac{(1+z)f}{n}}, \tag{67}$$

where $f_{{\rm K},r}$ is the Keplerian orbital GW frequency in the source frame.

Including environmental interactions and eccentricity gives [351]:

$$h_{\rm c}^2(f) = \int_0^\infty {\rm d}z \int_0^\infty {\rm d}m_1 \int_0^1 {\rm d}q \, \frac{{\rm d}^5 N}{{\rm d}z\,{\rm d}m_1\,{\rm d}q\,{\rm d}e\,{\rm d}\ln f_{\rm K}} \, h^2\left(f_{\rm K}\right) \sum_{n=1}^{\infty} g(n,e) \left(\tfrac{n}{2}\right)^2. \tag{68}$$

For a simplified circular, GW–driven binary population it reduces to [356]:

$$h_{\rm c}^2\left(f\right)=\int_0^\infty {\rm d}z\int_0^\infty {\rm d}\mathcal{M}\,\frac{{\rm d}^3N}{{\rm d}z\,{\rm d}\mathcal{M}\,{\rm d}\ln f_r}\,h^2\left(f_r\right), \tag{69}$$

where $\mathcal{M}$ is the chirp mass and $f_r=(1+z)f$.

Assuming circular binaries driven purely by GW emission (i.e. no environmental coupling) yields [323]:

$$h_{\rm c}^2\left(f\right)=\frac{4\,G^{5/3}}{3\,\pi^{1/3}\,c^2}\,f^{-4/3}\int_0^\infty {\rm d}\mathcal{M}\int_0^\infty {\rm d}z\,\left(1+z\right)^{-1/3}\,\mathcal{M}^{5/3}\,\frac{{\rm d}^2n}{{\rm d}z\,{\rm d}\mathcal{M}}, \tag{70}$$

giving the canonical $h_{\rm c}\propto f^{-2/3}$ scaling.

Environmental coupling and eccentricity introduce deviations from this power-law. Broken power-law models calibrated on simulations are in [95, 224, 335, 357].

Typically, efforts group into:

- **Self-consistent theoretical models**: simulate full SMBHB evolution across cosmic time [208, 224, 356].
- **Empirical models**: infer rates from observed galaxy pairs and SMBH–host relations [342, 353].

Of the four PTAs that presented results in 2023, only two [11, 142] have presented further interpretation of the constraints on the constrained GWB signal. Overall, all the PTAs appear to detect a GWB that follows a simple power law dependence on the GW frequency. However, as shown in figure 12, the recovered amplitudes of the GWB are far louder than expected from theoretical considerations [111, 208, 349, 358, 366]. Similarly, the spectral index for the power law fit is also flatter than that predicted for a background generated by an ensemble of nearly circularised SMBHBs. Similarly, the spectral index could also be explained by invoking more efficient gas accretion processes that lead to a larger number of MBHs with masses greater than $10^9 M_\odot$ The observed, mild tension can be explained by invoking a larger fraction of eccentric binaries. At the same time, the background could also be attributed to a number of cosmological sources as well as to a variety of exotic physics as the BFs for either choice of models appear to be roughly equal.

9.1. Astrophysical implications from the EPTA DR2

While the recovered amplitude is somewhat loud and the spectral index flatter than that expected the EPTA DR2 results are consistent with theoretical predictions of SMBHB populations, with signals dominated by binaries interacting with their stellar environments and exhibiting non-circular orbits.

Further, the EPTA DR2 compares predictions from models incorporating environmental effects, eccentricity, and more realistic accretion scenarios against the detected GWB signals. Notably, models considering pre-merger accretion and updated black hole-galaxy relations [230] tend to produce higher GWB amplitudes, matching the observed PTA signal better.

Beyond the standard analysis, the EPTA DR2 has also been used to consider the effect of a few discrete sources although a search for ‘continuous’ GW CGWs from individual SMBHBs is inconclusive but suggests that few nearby massive binaries may dominate the GWB signal. The probability of detecting such sources depends heavily on SNRs (S/N), and further observations may allow for the detection of these sources.

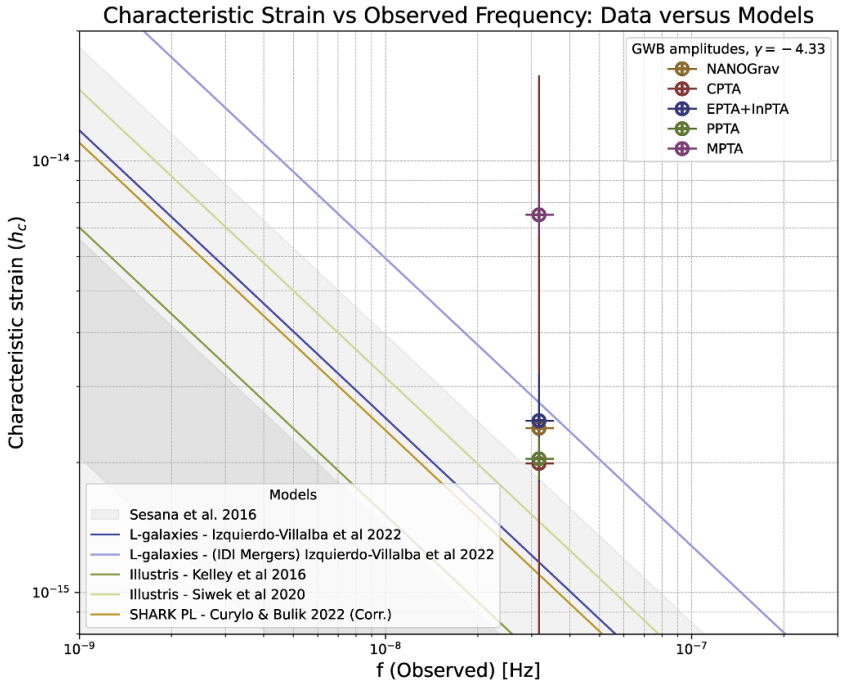

Figure 12. Figure shows the estimated GW strain amplitude at a reference frequency of 1/yr, when holding the spectral index of the GW power law fixed at −4.33. Also shown are predictions from a small number of astrophysical models relying on semi-analytical approximations using populations predicted by simulations of massive black hole binary mergers.

Using Bayesian inference, the EPTA DR2 has also been used to constrain the SMBHB mass function. Using the framework developed in [94, 96, 290] 'agnostic' and an astrophysically informed model were tested against the data, to refine our understanding of SMBHB mergers and their contribution to the observed GWB.

9.1.1. SMBHB population models

1. Agnostic SMBHB Model: This model assumes minimal prior knowledge about the population and describes the binary merger rates using a Schechter function for the redshift z and chirp mass $\mathcal{M}$. The five key parameters in this model include the merger rate $\dot{n}_0$, and parameters controlling the distributions of z and $\mathcal{M}$.
2. Astrophysically-Informed Model: This model incorporates more detailed astrophysical knowledge, including interactions between the binaries and their environment, and allows for eccentric orbits. It introduces 18 parameters, which describe the galaxy merger rates, stellar mass functions, and black hole-stellar bulge mass relations, among other aspects.

9.1.2. Inference results

- Merger rate density: the agnostic model provides weak constraints on $\dot{n}_0$, while the astrophysically-informed model shows that the PTA signal favours a higher merger rate density at the upper edge of the astrophysical prior.
- Chirp mass function: for both models, the PTA signal constrains the mass function of merging SMBHBs, with the astrophysically-informed model indicating that numerous mergers have occurred, particularly for massive binaries with chirp masses around $10^9 M_\odot$.
- Merger timescale and black hole-bulge mass relation: The astrophysically-informed model provides constraints on the merger timescale, suggesting that the SMBHBs have a relatively short merger time of less than 1 Gyr. Additionally, the PTA signal suggests a high normalization of the SMBH-bulge mass relation, implying efficient orbital decay following galaxy mergers.

These results suggest that compact SMBHBs are common in the centres of massive galaxies, indicating that the so-called 'final parsec problem' is solved in nature. The data also hint at eccentric binary orbits and dense environments, though these factors remain largely unconstrained.

9.2. The astrophysical implications of the NG 15 yr result

The results from NANOGrav 15 yr dataset have been probed using an extensive suite of simulations called `holodeck`. This package allows for selecting between two large classes of models. The first are phenomenological models which capture features such as the interaction of the binaries with their environment, variations in the number of SMBHBs contributing to each frequency bin, or the effects of orbital eccentricity. The second includes models where the binary evolution is driven by GW emission alone. These are referred to as the *Phenom* and *GWonly*, respectively with uniform (+Uniform) and astrophysically-informed (+Astro) prior. Similar to the techniques used for the EPTA DR2, `holodeck` starts from considerations of the merger rates and SMBHB mass function, and uses the selected model class to synthesise populations of SMBHBs. However, unlike the EPTA DR2, `holodeck` uses a Gaussian process interpolation scheme to calculate the power spectrum of the GWB [385]. This allows for a much faster evaluation of the effect of varying galaxy merger rates, governed by the galaxy stellar-mass function, the galaxy pair formation rate and the galaxy merger timescale. This also has the advantage that the generated spectrum captures the discrete distribution of the underlying GW sources, unlike the traditional simple power law approximation.

Combinations of the *Phenom* and *GWonly* models with the respective prior ranges are used to generate libraries of GWB spectra, which are then fitted to the spectrum obtained from the NANOGrav 15 yr 'free spectrum' analysis for an HD-correlated or CURN process (HD-w/MP+DP+CURN) [10]. Despite the broad range of model parameters fitted for, and the flexibility of the GP interpolation, the NANOGrav results are also broadly consistent with a background generated by populations of SMBHBs. In particular, the *Phenom* and *GWOnly* libraries both match the 15 yr HD-w/MP+DP+CURN free-spectrum posteriors, although the *GWOnly* model, limited to uniform priors, has more trouble matching the highest and lowest frequency bins. By contrast, *Phenom* exhibits a noticeable spectral turnover to align better with the data, especially under astrophysical priors (*Phenom+Astro*).

The 'GWOnly' library spectra, which resemble analytic estimates of SMBH binaries with $\gamma = 13/3$ (i.e. $\alpha = 2/3$), tend to be steeper than the bulk of the 15 yr data. Meanwhile, the 'Phenom' library's maximum-likelihood spectra and posterior draws show that a slight

turnover at low frequencies can better reproduce the 15 yr distributions. Nonetheless, these results remain consistent with $\alpha = 2/3$ power-law fits and the standard GW-driven evolution, indicating that the data neither rule out a turnover nor definitively confirm it.

9.2.1. Inference results.

- Merger rate density: The amplitude of the GWB inferred from the 15 yr data strongly prefers *efficient mergers* occurring in *high-mass* systems. In practice, this manifests as posterior distributions that push parameters such as the GSMF normalization (ψ_0) and the characteristic galaxy mass ($m_{\psi,0}$) toward higher values to boost the overall merger rate. When the binary lifetimes (τ_f) are longer, larger fractions of binaries can stall before entering the PTA band, leading to insufficient GWB amplitudes. Consequently, the *data disfavour very long lifetimes* and favour scenarios where a greater fraction of systems merge *in time* to contribute to the nHz GW frequency range. At the population level, the rate of SMBH binary mergers remains only *weakly constrained* at current sensitivity. Nonetheless, short merger timescales that elevate the total event rate, plus an abundance of high-mass galaxies in the low-redshift universe, appear crucial for reproducing the higher amplitudes in the 15 yr GWB spectrum.
- Chirp mass function: The 15 yr data indicate that *very massive SMBH binaries* ($M_{\rm tot} \gtrsim 10^{8.5}\,M_\odot$) dominate the GWB signal. At the lowest frequencies ($\sim$2 nHz), binaries can reach $M_{\rm tot} \gtrsim 10^{10}\,M_\odot$. Despite being rare, these high-mass binaries contribute most of the power in the GWB. Many lower-mass binaries also populate each frequency bin, but *the GWB is disproportionately shaped by the most massive systems*: for instance, binaries in the range $10^{9.2}$–$10^{10.4}\,M_\odot$ may constitute less than 0.1% of all emitting binaries at low frequencies yet produce $\sim$70% of the GWB amplitude there. As frequency increases (up to $\sim$20 nHz), binaries evolve more rapidly and the typical total mass contributing to the signal decreases. Even so, the *highest-mass tail* remains a critical driver of the overall GWB. The data allow for *flat or modestly turned-over* spectral shapes at low frequencies, consistent with a range of mass functions, but always emphasizing the leading role of high-mass SMBH binaries.
- Merger timescale and black hole-bulge mass relation: The posterior distributions strongly favour *short binary lifetimes* (τ_f) to achieve the high GWB amplitudes seen in the 15 yr data. Long-lived binaries would stall at separations above the PTA band, failing to accumulate enough total signal. This preference also drives higher values of galaxy stellar mass function parameters (ψ_0, $m_{\psi,0}$) to ensure sufficient overall mergers. The *MBH–$M_{\rm bulge}$ relation* (with normalization μ and scatter σ_μ) plays a key role in setting the typical black hole masses that enter the PTA band. Larger scatter (σ_μ) effectively increases the occurrence of ultra-massive SMBHs, contributing extra low-frequency power. Nonetheless, the posterior distributions remain broad, especially when comparing uniform versus astrophysical priors, indicating that current data cannot tightly pin down the precise BH–bulge scaling. Because the lifetime from $\sim$ nHz frequencies down to coalescence is much shorter than a Hubble time in most favoured scenarios, *a high fraction of SMBH binaries at lower redshifts* (i.e. $z \lesssim 0.25$) are expected to merge before the present epoch. In contrast, at higher redshifts, the fraction of binaries that can fully coalesce by today drops significantly, revealing that *merger timescales*—whether driven by environmental effects or GW emission—heavily shape the overall SMBH population evolution.

9.2.2. Population models and merger rates. SMBHB evolution is shaped by galactic mergers, which bring two SMBHs into close proximity. Different cosmological simulations, including Illustris, Millennium [371], TNG300, and ASTRID, have been used to model

SMBHB demographics and predict their gravitational wave contributions. These models suggest that SMBHB mergers peak at redshift $z \sim 2$, declining at lower redshifts. Results using the ASTRID simulation predict that SMBHBs with total masses in the range 10^9–$10^{10} M_\odot$ at $z \sim 0.3$ contribute the bulk of the SGWB [91], while work based on the TNG300 simulation estimates that SMBHB mergers contribute 70%–90% of the SGWB at low frequencies and 20%–30% at high frequencies [91]. The SHARK semi-analytical model, which accounts for gas-driven mergers, predicts a GW strain amplitude of $A^{\mathrm{yr}^{-1}} = (1.20\text{–}1.46) \times 10^{-15}$, which is about 50% lower than PTA observations [250] The Millennium simulation, incorporating dynamical friction and black hole interactions, predicts an SMBHB merger rate of $\sim 10^{-3}$–10^{-4} per cubic gigaparsec per year [280]. The SMBHB population also includes minor mergers ($q < 0.2$), which could contribute up to 40% of the total SGWB, a factor previously underestimated [91].

9.3. Black hole mass distributions and GW spectrum features

Recent PTA studies suggest a deviation from the expected power-law SGWB spectrum and a spectral break at ~ 26 nHz indicates a transition from a stochastic background to individual detectable SMBHB sources [91]. Allowing for an enhanced SMBHB merger rate at $z > 4$ increases the SGWB amplitude by 30%, aligning with JWST's discoveries of early massive galaxies [250].

10. GWs from individual SMBHBs

The SMBHBs in the relatively local universe that are expected to generate the stochastic GWB are in wide orbits with periods ranging from months to years, are far from merger and evolve slowly. Further, as discussed in the sections related to the interpretation of the GWB power-law model recovered from PTAs, the nHz GW spectrum is likely dominated by a few relatively nearby SMBHBs. Consequently, they emit GWs that are nearly monochromatic and appear as stationary in time. Thus searches for such CGW sources have also been carried out by a number of PTAs.

10.1. Detection concept and signal model

The concept of detecting GWs with PTAs was first formulated by Sazhin [350] and Detweiler [120]. The response of a PTA to a deterministic GW signal can be expressed as:

$$s_{\mathrm{a}}(t,\omega) = \int_0^t \frac{1}{2} \frac{\hat{p}_{\mathrm{a}}^i \hat{p}_{\mathrm{a}}^j}{1 + \hat{p}_{\mathrm{a}} \cdot \hat{\Omega}} \Delta h_{ij}(t')\, \mathrm{d}t', \tag{71}$$

where $\hat{p}_{\mathrm{a}}$ is the unit vector pointing to pulsar a, $\hat{\Omega}$ is the GW propagation direction, and h_{ij} is the GW strain tensor in the transverse-traceless gauge. The response depends on the GW strain at two distinct times: the time of emission and the time of reception:

$$\Delta h_{ij}(t) = h_{ij}(t - \tau_{\mathrm{a}}) - h_{ij}(t), \tag{72}$$

with

$$\tau_{\mathrm{a}} = L_{\mathrm{a}} \left(1 + \hat{\Omega} \cdot \hat{p}_{\mathrm{a}}\right), \tag{73}$$

where $L_{\rm a}$ is the distance to pulsar a. This time difference corresponds to the light travel time between Earth and the pulsar, adjusted by a geometrical factor. The timing residuals can thus be decomposed into two terms:

$$s_{\rm a}(t) = s_{p,a}(t-\tau_{\rm a}) - s_{e,a}(t), \tag{74}$$

where $s_{e,a}(t)$ and $s_{p,a}(t-\tau_{\rm a})$ are referred to as the Earth term and pulsar term, respectively.

The strain amplitude of a GW produced by a circular binary system is given by:

$$h_{ij}(t,\Omega) = \sum_{A=+,\times} e_{ij}^{A}\left(\hat{\Omega}\right) h_A(t), \tag{75}$$

where e_{ij}^{A} are the GW polarization tensors, defined as:

$$e_{ij}^{+}\left(\hat{\Omega}\right) = \hat{m}_i\hat{m}_j - \hat{n}_i\hat{n}_j, \tag{76}$$

$$e_{ij}^{\times}\left(\hat{\Omega}\right) = \hat{m}_i\hat{n}_j + \hat{n}_i\hat{m}_j, \tag{77}$$

with $\hat{\Omega} = -\sin\theta\cos\phi\,\hat{x} - \sin\theta\sin\phi\,\hat{y} - \cos\theta\,\hat{z}$, and the unit vectors:

$$\hat{m} = -\sin\phi\,\hat{x} + \cos\phi\,\hat{y}, \tag{78}$$

$$\hat{n} = -\cos\theta\cos\phi\,\hat{x} - \cos\theta\sin\phi\,\hat{y} + \sin\theta\,\hat{z}, \tag{79}$$

where (θ,ϕ) are the polar coordinates of the GW source's sky location.

Substituting these expressions into equation (71), the expected timing residuals in PTA data for a CGW signal from a circular SMBHB are:

$$s_{\rm a}\left(t,\hat{\Omega}\right) = \sum_{A} F^{A}\left(\hat{\Omega}\right)\left[s_A(t) - s_A(t-\tau_{\rm a})\right], \tag{80}$$

with:

$$s_{+}(t) = \frac{\mathcal{M}^{5/3}}{d_{\rm L}\omega(t)^{1/3}}\left[-\sin\left(2\Phi(t)\right)\left(1+\cos^2\iota\right)\cos 2\psi - 2\cos\left(2\Phi(t)\right)\cos\iota\sin 2\psi\right], \tag{81}$$

$$s_{\times}(t) = \frac{\mathcal{M}^{5/3}}{d_{\rm L}\omega(t)^{1/3}}\left[-\sin\left(2\Phi(t)\right)\left(1+\cos^2\iota\right)\sin 2\psi + 2\cos\left(2\Phi(t)\right)\cos\iota\cos 2\psi\right], \tag{82}$$

where $\mathcal{M}$ is the chirp mass, $d_{\rm L}$ is the luminosity distance, $\omega(t)$ is the orbital angular frequency, ι is the orbital inclination, ψ is the polarization angle, and $\Phi(t)$ is the GW phase.

The antenna pattern functions $F^{A}(\hat{\Omega})$ are given by [34, 131, 355, 386]:

$$F^{+}\left(\hat{\Omega}\right) = \frac{1}{2}\frac{\left(\hat{m}\cdot\hat{p}\right)^2 - \left(\hat{n}\cdot\hat{p}\right)^2}{1+\hat{\Omega}\cdot\hat{p}}, \tag{83}$$

$$F^{\times}\left(\hat{\Omega}\right) = \frac{\left(\hat{m}\cdot\hat{p}\right)\left(\hat{n}\cdot\hat{p}\right)}{1+\hat{\Omega}\cdot\hat{p}}, \tag{84}$$

where $\hat{p}$ is the unit vector pointing towards the pulsar.

Table 6. List of CGW parameters with their respective ranges. Uniform priors are typically assumed.

CGW Parameter	Range
$\log_{10} h$	$[-18,-11]$
$f_{\rm gw}$ (Hz)	$[10^{-9},10^{-7}]$
ϕ_0	$[0,2\pi]$
$\cos\iota$	$[-1,1]$
ψ	$[0,\pi]$
θ	$[0,\pi]$
ϕ	$[0,2\pi]$

10.2. Assumptions and simplifications

To make the analysis computationally feasible PTAs several simplifying assumptions, such as:

- **Neglecting the pulsar term:** The pulsar term is often neglected by considering it as part of the noise. This is justified if the source has evolved sufficiently over $\tau_{\rm a}$ to move the pulsar term off the Earth-term frequency. Including the pulsar term would improve parameter estimation but significantly increases the complexity of the likelihood surface and the dimensionality of the parameter space.
- **Non-evolving GW frequency:** The evolution of the GW frequency $\omega(t)$ over the observation time is typically neglected, assuming $\omega(t)=\omega_0$ is constant. This simplification is valid for sources where the frequency evolution is negligible during the observational timespan. Neglecting frequency evolution does not prevent detection but may introduce a bias in the measured GW frequency, potentially overestimating it [320].
- **Simplified phase evolution:** Under these assumptions, the GW phase simplifies to:

$$\Phi(t)=\omega_0 t+\phi_0/2, \tag{85}$$

  where ϕ_0 is the initial orbital phase.
- **Amplitude relation:** The GW amplitude h is related to the chirp mass $\mathcal{M}$, luminosity distance $d_{\rm L}$, and GW frequency $f_{\rm gw}$ by:

$$h=\frac{2\mathcal{M}^{5/3}(\pi f_{\rm gw})^{2/3}}{d_{\rm L}}. \tag{86}$$

10.3. Parameter space and priors

The model considers a single CGW source characterised by seven parameters, as summarised in table 6. Uniform priors are typically assumed for these parameters when conducting Bayesian analyses.

10.4. Data analysis methods

PTAs employ both Bayesian and frequentist frameworks to search for CGW signals. The methods involve modelling noise components, selecting pulsars, computing detection statistics, and setting upper limits.

10.4.1. Bayesian analysis and inference. In the Bayesian approach, PTAs sample the CGW parameters along with noise parameters for RN and DM variations. White noise parameters are often fixed, and the timing model and `BAYESEPHEM` parameters are marginalised over. Analyses are conducted both with and without a CRN component to assess its impact on the results.

MCMC samplers, such as `PTMCMC` [134], `Eryn` [221], and related implementations are commonly used in conjunction with software like `ENTERPRISE` [135] to construct models and compute likelihoods and priors. Empirical proposals based on prior noise explorations are used to improve sampling efficiency [14]. In addition, fast likelihood evaluators such as `QuickCW` [49] can be employed to accelerate parameter estimation.

10.4.2. Model selection and BFs. To determine whether the data favour the presence of a CGW signal, PTAs compute BFs comparing the null model (noise only) against a model including a CGW signal. The product-space (or hypermodel) approach [183] is often employed, where a hyperparameter indexes the models, and the BF is given by the ratio of the number of iterations the chain spends in each model:

$$\mathcal{B}^A_B = \frac{n_A}{n_B}, \tag{87}$$

where n_A and n_B are the counts of samples corresponding to models A and B, respectively. This method has been shown to yield reliable results [88]. Reversible Jump MCMC (RJMCMC) can also be used to allow transitions between models of differing dimensionality, ensuring detailed balance and a proper stationary distribution [50].

10.4.3. Upper limit setting. In the absence of a detection, PTAs proceed to set upper limits on the GW amplitude. This involves:

- Using MCMC with a uniform prior on $\log h$ within specified bounds.
- Computing the marginalised posterior probability distribution for the CGW amplitude $p(h)$.
- Determining the 95% upper limit h_{95}, defined by:

$$0.95 = \int_0^{h_{95}} p\,(h)\,\mathrm{d}h. \tag{88}$$

- Utilizing a grid of frequencies logarithmically spaced between 10^{-9} and 10^{-7} Hz.

Analyses are conducted both with and without the inclusion of CRN in the noise model.

10.4.4. Noise modelling. Accurate noise modelling is crucial for CGW searches. The noise in pulsar timing data is modelled as:

$$\delta t = \underbrace{\mathrm{M}\epsilon + n_{\mathrm{WN}} + n_{\mathrm{RN}} + n_{\mathrm{DM}} + n_{\mathrm{Sv}}}_{\mathrm{PSRN}} + \underbrace{n_{\mathrm{CRN}}}_{\mathrm{Common\,Red\,Noise}} + \underbrace{s}_{\mathrm{CGW}}, \tag{89}$$

where:

- $\mathrm{M}\epsilon$ represents timing model errors.
- n_{WN} is the white noise component, characterised by EFAC and EQUAD parameters.
- n_{RN}, n_{DM}, and n_{Sv} represent red noise, DM variations, and scattering variations, respectively.
- n_{CRN} is the common red noise component, which can model uncorrelated noise or an SGWB with HD correlations.

- s is the CGW signal.

PTAs often customize noise models for individual pulsars, adjusting the number of frequency bins and other parameters to best fit the data [88, 140].

10.4.5. Pulsar selection. Not all pulsars contribute equally to CGW sensitivity. PTAs select subsets of pulsars that recover the majority of the array's total SNR to CGWs. For example, selecting 21 pulsars out of 53 can recover approximately 95% of the total SNR [33, 88]. This reduces computational cost without significantly affecting results.

10.4.6. Frequentist analysis. In addition to Bayesian methods, PTAs employ frequentist approaches using detection statistics like the Earth term-only $\mathcal{F}_e$-statistic [34, 131]. This statistic is the log-likelihood maximised over 'extrinsic' CGW parameters for fixed intrinsic parameters.

To evaluate the significance of observed $\mathcal{F}_e$ values, PTAs may:

- Use the theoretical null distribution of $2\mathcal{F}_e$, which is a χ^2 distribution with four degrees of freedom under Gaussian noise assumptions.
- Perform sky shuffling, where pulsar positions are randomized to estimate the background distribution of $\mathcal{F}_e$ without assuming specific noise properties.

11. NHz GWB from cosmological sources

Having touched on the likelihood that the observed background and its relative tension with standard expectations, we might find it natural to discuss cosmological interpretations of the observed signal, from scenarios like cosmic inflation, scalar-induced GWs, first-order phase transitions (PTs), cosmic strings, and domain walls. All these models, except for stable cosmic strings from field theory, can reproduce the signal as observed in PTA data. Comparisons with the standard model of SMBHBs show cosmological models often yield better fits, with high BFs. However, these results are contingent on assumptions about the SMBHB population and should not be seen as definitive evidence of new physics. As a result, constraints on parameter regions where the predicted GW signal from cosmological sources exceeds the PTA signal can be derived, independent of the signal's origin, demonstrating how pulsar timing data constrain these models. Finally, searches for deterministic signals from UL$\mathcal{DM}$ and $\mathcal{DM}$ substructures in the Milky Way can be also be performed, leading to updated constraints on these models. For UL$\mathcal{DM}$, these constraints surpass those from torsion balances and atomic clocks for UL$\mathcal{DM}$ coupled to electrons, muons, or gluons.

11.1. Cosmic inflation

Cosmic inflation is a period of accelerated expansion in the early universe that sets up the initial conditions of standard big bang cosmology [256]. By rapidly stretching spacetime, inflation explains the size, homogeneity, isotropy, and flatness observed on cosmological scales. It also sources both scalar and tensor quantum vacuum fluctuations of the inflaton and metric. The scalar modes provide the seeds for structure formation, reentering the horizon after inflation as classical density perturbations. Meanwhile, the tensor modes generate a stochastic GWB once they similarly reenter the horizon during the radiation or matter eras [4, 145, 170, 171, 344, 375, 376].

These inflationary GWs (IGWs) imprint themselves on the temperature and polarization anisotropies of the cosmic microwave background (CMB) [16, 231, 346, 374]. Their amplitude is quantified by the tensor-to-scalar ratio, r, which is constrained by current CMB data: for instance, $r < 0.036$ [7], $r < 0.032$ when the standard single-field slow-roll consistency relation ($r = -8n_{\rm T}$) is assumed [397], and $r < 0.076$ with $-0.55 < n_{\rm T} < 2.54$ when that relation is relaxed [328]. In the simplest slow-roll scenario, $n_{\rm T} = -r/8 < 0$, so the resulting GW spectrum is slightly red-tilted and falls below the reach of most present and upcoming GW experiments, including PTAs, Laser Interferometer Space Antenna (LISA), and ground-based detectors [83]. Indeed, a nearly flat or red-tilted tensor spectrum generally implies an unobservably small amplitude at PTA frequencies.

Nonetheless, both CMB and big bang nucleosynthesis (BBN) constraints on the total radiation density permit nonminimal inflationary scenarios that can yield a blue-tilted spectrum at smaller scales [245]. Such enhancements can arise if there is a stiff component in the post-inflationary universe ($w > 1/3$) [66, 162] or via processes during inflation, including particle production [20, 41, 43, 367], the presence of spectator fields or space-dependent inflation [42, 56, 57, 158], modifications of gravity [198, 368], or enhanced scalar perturbations at small scales and/or primordial black holes (PBHs). In these scenarios, the resulting GWB could reach the sensitivity of PTAs, LISA, or ground-based detectors, despite remaining compatible with CMB measurements. Such a possibility has motivated the IGW interpretation of recent PTA data sets [52, 239, 401], illustrating that deviations from standard single-field slow-roll inflation may significantly improve prospects for detecting primordial gravitational waves at accessible frequencies.

11.2. Cosmological phase transitions

A first-order phase transition in cosmology occurs when a potential barrier separates the true and false vacua of a scalar field. This phase transition proceeds via bubble nucleation, where bubbles of the true vacuum appear within the false vacuum [132]. As these bubbles expand and collide, and as sound waves propagate through the plasma, a primordial GWB is produced [81, 196, 201, 217, 232, 233, 420].

Several parameters determine the amplitude and shape of this GW signal:

- T_*: The percolation temperature, defined by the point at which roughly 34% of the universe is in the true vacuum [132].
- α_*: The transition strength, i.e. the ratio of released vacuum energy to the radiation energy density at percolation [84, 132].
- H_*R_*: The average bubble separation (in Hubble-radius units) at percolation, related to the nucleation rate β by $H_*R_* = (8\pi)^{1/3} v_{\rm w} H_*/\beta$, where $v_{\rm w}$ is the bubble wall velocity.

Bubble collisions and sound waves both contribute to the GW energy density:

$$\Omega^{\rm b}_{\rm GW}(f) = \tilde{\Omega}_{\rm b} \left(\frac{H_*R_*}{1+H_*R_*}\right)^2 \left(\frac{\alpha_*}{\alpha_*+1}\right)^2 \Delta\Sigma_{\rm b}\left(\frac{f}{f_{\rm b}}\right), \tag{90}$$

$$\Omega^{\rm s}_{\rm GW}(f) = \tilde{\Omega}_{\rm s} \left(\frac{H_*R_*}{1+H_*R_*}\right)^2 \kappa_s^2 \left(\frac{\alpha_*}{\alpha_*+1}\right)^2 \tau_{\rm sw}\, \Delta\Sigma_{\rm s}\left(\frac{f}{f_{\rm s}}\right), \tag{91}$$

where $\tilde{\Omega}_{\rm b}$ and $\tilde{\Omega}_{\rm s}$ are numerical prefactors, κ_s is the efficiency factor for converting vacuum energy into bulk motion [144], and $\tau_{\rm sw}$ accounts for sound-wave lifetime.

11.3. Cosmic strings

Cosmic strings are one-dimensional topological defects that may form during early-universe symmetry breaking [228]. These strings, characterised by a tension μ, generate a stochastic GWB through oscillating loops produced when string segments intercommute [114, 197, 400, 411]. The GW energy density from a network of cosmic strings is:

$$\Omega_{\rm GW}^{\rm cs}(f) = \frac{8\pi}{3}(G\mu)^2 \sum_{k=1}^{k_{\rm max}} P_k \mathcal{I}_k(f), \tag{92}$$

where G is the gravitational constant, P_k is the power in the kth harmonic (modelled as $P_k = \Gamma k^{-q}/\zeta(q)$), and $\mathcal{I}_k(f)$ accounts for loop number density and redshifting. The large energy densities of these strings moving at relativistic velocities makes them natural sources of GWs arising from bursts from cusps and, kinks and their collisions on the loops [114].

Different values of q (e.g. 4/3 or 5/3) describe whether emission arises predominantly from cusps or kinks on the loops.

Metastable strings can decay via monopole–antimonopole pair production:

$$\Gamma_{\rm d} = \frac{\mu}{2\pi} {\rm e}^{-\pi\kappa}, \tag{93}$$

where $\Gamma_{\rm d}$ is the decay rate and κ controls the string lifetime. Cosmic superstrings, predicted in certain string-theory frameworks, have a lower intercommutation probability P, and their GWB scales as $\Omega_{\rm GW}^{\rm super}(f) = \Omega_{\rm GW}^{\rm cs}(f)/P$.

11.4. Domain walls

Domain walls are two-dimensional defects formed when a discrete symmetry breaks spontaneously in the early universe [228]. As these walls evolve and eventually decay, they generate a GWB [190, 331, 412]. The GW energy density is often written as:

$$h^2\Omega_{\rm GW}(f) = \frac{3\pi^2}{32}\Delta\epsilon\,\Sigma(f/f_{\rm p}), \tag{94}$$

where $\Delta\epsilon$ (≈ 0.7) is an efficiency factor from simulations, and $\Sigma(x)$ is again a broken power-law function of frequency. The peak frequency $f_{\rm p}$ depends on the decay temperature T_*, with

$$f_{\rm p} = 1.14\,{\rm nHz}\left(\frac{g_{*,s}}{10.75}\right)^{1/3}\left(\frac{T_*}{10\,{\rm MeV}}\right). \tag{95}$$

If domain walls decay into dark radiation (DW-DR), an extra effective number of neutrino species $\Delta N_{\rm eff}$ can be generated, if they decay primarily into Standard Model particles (DW-SM), $T_* \gtrsim 2.7\,{\rm MeV}$ is required to preserve standard nucleosynthesis. In both scenarios, the domain-wall network must decay before dominating the universe's energy budget in order to remain consistent with observations.

11.5. Second order GWB from curvature perturbations

Although the scalar, vector and tensor modes of the perturbed metric do not mix at linear order [257], scalar curvature perturbations can source propagating tensorial modes (i.e. GWs) at second order [279, 396]. Primordial density fluctuations associated with scalar curvature perturbations can be shown to arise naturally in the universe and can be constrained by CMB observations. These perturbations have been constrained to have a quasi-scale invariant power

spectrum with an amplitude of $A_{\rm eta} \sim 2 \times 10^{-9}$. The GWB generated would thus be virtually undetectable at the nHz frequency range with an energy density $\Omega_{\rm gw} \sim 10^{-24}$ in the standard scenarios. However, the class of inflationary models [67, 76, 121] can boost the power at small scales and thus source a GWB detectable in the PTA band. PTA measurements of a second order GWB from curvature perturbations thus offer an excellent complementarity to the CMB measurements which probe large cosmological scales by placing strong limits on the predicted growth rate of the power spectrum from various inflation models.

11.6. Deterministic signals from new physics

Some theories of new physics could leave *deterministic* imprints in pulsar timing data, such as small-scale $\mathcal{DM}$ substructures or UL$\mathcal{DM}$. Although no compelling evidence for these signals is found in PTA datasets, upper limits on their possible strengths from both the NANOGrav 15 yr and EPTA DR2 datasets yield tighter constraints on the models.

11.7. Ultralight DM

$\mathcal{DM}$ comprises about 27% of the universe's energy density, yet its fundamental nature remains elusive. UL$\mathcal{DM}$ models postulate bosonic particles with masses as low as $m_\phi \sim 10^{-23}\,\mathrm{eV}$. Such particles can suppress small-scale structure, potentially addressing challenges in the standard ΛCDM model [72].

PTAs are sensitive to UL$\mathcal{DM}$ in the mass range

$$10^{-23}\,\mathrm{eV} \lesssim m_\phi \lesssim 10^{-20}\,\mathrm{eV}, \tag{96}$$

because the observed frequency f is related to m_ϕ via $\omega = 2\pi f \sim m_\phi$. The timing residual for the Ith pulsar can be written:

$$h_I(t) = \sum_i \left[A_i^E(x) \sin\left(\omega t + \gamma_i^E\right) + A_i^{P,I}(x) \sin\left(\omega t + \gamma_i^{P,I}\right) \right], \tag{97}$$

where:

- $\omega = 2\pi f$ is the angular frequency,
- $A_i^E(x)$ and $A_i^{P,I}(x)$ are amplitudes corresponding to the Earth and pulsar terms, respectively,
- γ_i^E and $\gamma_i^{P,I}$ are phases,
- i indexes the UL$\mathcal{DM}$ field's polarization.

A key distance scale is the correlation length,

$$\ell_{\rm c} \approx \frac{2\pi}{m_\phi v_\phi} \approx 0.4\,\mathrm{kpc}\left(10^{-22}\,\mathrm{eV}/m_\phi\right), \tag{98}$$

where $v_\phi \sim 10^{-3}$. If $\ell_{\rm c}$ greatly exceeds the pulsar–Earth separation (the 'correlated' limit), both observer and source sample the same $\mathcal{DM}$ field, simplifying the signal model.

Several UL$\mathcal{DM}$-induced effects may yield pulsar timing signatures:

(i) Metric fluctuations: Field oscillations alter the stress-energy tensor, producing metric perturbations and timing residuals [227, 330].
(ii) Doppler–U(1) forces: Ultralight vector $\mathcal{DM}$ can create dark electric fields that act on baryon number, shifting arrival times [168, 425].

(iii) Pulsar spin fluctuations: Coupling between scalar UL$\mathcal{DM}$ and Standard Model fields can modulate pulsar spin frequencies by changing fundamental constants [219].
(iv) Reference clock shifts: Similar fundamental-constant variations may shift atomic clock frequencies, introducing common signals across all pulsars [168, 219].

Constraints on scalar UL$\mathcal{DM}$ couplings $\{d_e, d_g, d_q\}$ in the Lagrangian,

$$\mathcal{L} \supset \frac{\phi}{\Lambda}\left[d_e\, e F_{\mu\nu}F^{\mu\nu} - d_g\, \frac{\beta_3}{2g_3}\, G^a_{\mu\nu} G^{a\mu\nu} - \sum_{q=u,d,s} d_q m_q \bar{q} q\right], \tag{99}$$

are derived from the absence of detectable signals in the dataset, improving upon past bounds.

11.8. $\mathcal{DM}$ substructures

Small-scale $\mathcal{DM}$ substructures, such as primordial black holes PBHs, may leave observable marks in pulsar timing data. PBHs can produce timing residuals through:

- Doppler signals: pulsar accelerations induced by PBH gravity cause long-term changes in pulsar spin frequencies. The static Doppler signal is

$$h_{\rm D}(t) = A_{\rm D,sta}\left(\frac{t}{\rm yr}\right)^2, \tag{100}$$

  where $A_{\rm D,sta}$ depends on PBH mass and distance.
- Shapiro signals: gravitational time delays from PBHs also produce characteristic timing shifts:

$$h_{\rm S}(t) = A_{\rm S,sta}\left(\frac{t}{\rm yr}\right)^2. \tag{101}$$

Monte Carlo simulations [249] were used to derive posterior distributions for the PBH mass fraction $f_{\rm PBH} = \Omega_{\rm PBH}/\Omega_{\mathcal{DM}}$ over various PBH masses M. The study also considers $\mathcal{DM}$ substructures with Yukawa interactions:

$$V_{\rm fifth}(r) = \tilde{\alpha}\,\frac{GMM_{\rm P}}{r}\,{\rm e}^{-r/\lambda}, \tag{102}$$

where $\tilde{\alpha}$ is the coupling relative to gravity, λ is the interaction range, and M, $M_{\rm P}$ are masses of the substructure and the pulsar, respectively. Such interactions increase pulsar accelerations, affecting the Doppler signal and yielding constraints on $\tilde{\alpha}$ similar to those for PBHs.

11.9. Compatibility of the NANOGrav 15 yr spectrum with early–universe or novel physics backgrounds

A Bayesian framework built on `enterprise`, `enterprise_extensions` and the PTArcade wrapper examined the NANOGrav 15 yr timing residuals to contrast a purely astrophysical interpretation with a variety of cosmological GW backgrounds [300].

Inflationary GWs. The inflationary scenario outperforms the SMBHB-only hypothesis with a BF of 8.8 ± 0.3, driven by its richer parameter space; including an SMBHB component reduces this to 7.9 ± 0.3, demonstrating only marginal gain despite the enlarged prior volume. Posterior contours satisfy

$$n_{\rm t} = 0.14 \log_{10} r + 0.58, \tag{103}$$

ensuring $\mathcal{P}_t \sim 10^{-4}$ across PTA frequencies. A bimodal structure traces modes re-entering during radiation ($T_{\rm rh} > 1\,{\rm GeV}$) versus reheating ($T_{\rm rh} = 1\,{\rm GeV}$), with effective tilts $n_{\rm t}$ and $n_{\rm t} - 2$. In the limits $T_{\rm rh} \to \infty$ or $T_{\rm rh} \to 0$, parameters settle at $(n_{\rm t}, \log_{10} r) \approx (-2, -10)$ or $(-4, -20)$, reflecting the PTA band's insensitivity. The choice $n_{\rm t} = 2$ corresponds to a spectral index $\gamma = 3$, aligning with data. Constraints from BBN and LVK bounds on $\Delta N_{\rm eff}$ and $f_{\rm end}$ carve out the allowed $(T_{\rm rh}, n_{\rm t})$ region, admitting models up to $n_{\rm t} \sim 3$–4, $r \sim 10^{-16}$, $T_{\rm rh} \sim 10^{-3}\,{\rm GeV}$ and $N_{\rm rh} \lesssim 20$.

Scalar-induced GWs. Three models which capture different ways of injecting localized structure into the primordial power spectrum– a delta spike (DELTA), a Gaussian bump (GAUSS), or a flat box-shaped enhancement (BOX) in logarithmic k-space — were used. These scalar induced templates achieve BFs of 44 ± 2 (DELTA), 57 ± 3 (GAUSS) and 21 ± 1 (BOX), all comfortably surpassing inflationary fits. The DELTA spectrum remains essentially unchanged by adding SMBHB power. Departures from simple power laws extend coverage across the PTA band, yielding lower limits on $\log_{10} A$ of roughly -1.55, -1.43, -1.90 (DELTA, GAUSS, BOX). Frequency posteriors often lie below the NANOGrav sensitivity peak, and regions excluded by PBH overproduction or a conjectured one-loop no-go theorem further restrict viable amplitudes.

Phase transitions. Broken power-law forms, $\Sigma(x) = \frac{(ax)^b}{1+(ax)^{b+c}}$, capture sound-wave (PT-SOUND) and bubble-collision (PT-BUBBLE) spectra. Posterior intervals favour a strong, slow transition: PT-BUBBLE requires $\alpha_* > 1.1$, $H_* R_* > 0.28$ (68%); PT-SOUND requires $\alpha_* > 0.42$, $H_* R_* \in [0.053, 0.27]$. The SMBHB component relaxes these slightly. Peak frequencies align with high-end bins, tails with low end. Inferred temperatures span $T_* \in [0.047, 0.41]\,{\rm GeV}$ (BUBBLE) and $[4.7, 33]\,{\rm MeV}$ (SOUND), shifting upward when SMBHB is included. Correlations follow $\alpha_* \sim 1/(H_* R_*)$ (BUBBLE) and $H_* R_* \propto \alpha_*^{12}$ (SOUND). Compared to earlier datasets, spectra are bluer, shifting T_* upward and evading BBN/CMB limits. The BFs are 18.1 ± 0.6 (BUBBLE) and 3.7 ± 0.1 (SOUND), rising to 6.5 ± 0.3 for PT-SOUND plus SMBHB.

Cosmic strings. Stable–string models are strongly disfavoured, with BFs in the 0.28–0.38 range, as high tensions flatten the spectrum. Metastable strings fit better ($13.4 \pm 0.4, 21.3 \pm 0.8$ for META-L/LS), peaking near $k \sim 8$, $\log_{10} G\mu \sim -7$. Superstring networks produce the strongest support (46 ± 2, 37 ± 2 with SMBHB), preferring $\log_{10} G\mu \sim -12$ and $P \sim 10^{-3}$, though LVK constraints may impinge.

Domain walls. Domain-wall spectra (DW-SM, DW-DR) concentrate power at low frequencies. DW-SM yields $T_* \in [110, 275]\,{\rm MeV}$, $\alpha_* \in [0.080, 0.19]$ (68%); DW-DR gives $T_* \in [79, 153]\,{\rm MeV}$, $\Delta N_{\rm eff} \gtrsim 0.32$, broadening without an upper bound under SMBHB. The BFs reach 14.8 ± 0.5 (DW-SM) and 1.62 ± 0.05 (DW-DR), rising to 21.1 ± 0.9 and 2.53 ± 0.10 with SMBHB.

Ultralight $\mathcal{DM}$ and PBHs. Across masses $10^{-24} \leqslant m_f \leqslant 10^{-20}\,{\rm eV}$, fits yield Bayes factors near unity, except a slight 4 nHz Earth-term signal ($\sim$2) at $m_f \sim 2 \times 10^{-23}\,{\rm eV}$, conflicting with Ly α and kinematic limits. Upper bounds on local UL$\mathcal{DM}$ density exclude dominance below $10^{-23}\,{\rm eV}$, flattening toward $10^{-26}\,{\rm eV}$. Coupling constraints to electrons, muons, gravity and gauge fields align with lab and PPTA bounds under a Rayleigh prior. No PBH background is found; static Doppler and Shapiro effects set 95% upper limits on $f_{\rm PBH}$, while dynamic

Doppler remains undetectable. Fifth-force limits on $\tilde{a}$ rival equivalence-principle and NS heating bounds for $M \gtrsim 10^{-12} M_\odot$, though Bullet Cluster and MICROSCOPE constraints dominate under full $\mathcal{DM}$ coupling.

11.10. Compatibility of the EPTA DR2 spectrum with early–universe or novel physics backgrounds

A Bayesian framework, analogous to that used for NANOGrav, contrasts an SMBHB interpretation with a suite of cosmological GWBs in EPTA DR2.

Inflationary GWs. IGW-only is slightly disfavoured relative to SMBHB, with a Bayes factor $\mathcal{B} = 0.8 \pm 0.2$. Adding IGW to SMBHB yields $\mathcal{B} \simeq 1$, i.e. negligible improvement. Posteriors are broad and show no distinctive inflationary signatures.

Scalar–induced GWs. SIGW fits are weak: DELTA gives $\mathcal{B} = 1.2 \pm 0.3$, GAUSS $\mathcal{B} = 1.5 \pm 0.4$. The amplitude is bounded by $\log_{10} A \lesssim -1.3$ (95%), and the narrow frequency localisation demanded by PTA sensitivity further squeezes the viable space.

Phase transitions. Broken power-law templates modestly outperform SMBHB only. PT-BUBBLE achieves $\mathcal{B} = 2.3 \pm 0.5$; PT-SOUND $\mathcal{B} = 1.8 \pm 0.4$. Posteriors favour strong transitions with T_* of $\mathcal{O}(10\text{–}10^2)$ MeV and $\alpha_* \sim 0.1$. Tension with BBN/CMB bounds persists but is model-dependent.

Cosmic strings. Stable strings are strongly disfavoured, $\mathcal{B} = 0.10 \pm 0.02$, with $G\mu < 10^{-10.7}$ (95%). Metastable strings fit better, $\mathcal{B} = 3.5 \pm 0.7$, favouring $10^{-12} \lesssim G\mu \lesssim 10^{-7}$ and high decay rates ($\sqrt{\kappa} \gtrsim 8$). Cosmic superstrings are preferred among string models, $\mathcal{B} = 5.8 \pm 1.0$, with $P \sim 10^{-3}$ and $G\mu \sim 10^{-11}$–10^{-10}; some of this space is under LVK pressure.

Domain walls. DW-SM gives $\mathcal{B} \approx 1.1$; DW-DR $\mathcal{B} \approx 0.9$. Posteriors suggest $T_* \sim 100$–300 MeV and $\alpha_* \sim 0.05$–0.2. Adding SMBHB power does not materially change the picture.

Ultralight $\mathcal{DM}$ and PBHs. UL$\mathcal{DM}$ is disfavoured, with BFs $\sim$0.5 across the scanned mass range; the implied density cannot dominate $\mathcal{DM}$ under EPTA DR2 assumptions. No separate PBH background is detected.

Challenging the UL$\mathcal{DM}$ paradigm. Using EPTA-DR2Full (24.7 yr, daily–biweekly cadence) with per-backend white-noise modelling and a CURN process, a deterministic UL$\mathcal{DM}$ sinusoid at $f = m_\phi/2\pi$ is searched in three coherence regimes. Bayesian inference (`enterprise`+`enterprise_extensions`) finds $\ln B_{\max} < 1$ for $m_\phi \in [10^{-24}, 10^{-22}]$ eV; 95% limits on the local density are $\rho_\phi \lesssim 0.15\,\mathrm{GeV\,cm^{-3}}$ for 10^{-24}–$10^{-23.7}$ eV and $\rho_\phi \lesssim 0.30\,\mathrm{GeV\,cm^{-3}}$ for $10^{-23.7}$–$10^{-23.4}$ eV. A small feature at $m_\phi \simeq 10^{-23}$ eV ($\ln B \sim 0.1$) is noise-consistent and astrophysically excluded. Thus, in 10^{-24}–$10^{-23.3}$ eV, UL$\mathcal{DM}$ is at most a subdominant fraction of local $\mathcal{DM}$.

Constraints on conformal ULDM couplings. Allowing universal conformal couplings $A(\phi)$, EPTA DR2 constrains FJBD (linear) and DEF (quadratic) cases via ULDM-driven spin-frequency modulation. For $m_\phi \lesssim 10^{-21}$ eV, $\log_{10}\alpha \lesssim -4.5$ globally (tightening to $\lesssim -7$ near 10^{-23} eV), exceeding solar-system and triple-pulsar bounds. Assuming $\rho_\phi = \rho_{\rm DM}$, DEF yields $-2 \lesssim \beta \lesssim 20$ (95%); these weaken roughly linearly if UL$\mathcal{DM}$ is only a fraction of $\mathcal{DM}$. No viable strong equivalence–violating couplings survive in this mass range.

11.11. Beyond the standard model using the PTA results

The PTA results have generated a very wide range of discussions beyond those presented in the papers from the PTAs themselves. Given the broad constraints on the spectrum, and the surprisingly high amplitude recovered for the powerlaw model, the number of models that can provide plausible fits remains quite large. As such it is virtually impossible to cover all of the models and their nuances. However, I summarise below a small, representative sample of papers discussing a variety of models, a significant number of which focus on the beyond standard model (BSM) physics. A full review of those would extend beyond the scope of this review, but the connections of the PTA results with single/multifield inflation with large fluctuations, PBHs, and loop corrections have been explored in [99], while their ability to probe cosmic history, revealing BSM signals have been discussed in [343] and references therein. Expanding-spacetime corrections to fluid shell collisions which alter the spectral shape of first order PTs (FOPTs) and make them detectable in the PTA bands can be found in [213]. Junior Iovino [216] reviews PBH formation scenarios and second-order GW constraints from LIGO and PTA synergy while [343] demonstrates how GWs traverse cosmic epochs transparently, opening a direct window on dark-sector physics, although loop corrections heavily restrict single-field PBH models unless they are finely tuned [99]. Similarly, summaries of alternative theories of gravity can be gleaned from [124], where a Chern–Simons-inspired running vacuum model features a metastable inflationary phase with quantum condensate corrections. Beyond model templates, current PTAs also constrain sky distribution and polarizations of the GWB: (1) a 95% limit on broadband anisotropy, $(C_{\ell>0}/C_{\ell=0}) < 0.2$; (2) no preference for non-tensor correlations—HD vs. scalar-transverse gives Bayes factor $\sim$2 and the HD component accounts for essentially all power; (3) no evidence for spectral running, with $\beta \in [-0.80, 2.96]$ and $B_{\rm RPL/CPL} = 0.69 \pm 0.01$.

(i) Cosmic strings and topological defects: cosmic strings are one-dimensional topological defects that can form during early-universe symmetry breaking and generate a stochastic GWB through loop dynamics, cusps/kinks, and related processes. Variants include metastable strings, superconducting strings, cosmic superstrings (with reduced intercommutation probability), and hybrid defects such as domain walls bounded by strings.
   (a) Metastable cosmic strings and stochastic gravitational Waves: Certain inflationary models predict metastable strings from a two-step symmetry-breaking process. Although these strings eventually decay, they can still contribute a detectable stochastic GWB. Representative benchmarks used in the literature include a tension $G_N\mu \sim 10^{-5}$ with a stochastic GWB peaking near $f \sim 10^{-9}$ Hz and amplitude $\Omega_{\rm GW} \sim 10^{-10}$ [40, 98].
   (b) Monopole production from metastable cosmic strings: Quantum decay of metastable strings can produce topologically stable monopoles (carrying Dirac and colour magnetic charges), with masses $M_{\rm mono} \sim 10^8$–10^{17} GeV depending on $G\mu$ [246]. The associated GW signal from monopole-connected string decay peaks at $f \sim 10^{-8}$–10^{-6} Hz, a target for ET/CE [246].
   (c) Superconducting cosmic strings and their unique GW signatures: In BSM settings, string currents/charges yield superconducting networks with modified scaling across radiation/matter eras, imprinting a distinct coherence length and condensate equation of state in the stochastic GWB [108]. Simulations indicate detectable deviations from standard string spectra, with a characteristic amplitude $\Omega_{\rm GW} \sim 10^{-9}$ in the 10^{-6}–10^{-3} Hz window (LISA band) [108].
   (d) Decay into $\mathcal{DM}$ and gauge bosons: In some models, strings predominantly radiate into gauge bosons that subsequently populate $\mathcal{DM}$/radiation sectors. The resulting

GW spectrum shows a high-frequency power law with $\Omega_{\rm GW}\sim 10^{-12}$ at $f\sim 10^{-2}$ Hz, offering discrimination prospects with LISA/ET/BBO [97].

(e) Domain walls bounded by cosmic strings: Certain symmetry-breaking patterns produce hybrid networks where domain walls terminate on strings. Their GW spectrum exhibits a characteristic inflection between μHz and Hz, with predicted peak amplitudes around $\Omega_{\rm GW}\sim 10^{-11}$ for breaking scales 10^{12}–10^{15} GeV in $U(1)_R$ extensions [157].

(f) Axion strings and CMB constraints: Axion(-like) string networks can survive to sub-BBN temperatures, sourcing both GWs and CMB polarization rotation. Current CMB power-spectrum bounds suggest $f_{\rm a}\lesssim 10^{12}$ GeV remains testable in future surveys; the GW spectrum from axion strings typically peaks near $f\sim 10^{-10}$ Hz with $\Omega_{\rm GW}\sim 10^{-12}$, within reach of next-generation PTAs [51].

(ii) Inflationary models and PBHs inflationary models provide a framework to explain the observed large-scale structure of the universe and generate the primordial fluctuations that seed cosmic structure. Under certain conditions, these fluctuations can lead to the formation of PBHs, which in turn serve as a significant source of GWs. The GWB from these processes provides crucial observational tests for inflationary physics and PBH formation scenarios.

(a) Inflationary Perturbations and PBH Formation: Inflation generates quantum fluctuations that become classical perturbations as they exit the Hubble horizon. If these perturbations are sufficiently large upon reentry, they can collapse into PBHs. The critical density contrast for collapse is typically given by $\delta_{\rm c}\sim 0.45$ [see e.g.; 427, and references therein]. PBH formation is particularly enhanced in models featuring an ultra-slow-roll phase, where the inflaton potential flattens temporarily, leading to an amplification of scalar perturbations. The characteristic PBH mass in these scenarios ranges from $10^{-15}M_\odot$ to $10^{-2}M_\odot$, with a corresponding GW spectrum peaking at frequencies of 10^{-6}—10^{-2} Hz [203]. Fitting the nHz background with SIGWs typically requires a narrow bump with $\mathcal{P}_\zeta(k_*)\simeq(1\text{–}4)\times 10^{-2}$ at $k_*\sim 10^{6.5\pm 0.5}\,{\rm Mpc}^{-1}$ (i.e. $f_*\sim 3$–30 nHz), mapping to $M_{\rm PBH}\sim 10^{-12}$–$10^{-11}\,M_\odot$ if PBHs accompany the peak [417].

(b) Axion-Gauge field interactions and inflationary GWs: In axion inflation models, gauge field interactions with the inflaton can lead to significant enhancement of GWs. These interactions produce chiral GWs, leading to potential parity-violating signatures that could be tested by future space-based detectors [41]. The predicted energy density of these waves is $\Omega_{\rm GW}\sim 10^{-10}$ at frequencies around 10 mHz, making them accessible to experiments like LISA [204].

(c) Multi-Step Inflation and PBH Production: Multi-step inflationary scenarios introduce sharp transitions in the inflaton potential, leading to localized enhancements in the scalar power spectrum. These transitions can arise from interactions with additional fields or changes in the effective mass of the inflaton [92]. Recent studies suggest that such transitions can produce a bimodal PBH mass distribution, with peaks at $\sim 10^{-14}M_\odot$ and $\sim 10^{-4}M_\odot$, leading to multiple sources of gravitational wave production [430]. The stochastic GW spectrum from these PBHs features peaks in the nHz and mHz frequency bands, making them prime candidates for detection by PTAs and LISA [39, 87].

(d) Scalar-Induced GWs from PBH Formation: When PBHs form due to large inflationary perturbations, they also generate secondary GWs through nonlinear couplings between the enhanced curvature perturbations. These induced GWs can be detected independently of the PBHs themselves and serve as a direct probe of the primordial power spectrum. The frequency of these scalar-induced GWs is given by $f_{\rm GW}\sim$

$10^{-9}\left(\frac{M}{10^{-12}M_\odot}\right)^{-1/2}$ Hz, where M is the mass of the forming PBH. Observations of the stochastic GWB in the nHz band suggest that if PBHs make up all of DM, their mass must be within 10^{-12}–$10^{-11}M_\odot$ [15]. *To be consistent with the current PTA limits SIGWs need $\mathcal{P}_\zeta$ at the few$\times 10^{-2}$ level near the nHz peak; broader bumps overproduce PBHs unless non-Gaussianity or extended spectra are invoked [155, 416].*

(e) Observational constraints on inflationary GWs: The latest data from CMB experiments such as Planck and BICEP/Keck provide strong constraints on the inflationary tensor-to-scalar ratio, with an upper bound of $r < 0.036$ at 95% confidence [7]. Future observations with LiteBIRD aim to improve this sensitivity by an order of magnitude, potentially confirming or ruling out a broad class of inflationary models [160]. Additionally, LISA and DECIGO are expected to probe IGWs with amplitudes down to $\Omega_{\rm GW} \sim 10^{-12}$, allowing for direct tests of ultra-slow-roll inflation and axion-gauge field interactions [43]. *Fits to the angular correlation of pulsars pairs as available from the latest PTA datasets imply $v_{\rm gw}/c > 0.87$ (95%) and $m_{\rm g} \lesssim (0.8\text{–}1.5)\times 10^{-23}$ eV, depending on spectral priors [55, 417, 421].*

(f) Primordial black holes as $\mathcal{DM}$ candidates: The possibility that PBHs constitute a fraction of $\mathcal{DM}$ is a subject of ongoing debate. Microlensing constraints from OGLE and HSC exclude PBHs in the mass range 10^{-11}—10^{-6} $M_\odot$ from making up all of $\mathcal{DM}$ [306]. However, recent work suggests that a small fraction ($\sim 10^{-3}$) of $\mathcal{DM}$ in the form of PBHs remains consistent with all existing constraints [86]. Observations of PBH mergers by LIGO-Virgo provide additional constraints. If PBHs dominate the binary black hole population, the merger rate at redshift $z \sim 1$ should be at least $\sim$10 Gpc^{-3} yr^{-1}, which is consistent with current estimates [59]. *In the 10^{-12}–$10^{-11}, M_\odot$ mass window, the PTA-required nHz SIGW amplitude places strong limits on PBH $\mathcal{DM}$: a fraction $f_{\rm PBH} = 1$ is disfavoured unless the underlying curvature perturbation bump is extremely narrow or highly non-Gaussian [416].*

(g) Chain inflation and first-order phase transitions: Chain inflation differs from slow-roll inflation, as the inflaton tunnels through a series of consecutive vacuum states. This process results in multiple first-order phase transitions, each contributing to the stochastic GWB. The predicted GW spectrum exhibits a double-peak structure, with a faint high-frequency component from inflationary quantum fluctuations and a stronger low-frequency component marking the transition to radiation dominance [156]. Some studies suggest chain inflation could explain the recently detected stochastic GWB by NANOGrav, PPTA, EPTA, and CPTA [156]. *PTA fits to the nHz background imply that for causal FOPTs with $f_{\rm p} \sim$few–30 nHz, the corresponding transition temperature is $T_* \sim$30–300 MeV; most PTA-compatible models favour slow completion [8, 84].*

(h) Hybrid inflation and preheating-induced gravitational waves: In hybrid inflation, inflation ends when a secondary scalar field, the 'waterfall' field, becomes tachyonic, triggering rapid particle production (preheating). This tachyonic preheating phase sources GWs, which may be observable in upcoming experiments [70]. Variations of hybrid inflation can also lead to topological defects, such as unstable domain walls, that generate a stochastic GWB [70].

(i) High-frequency primordial GWs from post-inflation dynamics: Some inflationary models predict high-frequency primordial GWs (PGWs) due to the instantaneous transition from inflation to radiation dominance. If a stiff post-inflationary phase exists, PGWs display a characteristic spectral shape of power-law increase followed by exponential decay [326]. A new semi-analytical expression suggests that PGWs at high wave numbers could be used for signal searches [326].

(j) Curvaton models and non-gaussianity in PBH formation: In curvaton models, an additional scalar field dominates the universe after inflation and generates perturbations that lead to PBH formation. These models predict non-Gaussian primordial fluctuations, significantly affecting the PBH mass function and induced GWs [325]. If the curvaton-generated perturbations are highly non-Gaussian, PBHs can form without requiring large inflaton fluctuations [325]. *PTA constraints on the nHz SIGWB require* $\mathcal{P}_\zeta \sim few \times 10^{-2}$ *near* $k \sim 10^{6-7}\,\mathrm{Mpc}^{-1}$*; curvaton non-Gaussianity alters the PBH connection but not the PTA-required SIGW peak amplitude [416].*

(k) Delayed vacuum decay and PBH formation: PBHs can form through delayed vacuum decay during slow cosmic first-order phase transitions. The PBH abundance is highly sensitive to the barrier height of the scalar potential. Studies suggest that this mechanism does not require extreme supercooling and can produce PBHs with a mass spectrum spanning multiple orders of magnitude [218]. The transition duration is a key factor, and standard nucleation approximations fail to capture the PBH formation dynamics [218].

(l) Spectator fields and stochastic PBH formation: Some models propose that large curvature fluctuations leading to PBH formation arise from stochastic fluctuations of a light spectator field during inflation. These scenarios predict an extended PBH mass distribution with peaks at the solar-mass scale and provide an alternative explanation for the stochastic GWB observed by PTAs [372].

(m) Dark sector interactions and PBH production: Certain models explore how PBH formation is influenced by hidden-sector physics, such as asymmetric reheating or dark radiation. Extended dark-sector models predict unique GW signatures that could be tested using current and future observatories [63].

(iii) First-order phase transitions first-order phase transitions in the early universe produce strong GWs through bubble nucleation, sound waves, and turbulence in the primordial plasma. These transitions occur when a metastable vacuum decays into a lower-energy state, releasing latent heat that generates characteristic GW signals. The GWB from these transitions provides a powerful probe of physics beyond the Standard Model and constraints on early universe dynamics.

(a) Electroweak phase transitions: Electroweak phase transitions occur when the Higgs field acquires a vacuum expectation value, breaking electroweak symmetry. If the transition is strongly first-order, it generates gravitational waves detectable by space-based interferometers. The peak frequency of these waves is expected to be in the mHz range, making them ideal targets for LISA [109]. The strength of the transition depends on the details of the Higgs potential. Extensions of the Standard Model with extra scalar fields, such as singlet Higgs models, increase the strength of the transition and enhance GW signals. The predicted GW energy density fraction in these models is $\Omega_{\mathrm{GW}} \sim 10^{-10}$ [2]. Lattice simulations suggest that bubble wall velocities range from 0.1c to 0.9c, significantly affecting the GW spectrum [189]. More efficient bubble collisions produce stronger GW signals with $\Omega_{\mathrm{GW}} \sim 10^{-9}$ [85]. The duration of the phase transition is another crucial parameter, governed by the nucleation rate $\Gamma \sim \mathrm{e}^{-S(T)}$, where S(T) is the Euclidean action [259]. Recent studies constrain the reheating temperature associated with electroweak bubbles to the range of 100–300 GeV [172].

(b) Supercooled phase transitions: Supercooling extends the duration of the phase transition, leading to stronger GW signals. These transitions occur when the universe remains trapped in a metastable phase longer than expected, delaying bubble nucleation. The degree of supercooling is characterised by the nucleation temperature T_n, estimated in recent studies to range from 10 GeV to 100 TeV [314]. The

amplitude of GWs from supercooled transitions is significantly higher than from standard electroweak transitions, with $\Omega_{\rm GW}$ reaching values of 10^{-8} [133]. The peak frequency of these waves falls between 0.01–1 Hz, making them detectable by DECIGO and BBO [161]. Recent studies show that prolonged supercooling affects entropy release and baryogenesis mechanisms, altering the phase transition's role in generating the matter-antimatter asymmetry [84]. *PTA fits to the nHz background favour peak frequencies* $f_{\rm p}\sim 3$–$30\,{\rm nHz}$*, corresponding to* $T_*\sim 30$–$300\,{\rm MeV}$ *via* $f_{\rm p}\simeq 1.1\,{\rm nHz}(g_*/10.75)^{1/6}(T_*/10\,{\rm MeV})$*, with slow/strong transitions* ($H_*R_*\sim 0.05$–*0.3,* $\alpha_*\gtrsim 0.3$*) preferred [8, 84].*

(c) Chiral phase transitions in quantum chromodynamics (QCD): Chiral symmetry breaking in QCD can also generate GWs. These transitions occur at temperatures around 150 MeV and play a crucial role in early-universe evolution. The peak GW frequency from QCD transitions is estimated to be 10^{-7} Hz, making them a potential source for PTA-detectable stochastic GWB [429]. Lattice QCD simulations indicate that the equation of state during the QCD phase transition strongly influences the GW spectrum. The energy density fraction of GWs produced in these transitions is estimated at $\Omega_{\rm GW}\sim 10^{-12}$ [420]. Observations of net baryon number fluctuations suggest that first-order QCD phase transitions can enhance the GW amplitude by up to two orders of magnitude [80]. More recent work suggests that the peak frequency of QCD-generated GWs could range from 10^{-9} Hz to 10^{-6} Hz, depending on the speed of sound in the hadronic phase [281]. Experimental constraints from heavy-ion collisions at RHIC and LHC provide further insight into QCD phase transition dynamics. A first-order QCD transition may also lead to detectable GWs from early-universe turbulence [82, 206]. *PTA-compatible broken–power-law fits to the nHz background point to* $T_*\sim 0.05$–$0.4\,{\rm GeV}$ *with slow completion* ($H_*R_*\gtrsim 0.05$*), while remaining consistent with BBN and CMB bounds [8].*

(d) GW Signatures of first-order phase transitions: The detectability of GWs from first-order phase transitions depends on the peak frequency and amplitude of the signal. Current and future GW detectors provide complementary coverage across different frequency bands—at nHz frequencies, PTAs can probe QCD phase transitions and certain supercooled scenarios [109], while at the mHz band, LISA is sensitive to electroweak phase transitions [85]. DECIGO/BBO covers the Hz range, making them optimal for detecting highly supercooled transitions with $\Omega_{\rm GW}\sim 10^{-9}$ [115]. LIGO-Virgo-KAGRA detects GWs in the kHz range but is less sensitive to cosmological phase transitions [324]. *In the nHz band, constraints for first-order transitions come through the broken–power-law peak and amplitude; viable QCD/supercooled scenarios require* $f_{\rm p}$ *in the few–*30 nHz *range with model-dependent mapping to* T_* *and duration [85, 109].*

(e) Implications for beyond standard model physics: GWs from first-order phase transitions provide a unique probe of physics beyond the Standard Model. Many theories, including supersymmetry, extra dimensions, and dark sector interactions, predict phase transitions in the early universe that could generate detectable GW signals [428]. Recent studies suggest that phase transitions associated with DM interactions could leave a distinct imprint on the GW spectrum, with potential correlations to direct detection experiments [73]. The interplay between GWs and particle physics experiments provides an exciting avenue for future research.

(f) Non-standard first-order phase transitions: In some scenarios, the energy from the phase transition is not converted into thermal plasma but instead into dark radiation, affecting the dark radiation energy density parameter $\Delta N_{\rm eff}$ [71]. Certain non-thermal

first-order phase transitions begin during inflation but complete only after reheating, leaving a distinct imprint in the CMB power spectrum. Constraints on $\Delta N_{\rm eff}$ derived from CMB+BAO data suggest a limit of $\Delta N_{\rm eff} \lesssim 10^{-5}(T_*/T_{\rm rh})^{-4}$, which is stronger than the standard adiabatic assumption [71].

(g) Leptogenesis and baryogenesis from phase transitions: The breaking of B−LB-L symmetry at the GUT scale during a first-order phase transition can generate a stochastic GWB that aligns with PTA observations [130]. Additionally, CP-violating interactions in the Standard Model can lead to baryogenesis through a meson-mediated decay scenario, producing a GW signature detectable by PTAs [137].

(h) Turbulence and magnetic fields in first-order phase transitions: Beyond bubble collisions and sound waves, turbulence in the plasma can significantly contribute to GW production. Late-stage turbulence dominates the GW spectrum, altering the spectral slope and duration of the signal [213]. Magnetic fields generated during the phase transition influence turbulence dynamics, leading to distinct spectral modifications. The magnetohydrodynamic (MHD) turbulence signatures of first-order phase transitions may be detected in upcoming experiments [213].

(i) Strongly coupled first-order phase transitions: In strongly coupled scenarios, traditional field-theoretic approaches face challenges, necessitating the use of holographic dual theories. Recent simulations have revealed universal scaling relations between the phase pressure difference and bubble wall velocity, allowing for precise analytical predictions [413]. These holographic approaches suggest that the wall pressure difference scales quadratically with the terminal wall velocity, regardless of the bubble geometry [413].

(j) GW spectrum beyond standard model phase transitions: Beyond-Standard-Model phase transitions, such as those involving radiative symmetry breaking in a dark sector, produce unique GW signatures. Some models predict a fast reheating phase facilitated by non-minimal gravity couplings, resulting in a distinct signal detected by PTAs [347]. Symmetry breaking events can also generate domain walls, which decay through quantum gravity-suppressed operators, emitting GWs detectable in future interferometers [347].

(iv) Alternative gravity theories alternative theories of gravity extend beyond GR and often introduce modifications to gravitational wave properties, including altered dispersion relations, additional polarization states, or modified propagation speeds. These theories aim to explain outstanding cosmological problems such as dark energy, cosmic acceleration, and quantum gravity effects. GW observations provide a powerful means to test these theories and constrain deviations from GR.

(a) Parity-violating gravity and GW birefringence: Parity-violating modifications to GR introduce asymmetries in the propagation of left- and right-handed GW polarizations. These modifications are common in models incorporating Chern–Simons gravity or certain effective field theories. GW birefringence arises as a natural consequence of such parity violation, where the two polarization modes travel at different speeds, leading to measurable phase shifts [78]. Recent observational constraints from LIGO-Virgo-KAGRA suggest that GW birefringence is limited to deviations at the 10^{-2} level [64]. If confirmed, this effect would provide one of the first observational signatures of parity-violating interactions in gravity. Theoretical predictions suggest that birefringence effects should be more pronounced at high frequencies ($f > 10\,\mathrm{Hz}$), making next-generation detectors such as Cosmic Explorer and Einstein telescope (ET) ideal for testing these theories.

(b) Scalar-tensor theories and modified GW polarizations: Scalar-tensor theories introduce an additional scalar degree of freedom in gravity, modifying the propagation of tensor perturbations. These modifications result in additional polarization modes beyond the standard plus and cross polarizations of GR. The energy density fraction of GWs in scalar-tensor models can be amplified to values $\Omega_{\rm GW} \sim 10^{-9}$ [85]. Some models predict that scalar-induced secondary GWs should peak in the frequency range of 0.01 Hz to 1 Hz, making them detectable by space-based interferometers such as LISA and Taiji. However, constraints from PTAs suggest that certain scalar-tensor models are viable explanations for the nHz GWB observed by NANOGrav and other collaborations [116]. *PTA polarization searches show that HD-like tensor correlations fit best; scalar-transverse modes add little support (BFs ∼1–2), implying any non-tensor contribution is subdominant [10].*

(c) Chern–Simons gravity and chiral GWs: Chern–Simons modified gravity introduces parity-violating corrections to the Einstein–Hilbert action, leading to chiral GWs where one polarization is preferentially amplified over the other. The degree of chiral asymmetry is parametrized by the Chern–Simons coupling constant $\xi_{\rm CS}$, which has been constrained observationally to $\xi_{\rm CS} < 10^{-3}$ [260]. Recent Bayesian analyses using LIGO-Virgo data have placed upper limits on Chern–Simons modifications at the 10^{-8} level, indicating that significant deviations from GR are unlikely in the currently observable frequency range [298]. Future GW detectors will further tighten these constraints, allowing for sub-percent level tests of parity violation in gravity.

(d) Einstein–Gauss–Bonnet (EGB) Gravity and GWs: Einstein–Gauss–Bonnet gravity introduces higher-order curvature corrections to the Einstein–Hilbert action. These corrections arise naturally in low-energy limits of string theory and modify the GW spectrum at cosmological scales [308]. Recent work suggests that EGB gravity can produce a blue-tilted IGW spectrum when the Gauss–Bonnet coupling function satisfies $\xi''(\phi_*)V(\phi_*) > 0$ at first horizon crossing [308]. The characteristic spectral tilt of tensor modes in these models provides a potential observational signature for distinguishing EGB gravity from standard inflationary models. Additionally, EGB gravity can amplify primordial tensor perturbations, leading to enhanced gravitational wave signals at mHz frequencies, making them detectable by LISA [30].

(e) Horndeski gravity and secondary GWs: Horndeski gravity represents the most general scalar-tensor theory with second-order field equations, providing a broad framework for modified gravity models. In the context of GWs, Horndeski gravity predicts enhancements in secondary (induced) GWs due to nontrivial scalar field interactions [122]. A key prediction of Horndeski gravity is that higher derivative interactions can dominate the source term for induced GWs, leading to stronger resonances and enhanced amplitude growth on subhorizon scales. The maximum amplitude of these waves is found to scale as $\Omega_{\rm GW} \propto \mathcal{P}_\zeta$, differing from the standard quadratic dependence in GR. Recent studies indicate that Horndeski-induced GWs could be observable even without enhancement of the primordial curvature spectrum, opening new detection possibilities for upcoming GW experiments.

(f) Massive gravity and frequency-dependent dispersion relations: Massive gravity theories propose that the graviton has a small but nonzero mass, leading to modifications in GW dispersion relations. The presence of a graviton mass introduces a frequency-dependent group velocity, altering the arrival times of GWs at different frequencies. Current bounds on the graviton mass from LIGO-Virgo observations suggest $m_{\rm g} < 1.2 \times 10^{-23}$ eV [3]. These constraints are expected to improve significantly with future observations of inspiraling binary black holes at cosmological distances. The energy

density of GWs in massive gravity models is modified due to altered damping rates in the cosmic expansion. Recent work suggests that $\Omega_{\rm GW}$ could be suppressed or enhanced by an order of magnitude compared to standard GR predictions, depending on the interaction strength of the massive graviton [259]. *PTA angular-correlation fits constrain massive-gravity models, giving* $v_{\rm gw}/c > 0.87$ *(95%) and* $m_{\rm g} \lesssim (0.8\text{–}1.5) \times 10^{-23}\,{\rm eV}$ *across reasonable priors [55, 415, 421].*

(g) Testing Alternative Gravity Theories with Future Observatories: GW observations provide a unique testing ground for alternative gravity models, with current and future detectors offering complementary sensitivities:
   1. LIGO-Virgo-KAGRA: Strong constraints on deviations from GR at frequencies above 10 Hz [121].
   2. LISA: Optimal for detecting parity-violating effects and scalar-tensor modifications at mHz frequencies [15].
   3. PTAs: NHz observations of the stochastic GWB can test massive gravity and scalar-tensor effects.
   4. Cosmic explorer and Einstein telescope: Future detectors capable of probing high-frequency deviations in birefringence and dispersion relations [428].

(h) Implications for fundamental physics: Alternative gravity theories provide a pathway to understanding unresolved problems in cosmology, such as the nature of dark energy and quantum gravity effects. Observational tests of these theories have the potential to distinguish between different high-energy extensions of GR and probe fundamental physics at unprecedented scales [19, 309]. Certain deviations from GR, such as modified dispersion relations and additional polarization states, could serve as indirect probes of string theory-inspired models of quantum gravity [24]. The synergy between GW astronomy and particle physics experiments will be crucial in the next decade for advancing our understanding of fundamental interactions.

12. Is the nHz GWB anisotropic?

Anisotropy in the GWB would indicate that the signal is dominated by a small number of bright sources or by spatial clustering of the underlying population, rather than by a fully diffuse ensemble. PTA analyses have traditionally assumed isotropy, but decomposiing the measured GWB sky onto a spherical-harmonic basis allows this assumption to be relaxed. Current datasets are beginning to probe the level of anisotropy expected from SMBHB populations, though evidence remains inconclusive. Below we summarise recent results from NANOGrav and the MPTA.

12.1. The spherical-harmonic basis

An anisotropic GWB can be described through an angular power distribution $P(\hat{\Omega})$, where $\hat{\Omega}$ denotes sky position. This distribution is expanded in real spherical harmonics $Y_{\ell m}(\hat{\Omega})$ as

$$P\left(\hat{\Omega}\right) = \sum_{\ell=0}^{\ell_{\rm max}} \sum_{m=-\ell}^{\ell} c_{\ell m}\, Y_{\ell m}\left(\hat{\Omega}\right), \tag{104}$$

with coefficients $c_{\ell m}$ to be inferred from PTA data [387]. The $\ell = 0$ monopole corresponds to an isotropic background, while higher multipoles ($\ell > 0$) encode anisotropic contributions. The angular power spectrum is then defined as

$$C_\ell = \frac{1}{2\ell+1} \sum_{m=-\ell}^{\ell} |c_{\ell m}|^2, \tag{105}$$

and the fractional anisotropy is characterised by $C_{\ell>0}/C_0$.

In the PTA context, the expected correlation between pulsar timing residuals a and b is given by the ORF,

$$\Gamma_{ab} = \frac{3}{8\pi}(1+\delta_{ab}) \int_{S^2} \mathrm{d}\hat{\Omega}\, P\left(\hat{\Omega}\right) \sum_{q=+,\times} F^q{}_{\mathrm{a}}\left(\hat{\Omega}\right) F^q{}_b\left(\hat{\Omega}\right), \tag{106}$$

where $F^q{}_a$ are the antenna response functions. The isotropic HD curve emerges as the special case with $c_{00} \neq 0$ and $c_{\ell m} = 0$ for $\ell > 0$.

12.2. NANOGrav results

The NANOGrav 15 yr dataset was analysed in this framework [13]. Posterior distributions for $c_{\ell m}$ are consistent with isotropy, with a Bayesian 95% upper limit of

$$\frac{C_{\ell>0}}{C_0} < 0.2, \tag{107}$$

across $\ell = 1$–6. Map reconstructions show low-significance features (e.g. excess power near RA $\sim$3h), but the global BF in favour of anisotropy is $\sim$2. Frequentist optimal-statistics tests yield $p \simeq 0.05$ for anisotropic components, values expected from noise fluctuations.

12.3. MPTA results

The MPTA applied the same formalism to its 4.5 yr dataset [173]. Using $\ell_{\max} = 8$, corresponding to an angular resolution of $\sim$23°, the recovered spherical-harmonic maps in frequency bins $f = 7$–21 nHz are consistent with isotropy. A hotspot at $f = 7$ nHz has nominal significance

$$p = 0.015, \tag{108}$$

but this vanishes once look-elsewhere corrections are applied. No evidence for point-like anisotropy is found in radiometer maps.

12.4. Summary

NANOGrav and MPTA data constrain anisotropy in the nHz GWB to $\lesssim 20\%$ of the monopole component, in agreement with expectations for a stochastic SMBHB population. The spherical-harmonic formalism provides a unified framework in which isotropy is a special case, but current datasets show no statistically significant departure from it. Larger arrays with greater sky coverage (e.g. SKA) will be required to detect anisotropy with confidence.

13. Is the currently detected GWB non-stationary?

An unusual feature of recent PTA results is that newer datasets tend to show stronger support for the presence of a HD correlated process. For example, the EPTA DR2New/+ configuration,

which uses only the most recent ∼10 yr of data, returns a much higher BF for the HD model than the DR2Full/+ configuration, which extends the same dataset back to ∼24 yr. Similarly, the NANOGrav 15 yr dataset, covering a shorter timespan, yields a much higher BF than the longer EPTA and PPTA datasets, while the CPTA dataset (∼2.5 yr) achieves the highest detection significance. To compound this tension, the deepest upper limit on the GWB amplitude from the PPTA in 2015 [360] lies significantly below the amplitudes recovered currently. A trivial explanation would be that the GWB itself is not stationary, contrary to standard assumptions. However, it is also possible that non-stationary noise in individual pulsars drives varying sensitivity across datasets of different spans.

13.1. PPTA results

The PPTA analysed their dataset using sliding windows of 6 and 9 years with a fixed spectral index $\gamma = 13/3$. In early windows no common red process was detected and only 95% upper limits were obtained. In later windows detections were recovered with 95% credible intervals. The bounds increase with time, consistent with previous limits [28, 360, e.g.].

Early observations used less sensitive backend systems, giving higher limits due to reduced bandwidth and digital artefacts [226, 275]. In 2010–2012 no common red process was found, with

$$A_{\rm CRN} < \left(1.2 \times 10^{-15}\right) - \left(1.5 \times 10^{-15}\right), \tag{109}$$

below the full-dataset value,

$$A_{\rm CRN} = (2.0 \pm 0.2) \times 10^{-15}. \tag{110}$$

The first 9 year slice ($A_{\rm CRN} < 1.2 \times 10^{-15}$) agrees with earlier limits [28, 360]. The most recent 6 year slice gives

$$A_{\rm CRN} = \left(2.7^{+0.7}_{-0.8}\right) \times 10^{-15}, \tag{111}$$

consistent with the full span. Using fewer pulsars [360] can underestimate limits [214], but this does not explain the variation, since all pulsars were included in each slice with consistent priors and noise models. The first three 9 year slices remain incompatible with later amplitudes. The uncorrelated common-spectrum amplitude,

$$\log_{10} A_{\rm CRN} = -14.69, \tag{112}$$

lies at the 99.8th percentile of reweighted samples from the first 9 year window. Some variability is expected for a stochastic background [181], but the variation reported is larger than anticipated.

13.2. EPTA results

The EPTA carried out a similar analysis [143] of the DR2full dataset spanning 24.7 yr [139]. The GWB was modelled as a power-law process with HD spatial correlations [17, 184], and pulsar models included red and dispersion-measure noise [140] using `enterprise` [135]. A time-slice analysis [146] gave broad posteriors in the earliest slice and tighter constraints in later slices. The latter agree with recent results [141]. A small reduction in γ was noted, but uncertainties in the first slice prevent interpretation.

To test for non-stationarity, the EPTA introduced a time-dependent spectrum,

$$\begin{aligned}\log_{10}A(t) &\approx \log_{10}A(t_0) + a\frac{t-t_0}{T},\\ \gamma(t) &\approx \gamma(t_0) + b\frac{t-t_0}{T},\end{aligned} \tag{113}$$

with Gaussian priors $\mathcal{N}(0,1)$ on a and b. The recovered parameters [146] were

$$\begin{aligned}\log_{10}A(t_0) &= -14.35^{+0.20}_{-0.23},\\ \gamma(t_0) &= 3.72^{+0.46}_{-0.47},\\ a &= 0.0^{+0.3}_{-0.3},\\ b &= -0.7^{+0.7}_{-0.6},\end{aligned}$$

with BF $B^S_{\rm NS} = 1.5$, indicating no evidence for non-stationarity. The mild trends are consistent with changes in data quality rather than intrinsic evolution.

Individual pulsars were also tested [141]. Most showed no support for non-stationarity ($\log_{10}B^S_{\rm NS} \leqslant 2$). J1713+0747 yielded $\log_{10}B^S_{\rm NS} = 4.3$, but this reduced to -0.6 once exponential dip events were included, consistent with stationarity.

Simulations showed that eccentric binaries with $e \gtrsim 0.4$ can mimic non-stationarity, producing systematic shifts in a and b and BFs favouring non-stationarity [146, 380, 386]. No such evidence is present in the EPTA data. The results are therefore consistent with a stationary GWB, as in the PPTA analysis.

14. A new era of operational low-frequency GW detectors

As exciting as the PTA results are, the next few years and decades promise to rapidly expand our view of the low-frequency GW universe through a number of experiments, from the sub-nHz to the μHz. While the adoption of the LISA by the European Space Agency guarantees a new probe of the mHz regime, the nHz regime will be intensely probed by the upcoming SKA PTA. MPTA, which is a precursor instrument for the SKA-mid (frequency) instrument already shows the great promise that even the currently promised configurations of the SKA hold. Further, the gamma ray PTA (GPTA) [1] seeks to remove one of the most challenging issues of radio PTAs—the challenge of removing the noise from DM variations. As demonstrated by Ferranti and collaborators [150] the lack of adequate DM sensitivity can significantly degrade the sensitivity of a PTA, by exchanging power between chromatic DM process and achromatic red noise processes. Beyond time-domain techniques, the availability of very high precision astrometry of stars using optical surveyors such as Gaia has led to a revival of interest in the astrometric techniques of Book and Flannagan [65], offering a possible commentary probe of the nHz regime. In the following sections I summarise the features and possibilities of these experiments.

14.1. Gamma ray PTA

The large area telescope (LAT) on the Fermi Gamma-ray Space telescope has been surveying the sky between 30 MeV and 1 TeV since August 2008 [32]. One of its early achievements was the detection of γ-ray pulsations from a population of known MSPs [5]. Since then, radio searches for pulsations in unassociated LAT sources have been particularly effective in discovering new MSPs, leading to a population of over 100 γ-ray MSPs [336].

Because Fermi continually monitors these pulsars, its data set effectively functions as a γ-ray PTA [1, GPTA]. Using 35 of the γ-brightest MSPs and about 12.5 year of LAT data (GPTA DR1), this leads to a 95% upper limit on the GWB strain of 1.0×10^{-14} at a frequency of $1\,\mathrm{yr}^{-1}$, with this limit scaling as $T_{\mathrm{obs}}^{-13/6}$, meaning that longer observation times improve constraints.

Pulsar spin noise and propagation effects, such as DM variations, could mimic GWB signals. However, γ-ray observations eliminate most ISM effects seen in radio observations.

In the latest analysis of 14.5 year of data [225], two methods were used to analyse the data: photon-by-photon analysis with microsecond precision and TOA analysis, both of which yielded consistent results. Upper limits on the GWB strain were derived from both approaches.

The photon-by-photon GWB analysis uses maximum likelihood techniques, incorporating degrees of freedom for spin noise and GWB into the likelihood expression:

$$\log L = \sum_i \left[\log\left(w_i f(\phi[t_i,\lambda,\beta]) + (1-w_i)\right)\right] - \frac{1}{2}\sum_{k,l}\beta_k C_{kl}^{-1}\beta_l - \frac{1}{2}\log\det(C) \tag{114}$$

where β_k are Fourier coefficients representing potential noise signals. The phase model $\phi(t,\lambda,\beta)$ includes the spin frequency ν, and the analysis constrains the GWB amplitude A_{gwb} by marginalizing over nuisance parameters.

Using the new dataset and both the old (energy-independent) and new (energy-dependent) pulse profile models, the unbinned analysis from [1] was repeated to estimate a 95% confidence limit on the GWB amplitude, A_{gwb}. Depending on the specific details of the noise modelling, a range of upper limits are obtained. With the old models

$$A_{\mathrm{gwb}} < (6.9 - 7.5) \times 10^{-15},$$

while with the new energy-dependent models

$$A_{\mathrm{gwb}} < (6.4 - 7.0) \times 10^{-15}.$$

with the mid-range value, $A_{\mathrm{gwb}} < 6.7 \times 10^{-15}$, providing a characteristic limit. This approach only constrains common noise processes and does not use correlation information.

The DR1 limit, $A_{\mathrm{gwb}} < 10 \times 10^{-15}$, was expected to scale to 7.3×10^{-15} simply by increasing the dataset from 12.5 to 14.5 years. The DR2 results that used the old pulse profile models align closely with this expectation. Since the preliminary analysis did not incorporate spatial information (HD correlations), the additional pulsars in the sample did not contribute significantly to the improvement. In general, the cross-spectrum of pulsar timing residuals can be written as

$$S_{ij}(f) \equiv \langle \tilde{r}_i(f)\, \tilde{r}_j^*(f)\rangle = \frac{\Gamma_{ij}}{12\pi^2 f^2}\, S_h(f)\,, \tag{115}$$

where $S_h(f)$ is the one-sided strain PSD and Γ_{ij} is the HD overlap reduction function:

$$\Gamma_{ij}(\zeta_{ij}) = \begin{cases} \dfrac{3}{2}x\ln x - \dfrac{1}{4}x + \dfrac{1}{2}, & i \neq j, \\ 1, & i = j, \end{cases} \qquad x \equiv \frac{1-\cos\zeta_{ij}}{2}, \tag{116}$$

with ζ_{ij} as the angular separation between pulsars i and j.

With this scaling alone, the GPTA sensitivity should reach the level of the GWB candidate signal by 2030. Including energy dependence in the pulse profile modelling improves the sensitivity by nearly 10%. A final analysis of the GPTA DR2 data will include spatial correlations, which are expected to enhance the sensitivity by an additional 10%–15%.

14.2. Astrometric approaches to nHz GW detection

Astrometry, the precise measurement of star motions, offers a complementary method to PTAs for detecting low-frequency GWs by measuring the spatial deflection of photons induced by them. Future missions like Gaia, Theia, and the Nancy Grace Roman space telescope (Roman) could not only validate PTA findings but also explore the frequency gap between PTAs and LISA.

Astrometric techniques are expected to remain sensitive to GW-induced strain over a broad range of frequencies between $10^{-18}\,\mathrm{s}^{-1} \lesssim f \lesssim 10^{-8}\,\mathrm{s}^{-1}$, offering a bridge between cosmic microwave background polarization measurements and the frequencies probed by PTAs and LISA.

Astrometric data, such as that from Gaia and extragalactic radio sources, already place an upper limit on the energy density of the stochastic GWB (SGWB) of $\Omega_{\rm gw}(f) < 0.011$ for frequencies $6 \times 10^{-18}\,\mathrm{s}^{-1} \lesssim f \lesssim 10^{-9}\,\mathrm{s}^{-1}$. Future missions are expected to improve this sensitivity. Due to the larger number of observed 'detectors' and the concentration of pulsars and stars toward the Galactic Center, astromteric techniques are likely to be more sensitive to anisotropy of the nHz GWB than PTAs. Additionally, the presence of parity-odd correlations among astrometric observables, or cross-correlations between PTAs and astrometry, could reveal the chirality of the SGWB, thereby constraining modified theories of gravity. These correlations, represented by generalized HD curves, adding additional layers of information for SGWB detection.

For both PTA and astrometric detection of the SGWB, GWs perturb photon geodesics, resulting in shifts in either photon arrival times (measured by PTAs) or the proper motion of sources (measured by astrometry). These perturbations can be described by the GW strain, $h_{ij}(t)$, which is a sum over frequency modes:

$$h_{ij}(t) = \int_{-\infty}^{\infty} \mathrm{d}f \int \mathrm{d}^2\hat{\Omega} \sum_P h_{\rm P}\left(f,\hat{\Omega}\right) \epsilon_{ij}^{P}\left(\hat{\Omega}\right) \mathrm{e}^{2\pi i f t}, \tag{117}$$

where f is the frequency, $\hat{\Omega}$ the incoming direction, and P the polarization mode. The observable response in either PTAs (photon redshift δz) or astrometry (proper motion δx) is given by the integral:

$$X(f) = \int_{S^2} \mathrm{d}^2\hat{\Omega} \sum_{\rm P} h_{\rm P}\left(f,\hat{\Omega}\right) \epsilon_{ij}^{P}\left(\hat{\Omega}\right) R_{ij}^{X}\left(\hat{\Omega},\hat{n}\right), \tag{118}$$

where R_{ij}^{X} represents the response function for either PTAs or astrometry.

The correlation functions for GW-induced redshifts (PTAs) or proper motions (astrometry) can be expressed using generalized Hellings-Downs curves, which account for both intensity $I(f)$ and circular polarization $V(f)$:

$$\left\langle X_{\rm a}(f) X_b^{*}\left(f'\right)\right\rangle = \delta\left(f-f'\right) \sum_{P,P'} P_{\rm P}^{P'}(f)\ \Gamma_{ab}^{XX';PP'}, \tag{119}$$

where $P_{\rm P}^{P'}(f)$ is the power spectrum of the GWB, and the correlation functions Γ for redshift and proper motion are known as the generalized HD curves [200].

$$\Gamma_{\rm ab}^{XX';PP'} \equiv \int \mathrm{d}^2\hat{\Omega}\ \epsilon_{ij}^{P}\left(\hat{\Omega}\right)\ \epsilon_{kl}^{P'}\left(\hat{\Omega}\right)^{*} R^{X,ij}\left(\hat{\Omega},\hat{n}_{\rm a}\right) R^{X',kl}\left(\hat{\Omega},\hat{n}_b\right). \tag{120}$$

For astrometry, these generalized HD functions describe how correlations in stellar proper motions depend on angular separation, and they reduce to the familiar PTA HD form in the redshift case. Their structure encodes more than geometry: parity-odd contributions, for instance,

would signal a chiral GW background [255]. While astrometric data provide a direct testbed for such effects, similar polarization-sensitive correlations could also be exploited in other experiments targeting the nHz band [348].

14.3. Pulsar polarisation arrays

Pulsar polarisation arrays (PPAs) are a recently proposed observational approach that parallels PTAs, but focuses on polarisation signals rather than pulse arrival times [261]. While PTAs detect GWs through correlations in the timing residuals of multiple MSPs, PPAs search for correlated variations in pulsar polarisation, potentially revealing novel astrophysics or fundamental physics.

PPAs target cosmic birefringence induced by ultralight axion-like $\mathcal{DM}$ (AL$\mathcal{DM}$), causing oscillations in the polarisation angle (PA) of photons traversing the Galaxy [424]. Detecting a common, coherent oscillation in PA across pulsars would indicate AL$\mathcal{DM}$-induced birefringence. Theoretical studies indicate that PPAs can probe axion-photon couplings as small as 10^{-17} GeV^{-1} for axion masses in the range 10^{-27}–10^{-21} eV.

14.4. Theoretical motivation and formulation

AL$\mathcal{DM}$ can be modeled as a classical, oscillating scalar field permeating the Galaxy [329]. It couples to the electromagnetic field via a Chern–Simons term, leading to cosmic birefringence: a rotation in the plane of linear polarisation of photons traversing the field. The predicted rotation angle $\Delta\Psi$ for a pulsar's radio emission is given by:

$$\Delta\Psi\left(t\right) = \frac{g_{a\gamma}}{2}\left[a\left(t_{\text{emit, pulsar}}\right) - a\left(t_{\text{recv, Earth}}\right)\right], \tag{121}$$

where $g_{a\gamma}$ is the axion-photon coupling constant, and $a(t)$ is the AL$\mathcal{DM}$ field amplitude. Assuming a monochromatic AL$\mathcal{DM}$ field $a(t) \propto \cos(m_a t + \phi)$, where m_a is the axion mass, this induces an oscillatory, frequency-independent rotation of the PA with frequency $f_a \approx m_a/(2\pi)$.

14.5. Observations and data products

The Parkes PPA study analysed polarisation data from 22 MSPs over 2004–2022 [424]. Stokes parameters (I, Q, U, V) were calibrated using standard procedures [261], and Faraday rotation due to the ISM and Earth's ionosphere was corrected [424]. A standard position angle (PA) profile was subtracted from each observation to extract residual PA offsets $\Delta\text{PA}_\text{p}(t_n)$, yielding time series for each pulsar suitable for detecting time-variable effects.

The EPTA study similarly analysed polarisation data from 12 MSPs in the EPTA dataset, selecting those with high linear polarisation [329].

14.6. Noise modelling

The observed PA residuals are modelled as:

$$\Delta\text{PA}_\text{p}\left(t\right) = S_\text{p}\left(t\right) + I_\text{p}\left(t\right) + W_\text{p}\left(t\right) + R_\text{p}\left(t\right) + D_\text{p}\left(t\right), \tag{122}$$

where $S_\text{p}(t)$ is the potential AL$\mathcal{DM}$ signal, $I_\text{p}(t)$ residual ionospheric Faraday rotation, $W_\text{p}(t)$ white noise (including measurement and jitter noise), $R_\text{p}(t)$ red noise (e.g. ISM or systematics), and $D_\text{p}(t)$ deterministic trends (polynomial terms for long-term drifts). However, the $R_\text{p}(t)$

contribution is expected to be far below the RM sensitivity of current telescopes and can be ignored in realistic analyses.

As in PTAs, red noise is modelled as a power-law Gaussian process with spectrum $P(f) \propto f^{-\gamma}$. Additional white-noise terms account for excess scatter beyond formal measurement uncertainties.

14.7. Common AL$\mathcal{DM}$ signal model

An AL$\mathcal{DM}$-induced signal produces correlated PA oscillations across the pulsar array. The signal covariance matrix $\mathbf{C}(m_{\rm a}, g_{\rm a\gamma})$ encodes both temporal and spatial correlations between pulsars, derived from the theoretical two-point correlation function of the AL$\mathcal{DM}$ field [329].

For nearby pulsars ($L_{\rm p} \ll L_{\rm coh}$), where $L_{\rm coh}$ is the AL$\mathcal{DM}$ coherence length, both Earth and pulsar terms in $S_{\rm p}(t)$ contribute coherently, enhancing inter-pulsar correlations. The signal model predicts a nearly common oscillation across the array, with frequency $f_{\rm a} = m_{\rm a}/(2\pi)$ and amplitude proportional to $g_{\rm a\gamma}$.

14.8. Statistical inference approach

The Parkes PPA study employs a Bayesian Gaussian-process framework. The total covariance $\mathbf{Cov} = \mathbf{N} + A^2\mathbf{C}$ combines noise ($\mathbf{N}$) and AL$\mathcal{DM}$ signal covariance ($\mathbf{C}$), with A proportional to $g_{\rm a\gamma}$. Marginal likelihoods over A are computed for each axion mass hypothesis $m_{\rm a}$, yielding 95% credible upper limits on $g_{\rm a\gamma}$ [424].

Bayes factors compare models with and without a common AL$\mathcal{DM}$ signal. In the Parkes analysis, no significant preference for a signal model was found [424].

The EPTA study applied both Bayesian and frequentist methods. Lomb–Scargle periodograms searched for periodicities, and a Bayesian sinusoidal model accounted for known systematics (e.g. annual ionospheric effects). No significant common signal was detected [329].

Both studies set competitive upper limits on $g_{\rm a\gamma}$, with the Parkes PPA placing the most stringent constraints to date in the mass range 10^{-22}–10^{-21} eV, reaching $g_{\rm a\gamma} \lesssim 10^{-13.5}$–$10^{-12.2}$ GeV^{-1} [424].

14.9. First PPA limits with PPTA

The first practical implementation of PPAs used PPTA data from 22 pulsars [424]. The analysis searched for correlated oscillations in PA residuals analogous to timing residual analysis in PTAs. No AL$\mathcal{DM}$ signature was detected, resulting in the first observational limits on axion-photon coupling:

$$g_{\rm a\gamma} \lesssim 10^{-13.5}\text{–}10^{-12.2}\,\text{GeV}^{-1}, \quad \text{for} \quad m_{\rm a} = 10^{-22}\text{–}10^{-21}\,\text{eV}, \tag{123}$$

assuming a local DM density $\rho_0 = 0.4\,\text{GeV/cm}^3$ [424]. These represent the strongest astrophysical constraints in this axion mass window, emphasizing cross-correlations among pulsars as key discriminants against noise.

14.10. EPTA polarisation search results

The EPTA independently analysed polarisation data from 12 pulsars, employing both frequentist (Lomb–Scargle periodogram) and Bayesian analyses [329]. Initially, a common oscillation between 10^{-8} and 2×10^{-8} Hz was detected but subsequently attributed to residual Faraday

rotation in Earth's ionosphere rather than AL$\mathcal{DM}$. Correcting for ionospheric effects, no axion-like signal remained, allowing the EPTA to place upper limits on $g_{a\gamma}$:

$$g_{a\gamma} \lesssim 10^{-13}\text{–}10^{-12}\,\mathrm{GeV}^{-1}, \quad \text{for} \quad m_a = 6\times10^{-24}\text{–}5\times10^{-21}\,\mathrm{eV}, \tag{124}$$

which align with existing astrophysical bounds [329]. The EPTA analysis identified significant challenges from ionospheric and calibration systematics, suggesting improved multi-frequency observations and additional pulsars could enhance sensitivity.

14.11. Conclusion

PPAs offer a novel approach to constrain axion-photon coupling via correlated polarisation rotations and their current sensitivities have reached $g_{a\gamma} \sim 10^{-13}\text{–}10^{-12}\,\mathrm{GeV}^{-1}$, rivalling established methods. The potential of PPAs with upcoming searches using SKA-precursor datasets promises to deepen these limits significantly and the SKA era will herald the deepest searches and likely detection of such signals. However, in a very classical sense, achieving those remarkable results requires not only improvements in radio astronomical techniques but also in our understanding and modelling of ionospheric phenomena.

15. Closing remarks

The strong evidence for a spatially correlated signal that has emerged in various PTA datasets marks a turning point for nHz frequency GW research. It is challenging to fairly summarise the many different impacts these results have already had, and even more challenging to predict the future of the field. However, the under the umbrella of the IPTA all the PTAs are coming together to put together the largest PTA dataset produced till date. Although this dataset will be replaced by larger and more sensitive datasets within the next few years, the significant boost to signal sensitivity has encouraged a vast diversity of research that is being attempted with IPTA scale datasets.

Scientifically, the many themes reported in this review are being actively pursued by groups within the IPTA as well as independent groups. At the same time, technically and in terms of the scientific culture, the IPTA is starting to become the driver of PTA research. While this presents several challenges, from coordinating work at individual group level across the world to optimise the scientific returns to figuring out the details of providing access to the data archives from all major radio observatories in the world governed by diverse institutional, national and regional regulations to a set of globally distributed collaborators, this also marks a rapid growth in the scientific endeavour of PTA research. The IPTA is seeing a remarkable growth, from pulsar timing and radio astronomical experts globally coordinating their expertise to dig deep into the very fundamental instruments, tools and techniques used for high-precision pulsar timing to improve our ability to model the various sources of nuisance terms in PTAs to serious efforts to uncover the underlying signal—not only as a contrast between 'astrophysical' SMBHB inspiral driven GWs, cosmologically sourced GWBs or signals arising from 'new physics' but also as possibly a combination of these.

In each of these several difficulties must be overcome. PTA observers must understand the implications of GW and other stochastic signals in their data at unprecedented precision, while improving our ability to connect statistically derived noise models with an increasing knowledge of the physics of NSs, their emission and the behaviour of the ISM, the solar wind and the terrestrial ionosphere. Much of this will only happen by incorporating approaches and results from communities beyond traditional PTA research, such as the heliophysics and geophysics communities as well as improving techniques using input from closely related communities

such the NSs magnetosphere and emission physics community. At the same time, the PTA community must also interact far more closely with external groups to improve our searches for signals. These include incorporating the efforts and involvement of the black hole physics community through dedicated simulation efforts constrained by the latest and future electromagnetic surveys; the cosmology community through improved modelling of those backgrounds; and the particle physics community through increased efforts to deepen searches for exotic signals.

However, the GW window is expanding fast and the prospect of observing the GW universe from sub-nHz up to MHz will be key to unravelling several regimes of physics that cannot be probed through singular experiments. Simultaneously, this multiband effort will require regular multi-messenger astronomy, requiring key support from current and proposed EM observatories to continue their impressive growth in sensitivity and speed. At the centre of this explosive growth and key to the success of this field lie early career researchers, whose personal and collaborative scientific success and growth is required by the field for its own growth and success. These are truly exciting times.

The emerging PTA detection era is naturally complementary to forthcoming space- and ground-based interferometers such as LISA and the ET. PTAs probe the nHz GW regime, providing population-level constraints on the early inspiral phases of SMBHBs and the low-frequency tail of any stochastic background. LISA will access millihertz frequencies, tracking individual massive binaries through their late inspiral, while ET will reach the kilohertz band relevant to stellar-mass mergers. Together, these facilities will establish a continuous, multi-decade frequency baseline—from $\sim 10^{-9}$ Hz to $\sim 10^{3}$ Hz—linking the dynamical evolution of compact objects across cosmic time. Coordinated analysis between PTAs, LISA, and ET will enable genuine multi-band GW astrophysics, constraining binary demographics, environmental coupling, and potential deviations from general relativity in a single, coherent framework.

Data availability statement

No new data were created or analysed in this study.

Acknowledgments

I am deeply grateful to Drs C Tiburzi, J P W Verbiest, Prof. A Sesana, and Dr D Izquierdo-Villalba for their invaluable discussions and support; to Drs A Possenti, M Falxa, R Busicchio, and P Coles for their insightful suggestions and debate; and to my students G Fumagalli, S Valtollina, B Moreschi, I Ferranti, S Manzini, and F Fantoccoli for their dedication and enthusiasm, which has helped me recover my own. This work was supported by the European Research Council under the ERC Consolidator Grant B MASSIVE (Grant Agreement No. 818691) and by the INFN Specific Initiative TEONGRAV. I also thank the members of the EPTA, IPTA, and MPTA collaborations, along with friends, colleagues, and collaborators across the global PTA community, and extend my heartfelt appreciation to the Gravitational Wave Early Career Scientists for showing me a hopeful future.

Author contribution

G M Shaifullah 0000-0002-8452-4834
Conceptualization (lead), Investigation (lead), Methodology (lead), Project administration (lead), Resources (lead), Visualization (lead), Writing – original draft (lead), Writing – review & editing (lead)

References

[1] The Fermi-LAT Collaboration 2022 A gamma-ray pulsar timing array constrains the nanohertz gravitational wave background *Science* **376** 521–3
[2] Aaij R *et al* 2024 Search for prompt production of pentaquarks in charm hadron final states *Phys. Rev. D* **110** 032001
[3] Abbott B P *et al* 2016 Tests of general relativity with GW150914 *Phys. Rev. Lett.* **116** 221101
[4] Abbott L F and Wise M B 1984 Constraints on generalized inflationary cosmologies *Nucl. Phys. B* **244** 541–8
[5] Abdo A A *et al* 2009 Detection of 16 gamma-ray pulsars through blind frequency searches using the Fermi LAT *Science* **325** 840–4
[6] Abdo A A *et al* 2013 The second Fermi Large Area Telescope catalog of gamma-ray pulsars *Astrophys. J. Suppl. Ser.* **208** 17
[7] Ade P A R *et al* 2021 Improved constraints on primordial gravitational waves using Planck, WMAP and BICEP/Keck observations through the 2018 observing season *Phys. Rev. Lett.* **127** 151301
[8] Agazie G *et al* 2024 The NANOGrav 12.5-year data set: search for gravitational wave memory *ApJ* **963** 61
[9] Agazie G *et al* 2023 The NANOGrav 12.5-year data set: search for gravitational wave memory (arXiv:2307.13797)
[10] Agazie G *et al* 2023 The NANOGrav 15 yr data set: Bayesian limits on gravitational waves from individual supermassive black hole binaries *Astrophys. J. Suppl. Lett.* **951** L50
[11] Agazie G *et al* 2023 The NANOGrav 15 yr data set: constraints on supermassive black hole binaries from the gravitational-wave background *Astrophys. J. Suppl. Lett.* **952** L37
[12] Agazie G *et al* 2023 The NANOGrav 15 yr data set: evidence for a gravitational-wave background *Astrophys. J. Suppl. Lett.* **951** L8
[13] Agazie G *et al* 2023 The NANOGrav 15 yr data set: search for anisotropy in the gravitational-wave background *Astrophys. J. Suppl. Lett.* **956** L3
[14] Aggarwal K *et al* 2019 The NANOGrav 11 yr data set: limits on gravitational waves from individual supermassive black hole binaries *Astrophys. J.* **880** 116
[15] Alabidi L, Kohri K, Sasaki M and Sendouda Y 2013 Observable induced gravitational waves from an early matter phase *J. Cosmol. Astropart. Phys.* JCAP05(2013)033
[16] Allen B and Koranda S 1994 CBR anisotropy from primordial gravitational waves in inflationary cosmologies *Phys. Rev. D* **50** 3713–37
[17] Allen B and Romano J D 2023 Hellings and Downs correlation of an arbitrary set of pulsars *Phys. Rev. D* **108** 043026
[18] Alpar M A, Cheng A F, Ruderman M A and Shaham J 1982 A new class of radio pulsars *Nature* **300** 728–30
[19] Amelino-Camelia G 2013 Quantum-spacetime phenomenology *Living Rev. Relativ.* **16** 5
[20] Anber M M and Sorbo L 2012 Non-Gaussianities and chiral gravitational waves in natural steep inflation *Phys. Rev. D* **85** 123537
[21] Antoniadis J *et al* 2022 The International Pulsar Timing Array second data release: search for an isotropic gravitational wave background *Mon. Not. R. Astron. Soc.* **510** 4873–87
[22] Antoniadis J *et al* 2013 A massive pulsar in a compact relativistic binary *Science* **340** 448
[23] Antoniadis J, Kaplan D L, Stovall K, Freire P C C, Deneva J S, Koester D, Jenet F and Martinez J G 2016 An eccentric binary millisecond pulsar with a helium white dwarf companion in the galactic field *Astrophys. J.* **830** 36
[24] Arai S *et al* 2023 Cosmological gravity probes: connecting recent theoretical developments to forthcoming observations *Prog. Theor. Exp. Phys.* **2023** 072E01

[25] Archibald A M, Gusinskaia N V, Hessels J W T, Deller A T, Kaplan D L, Lorimer D R, Lynch R S, Ransom S M and Stairs I H 2018 Universality of free fall from the orbital motion of a pulsar in a stellar triple system *Nature* **559** 73–76
[26] Armstrong J W, Rickett B J and Spangler S R 1995 Electron density power spectrum in the local interstellar medium *Astrophys. J.* **443** 209
[27] Arons J and Barnard J J 1986 Wave propagation in pulsar magnetospheres: dispersion relations and normal modes of plasmas in superstrong magnetic fields *Astrophys. J.* **302** 120
[28] Arzoumanian Z *et al* 2018 The NANOGrav 11-year data set: high-precision timing of 45 millisecond pulsars *Astrophys. J. Suppl. Ser.* **235** 37
[29] Arzoumanian Z *et al* 2020 The NANOGrav 12.5 yr data set: search for an isotropic stochastic gravitational-wave background *Astrophys. J. Suppl. Lett.* **905** L34
[30] Ashrafzadeh A, Solbi M, Heydari S and Karami K 2025 Primordial black holes in SB SUSY Gauss-Bonnet inflation *J. Cosmol. Astropart. Phys.* JCAP01(2025)025
[31] Asseo E and Melikidze G I 1998 Coherent radio emission models in pulsars *Mon. Not. R. Astron. Soc.* **301** 59
[32] Atwood W B *et al* 2009 The large area telescope on the Fermi gamma-ray space telescope mission *Astrophys. J.* **697** 1071–102
[33] Babak S *et al* 2016 European Pulsar Timing Array limits on continuous gravitational waves from individual supermassive black hole binaries *Mon. Not. R. Astron. Soc.* **455** 1665–79
[34] Babak S and Sesana A 2012 Resolving multiple supermassive black hole binaries with pulsar timing arrays *Phys. Rev. D* **85** 044034
[35] Backer D C 1970 Correlated subpulse structure in PSR 1237 + 25 *Nature* **228** 752–5
[36] Bailes M *et al* 2016 MeerTime—the MeerKAT key science program on pulsar timing *Proc. Sci.* **277** 11
[37] Bailes M *et al* 2020 The MeerKAT telescope as a pulsar facility: system verification and early science results from MeerTime *Publ. Astron. Soc. Aust.* **37** e028
[38] Bak Nielsen A -S *et al* 2020 Timing stability of three black widow pulsars *Mon. Not. R. Astron. Soc.* **494** 2591–9
[39] Balaji S, Domènech G and Franciolini G 2023 Scalar-induced gravitational wave interpretation of PTA data: the role of scalar fluctuation propagation speed *J. Cosmol. Astropart. Phys.* JCAP10(2023)041
[40] Barman B, Das A, Das S J and Merchand M 2025 Hunting for heavy Z' with IceCube neutrinos and gravitational waves *Phys. Rev. D* **112** 035035
[41] Barnaby N, Moxon J, Namba R, Peloso M, Shiu G and Zhou P 2012 Gravity waves and non-Gaussian features from particle production in a sector gravitationally coupled to the inflaton *Phys. Rev. D* **86** 103508
[42] Bartolo N, Matarrese S, Riotto A and Väihkönen A 2007 Maximal amount of gravitational waves in the curvaton scenario *Phys. Rev. D* **76** 061302
[43] Bartolo N *et al* 2016 Science with the space-based interferometer LISA. IV: probing inflation with gravitational waves *J. Cosmol. Astropart. Phys.* JCAP12(2016)026
[44] Bassa C G *et al* 2016 A millisecond pulsar in an extremely wide binary system *Mon. Not. R. Astron. Soc.* **460** 2207–22
[45] Basu R, Athreya R and Mitra D 2011 Detection of off-pulse emission from PSR B0525+21 and PSR B2045-16 *Astrophys. J.* **728** 157
[46] Basu R, Mitra D, Melikidze G I and Skrzypczak A 2019 Classification of subpulse drifting in pulsars *Mon. Not. R. Astron. Soc.* **482** 3757–88
[47] Baym G, Hatsuda T, Kojo T, Powell P D, Song Y and Takatsuka T 2018 From hadrons to quarks in neutron stars: a review *Rep. Prog. Phys.* **81** 056902
[48] Becker W 2009 X-ray emission from pulsars and neutron stars *Neutron Stars and Pulsars (Astrophysics and Space Science Library)* vol 357 (springer) p 91
[49] Bécsy B, Cornish N and Kelley L 2022 Searching for individual supermassive black hole binaries and a stochastic background in population-based simulated pulsar timing array datasets *American Astronomical Society Meeting (American Astronomical Society Meeting Abstracts)* vol 240 p 348.04 (available at: https://ui.adsabs.harvard.edu/abs/2022AAS...24034804B)
[50] Bécsy B and Cornish N J 2020 Joint search for isolated sources and an unresolved confusion background in pulsar timing array data *Class. Quantum Grav.* **37** 135011
[51] Benabou J N, Buschmann M, Kumar S, Park Y and Safdi B R 2024 Signatures of primordial energy injection from axion strings *Phys. Rev. D* **109** 055005

[52] Benetti M, Graef L L and Vagnozzi S 2022 Primordial gravitational waves from NANOGrav: a broken power-law approach *Phys. Rev. D* **105** 043520
[53] Bernardo R C and Ng K -W 2024 Beyond the Hellings–Downs curve: non-Einsteinian gravitational waves in pulsar timing array correlations *Astron. Astrophys.* **691** A126
[54] Bhattacharya D and Srinivasan G 1991 Gamma rays from millisecond pulsars *J. Astrophys. Astron.* **12** 17–25
[55] Bi Y-C, Wu Y-M, Chen Z-C and Huang Q -G 2024 Constraints on the velocity of gravitational waves from the NANOGrav 15-year data set *Phys. Rev. D* **109** L061101
[56] Biagetti M, Fasiello M and Riotto A 2013 Enhancing inflationary tensor modes through spectator fields *Phys. Rev. D* **88** 103518
[57] Biagetti M, Dimastrogiovanni E, Fasiello M and Peloso M 2015 Gravitational waves and scalar perturbations from spectator fields *J. Cosmol. Astropart. Phys.* JCAP04(2015)011
[58] Biggs J D 1992 An analysis of radio pulsar nulling statistics *Astrophys. J.* **394** 574
[59] Bird S, Cholis I, Muñoz J B, Ali-Haïmoud Y, Kamionkowski M, Kovetz E D, Raccanelli A and Riess A G 2016 Did LIGO detect dark matter? *Phys. Rev. Lett.* **116** 201301
[60] Blanchard C, Guillemot L, Voisin G, Cognard I and Theureau G 2025 A census of galactic spider binary millisecond pulsars with the Nançay Radio Telescope *Astron. Astrophys.* **698** A239
[61] Blandford R D 1974 Electrodynamics and astrophysical applications of strong waves *PhD Thesis* Defense Technical Information Center
[62] Bochenek C, Ransom S and Demorest P 2015 The feasibility of using black widow pulsars in pulsar timing arrays for gravitational wave detection *Astrophys. J. Suppl. Lett.* **813** L4
[63] Bodas A, Buen-Abad M A, Hook A and Sundrum R 2024 A closer look in the mirror: reflections on the matter/dark matter coincidence *J. High Energy Phys.* JHEP06(2024)052
[64] Bolívar L B, Huergo D, Santos F L dos, Venner C H, Santana L D and Ferrer E 2025 An empirical wall-pressure spectrum model for aeroacoustic predictions based on symbolic regression (arXiv:2501.08134)
[65] Book L G and Flanagan E É 2011 Astrometric effects of a stochastic gravitational wave background *Phys. Rev. D* **83** 024024
[66] Boyle L A and Steinhardt P J 2008 Probing the early universe with inflationary gravitational waves *Phys. Rev. D* **77** 063504
[67] Braglia M, Hazra D K, Sriramkumar L and Finelli F 2020 Generating primordial features at large scales in two field models of inflation *J. Cosmol. Astropart. Phys.* JCAP08(2020)025
[68] Brisken W F, Macquart J-P, Gao J J, Rickett B J, Coles W A, Deller A T, Tingay S J and West C J 2010 100 μas resolution VLBI imaging of anisotropic interstellar scattering toward pulsar B0834+06 *Astrophys. J.* **708** 232–43
[69] Brook P R, Karastergiou A and Johnston S 2019 Linking long- and short-term emission variability in pulsars *Mon. Not. R. Astron. Soc.* **488** 5702–12
[70] Brümmer F, Ferrante G and Frigerio M 2024 Hybrid inflation and gravitational waves from accidentally light scalars *Phys. Rev. D* **110** 103506
[71] Buckley M R, Du P, Fernandez N and Weikert M J 2024 Dark radiation isocurvature from cosmological phase transitions *J. Cosmol. Astropart. Phys.* JCAP07(2024)031
[72] Bullock J S and Boylan-Kolchin M 2017 Small-scale challenges to the ΛCDM paradigm *Annu. Rev. Astron. Astrophys.* **55** 343–87
[73] Bunji N, Fornal B and Garcia K 2024 Shedding light on dark sectors with gravitational waves *Phys. Rev. D* **110** 075030
[74] Burgay M *et al* 2003 An increased estimate of the merger rate of double neutron stars from observations of a highly relativistic system *Nature* **426** 531–3
[75] Burke-Spolaor S *et al* 2019 The astrophysics of nanohertz gravitational waves *Astron. Astrophys. Rev.* **27** 5
[76] Byrnes C T, Hindmarsh M, Young S and Hawkins M R S 2018 Primordial black holes with an accurate QCD equation of state *J. Cosmol. Astropart. Phys.* JCAP08(2018)041
[77] Caballero R N *et al* 2018 Studying the Solar System with the International Pulsar Timing Array *Mon. Not. R. Astron. Soc.* **481** 5501–16
[78] Callister T, Jenks L, Holz D E and Yunes N 2025 New probe of gravitational parity violation through nonobservation of the stochastic gravitational-wave background *Phys. Rev. D* **111** 044041
[79] Camilo F, Lorimer D R, Freire P, Lyne A G and Manchester R N 2000 Observations of 20 millisecond pulsars in 47 Tucanae at 20 centimeters *Astrophys. J.* **535** 975–90

[80] Caprini C and Durrer R 2006 Gravitational waves from stochastic relativistic sources: Primordial turbulence and magnetic fields *Phys. Rev. D* **74** 063521
[81] Caprini C, Durrer R and Servant G 2008 Gravitational wave generation from bubble collisions in first-order phase transitions: an analytic approach *Phys. Rev. D* **77** 124015
[82] Caprini C, Durrer R and Siemens X 2010 Detection of gravitational waves from the QCD phase transition with pulsar timing arrays *Phys. Rev. D* **82** 063511
[83] Caprini C and Figueroa D G 2018 Cosmological backgrounds of gravitational waves *Class. Quantum Grav.* **35** 163001
[84] Caprini C *et al* 2020 Detecting gravitational waves from cosmological phase transitions with LISA: an update *J. Cosmol. Astropart. Phys.* JCAP03(2020)024
[85] Caprini C *et al* 2016 Science with the space-based interferometer eLISA. II: gravitational waves from cosmological phase transitions *J. Cosmol. Astropart. Phys.* JCAP04(2016)001
[86] Carr B, Kühnel F and Sandstad M 2016 Primordial black holes as dark matter *Phys. Rev. D* **94** 083504
[87] Cecchini C, Franciolini G and Pieroni M 2025 Forecasting constraints on scalar-induced gravitational waves with future pulsar timing array observations *Phys. Rev. D* **111** 123536
[88] Chalumeau A *et al* 2022 Noise analysis in the European Pulsar Timing Array data release 2 and its implications on the gravitational-wave background search *Mon. Not. R. Astron. Soc.* **509** 5538–58
[89] Chamel N and Haensel P 2008 Physics of neutron star crusts *Living Rev. Relativ.* **11** 10
[90] Champion D J *et al* 2010 Measuring the mass of Solar System planets using pulsar timing *Astrophys. J. Suppl. Lett.* **720** L201–5
[91] Chen N, Di Matteo T, Zhou Y, Kelley L Z, Blecha L, Ni Y, Bird S, Yang Y and Croft R 2025 The gravitational wave background from massive black holes in the ASTRID simulation *ApJ* **991** L19
[92] Chen P-B and Gao T-J 2025 Gravitational waves and primordial black holes from the T-model inflation with Gauss-Bonnet correction (arXiv:2502.01024)
[93] Chen S *et al* 2021 Common-red-signal analysis with 24-yr high-precision timing of the European Pulsar Timing Array: inferences in the stochastic gravitational-wave background search *Mon. Not. R. Astron. Soc.* **508** 4970–93
[94] Chen S, Sesana A and Conselice C J 2019 Constraining astrophysical observables of galaxy and supermassive black hole binary mergers using pulsar timing arrays *Mon. Not. R. Astron. Soc.* **488** 401–18
[95] Chen S, Sesana A and Del Pozzo W 2017 Efficient computation of the gravitational wave spectrum emitted by eccentric massive black hole binaries in stellar environments *Mon. Not. R. Astron. Soc.* **470** 1738–49
[96] Chen S, Middleton H, Sesana A, Del Pozzo W and Vecchio A 2017 Probing the assembly history and dynamical evolution of massive black hole binaries with pulsar timing arrays *Mon. Not. R. Astron. Soc.* **468** 404–17
[97] Cheng H and Visinelli L 2024 Future targets for light gauge bosons from cosmic strings *Phys. Dark Universe* **46** 101667
[98] Chitose A, Ibe M, Neda S and Shirai S 2024 Gravitational waves from metastable cosmic strings in supersymmetric new inflation model *JCAP* **2025** 010
[99] Choudhury S and Sami M 2025 Large fluctuations and primordial black holes *Phys. Res.* **1103** 1–276
[100] Coles W, Hobbs G, Champion D J, Manchester R N and Verbiest J P W 2011 Pulsar timing analysis in the presence of correlated noise *Mon. Not. R. Astron. Soc.* **418** 561–70
[101] Cooper A J and Wadiasingh Z 2024 Magnetar radio emission beyond the death line *Mon. Not. R. Astron. Soc.* **533** 2133
[102] Corbin V and Cornish N J 2010 Pulsar timing array observations of massive black hole binaries (arXiv:1008.1782)
[103] Cordes J M, Pidwerbetsky A and Lovelace R V E 1986 Refractive and diffractive scattering in the interstellar medium *Astrophys. J.* **310** 737
[104] Cordes J M, Shannon R M and Stinebring D R 2016 Frequency-dependent dispersion measures and implications for pulsar timing *Astrophys. J.* **817** 16
[105] Cordes J M, Weisberg J M and Boriakoff V 1985 Small-scale electron density turbulence in the interstellar medium *Astrophys. J.* **288** 221–47

[106] Cordes J M, Wasserman I, Hessels J W T, Lazio T J W, Chatterjee S and Wharton R S 2017 Lensing of fast radio bursts by plasma structures in host galaxies *Astrophys. J.* **842** 35
[107] Cordes J M, Wolszczan A, Dewey R J, Blaskiewicz M and Stinebring D R 1990 Timing and scintillations of the millisecond pulsar 1937+214 *Astrophys. J.* **349** 245
[108] Correia J R C C C, Martins C J A P and Pimenta F C N Q 2024 Evolution of current-carrying string networks *Phys. Lett. B* **855** 138788
[109] Costa F, Zink J H, Lucente M, Pascoli S and Rosauro-Alcaraz S 2025 Supercooled dark scalar phase transitions explanation of NANOGrav data *Phys. Lett. B* **868** 139634
[110] Cromartie H T *et al* 2020 Relativistic Shapiro delay measurements of an extremely massive millisecond pulsar *Nat. Astron.* **4** 72–76
[111] Curyło M and Bulik T 2022 Predictions for LISA and PTA based on SHARK galaxy simulations *Astron. Astrophys.* **660** A68
[112] Damour T 1990 On the time variation of the gravitational constant *New and Exotic Phenomena* ed O Fackler and J Tran Thanh Van (Ed. Frontieres) p 285
[113] Damour T and Vilenkin A 2005 Gravitational radiation from cosmic (super)strings: Bursts, stochastic background and observational windows *Phys. Rev. D* **71** 063510
[114] Damour T and Vilenkin A 2001 Gravitational wave bursts from cusps and kinks on cosmic strings *Phys. Rev. D* **64** 064008
[115] Danieli V and De Felice A 2025 $f(T)$ gravity: background dependence and propagating degrees of freedom *Phys. Rev. D* **111** 104023
[116] Davari M, Allahyari A and Khosravi S 2024 Testing no slip model with pulsar timing arrays: NANOGrav and IPTA *J. Cosmol. Astropart. Phys.* JCAP12(2024)045
[117] De K and Gupta Y 2016 A real-time coherent dedispersion pipeline for the giant metrewave radio telescope *Exp. Astron.* **41** 67–93
[118] Demorest P B *et al* 2013 Limits on the stochastic gravitational wave background from the North American Nanohertz Observatory for gravitational waves *Astrophys. J.* **762** 94
[119] Desvignes G *et al* 2016 High-precision timing of 42 millisecond pulsars with the European Pulsar Timing Array *Mon. Not. R. Astron. Soc.* **458** 3341–80
[120] Detweiler S 1979 Pulsar timing measurements and the search for gravitational waves *Astrophys. J.* **234** 1100–4
[121] Di H and Gong Y 2018 Primordial black holes and second order gravitational waves from ultra-slow-roll inflation *J. Cosmol. Astropart. Phys.* JCAP07(2018)007
[122] Domènech G and Ganz A 2025 Enhanced induced gravitational waves in Horndeski gravity *J. Cosmol. Astropart. Phys.* JCAP01(2025)020
[123] Donner J Y *et al* 2020 Dispersion measure variability for 36 millisecond pulsars at 150 MHz with LOFAR *Astron. Astrophys.* **644** A153
[124] Dorlis P, Mavromatos N E and Vlachos S-N 2025 Quantum-ordering ambiguities in weak Chern–Simons 4D gravity and metastability of the condensate-induced inflation *Universe* **11** 15
[125] Doroshenko V, Suleimanov V, Pühlhofer G and Santangelo A 2022 A strangely light neutron star within a supernova remnant *Nat. Astron.* **6** 1444–51
[126] Draine B T 2011 *Physics of the Interstellar and Intergalactic Medium* (Princeton University Press)
[127] Drake F D and Craft H D 1968 Second periodic pulsation in pulsars *Nature* **220** 231–5
[128] Dror J A, Ramani H, Trickle T and Zurek K M 2019 Pulsar timing probes of primordial black holes and subhalos *Phys. Rev. D* **100** 023003
[129] Edwards R T, Hobbs G B and Manchester R N 2006 TEMPO2, a new pulsar timing package—II. The timing model and precision estimates *Mon. Not. R. Astron. Soc.* **372** 1549–74
[130] El Bourakadi K, Chakir H and Khlopov M Y 2024 Leptogenesis effects on the gravitational waves background: interpreting the NANOGrav measurements and JWST constraints on primordial black holes *J. Cosmol. Astropart. Phys.* JCAP07(2024)018
[131] Ellis J A, Siemens X and Creighton J D E 2012 Optimal strategies for continuous gravitational wave detection in pulsar timing arrays *Astrophys. J.* **756** 175
[132] Ellis J, Lewicki M and No J M 2019 On the maximal strength of a first-order electroweak phase transition and its gravitational wave signal *J. Cosmol. Astropart. Phys.* JCAP04(2019)003
[133] Ellis J, Lewicki M, No J M and Vaskonen V 2019 Gravitational wave energy budget in strongly supercooled phase transitions *J. Cosmol. Astropart. Phys.* JCAP06(2019)024
[134] Ellis J and van Haasteren R 2019 *PTMCMCSampler: Parallel Tempering Mcmc Sampler Package Written in Python* (Astrophysics Source Code Library)

[135] Ellis J A, Vallisneri M, Taylor S R and Baker P T 2019 *ENTERPRISE: Enhanced Numerical Toolbox Enabling a Robust Pulsar Inference Suite* (Astrophysics Source Code Library)
[136] Ellis J A, Vallisneri M, Taylor S R and Baker P T 2020 *ENTERPRISE: Enhanced Numerical Toolbox Enabling a Robust Pulsar Inference Suite* (Zenodo) (https://doi.org/10.5281/zenodo.4059815)
[137] Elor G, Houtz R, Ipek S and Ulloa M 2024 The standard model CP violation is enough (arXiv:2408.12647)
[138] Enoki M and Nagashima M 2007 The effect of orbital eccentricity on gravitational wave background radiation from supermassive black hole binaries *Prog. Theor. Phys.* **117** 241–56
[139] Antoniadis J *et al* (EPTA Collaboration) 2023 The second data release from the European Pulsar Timing Array. I. The dataset and timing analysis *Astron. Astrophys.* **678** A48
[140] Antoniadis J *et al* (EPTA Collaboration and InPTA Collaboration) 2023 The second data release from the European Pulsar Timing Array. II. Customised pulsar noise models for spatially correlated gravitational waves *Astron. Astrophys.* **678** A49
[141] Antoniadis J *et al* (EPTA Collaboration and InPTA Collaboration) 2023 The second data release from the European Pulsar Timing Array. III. Search for gravitational wave signals *Astron. Astrophys.* **678** A50
[142] Antoniadis J *et al* (EPTA Collaboration and InPTA Collaboration) 2024 The second data release from the European Pulsar Timing Array. IV. Implications for massive black holes, dark matter and the early universe *Astron. Astrophys.* **685** A94
[143] Antoniadis J *et al* (EPTA Collaboration and InPTA Collaboration) 2024 The second data release from the European Pulsar Timing Array. V. Search for continuous gravitational wave signals *Astron. Astrophys.* **690** A118
[144] Espinosa J R, Konstandin T, No J M and Servant G 2010 Energy budget of cosmological first-order phase transitions *J. Cosmol. Astropart. Phys.* JCAP06(2010)028
[145] Fabbri R and Pollock M D 1983 The effect of primordially produced gravitons upon the anisotropy of the cosmological microwave background radiation *Phys. Lett. B* **125** 445–8
[146] Falxa M *et al* 2024 Modeling nonstationary noise in pulsar timing array data analysis *Phys. Rev. D* **109** 123010
[147] Faulkner A J *et al* 2005 PSR J1756-2251: a new relativistic double neutron star system *Astrophys. J. Suppl. Lett.* **618** L119–22
[148] Faulkner A J *et al* 2004 The Parkes Multibeam Pulsar Survey—V. Finding binary and millisecond pulsars *Mon. Not. R. Astron. Soc.* **355** 147–58
[149] Feroz F, Hobson M P and Bridges M 2009 MultiNest: an efficient and robust Bayesian inference tool for cosmology and particle physics *Mon. Not. R. Astron. Soc.* **398** 1601–14
[150] Ferranti I *et al* 2025 Impact of the observation frequency coverage on the significance of a gravitational wave background detection in pulsar timing array data *Astron. Astrophys.* **694** A38
[151] Fienga A, Deram P, Viswanathan V, Di Ruscio A, Bernus L, Durante D, Gastineau M and Laskar J 2019 INPOP19a planetary ephemerides *Notes Scientifiques et Techniques de l'Institut de Mecanique Celeste* vol 109 (Institut de Mécanique Céleste et de Calcul des Éphémérides) (available at: https://ui.adsabs.harvard.edu/abs/2019NSTIM.109.....F)
[152] Fonseca E *et al* 2016 The NANOGrav nine-year data set: mass and geometric measurements of binary millisecond pulsars *Astrophys. J.* **832** 167
[153] Foster G, Karastergiou A, Paulin R, Carozzi T D, Johnston S and van Straten W 2015 Intrinsic instrumental polarization and high-precision pulsar timing *Mon. Not. R. Astron. Soc.* **453** 1489–502
[154] Foster R S and Backer D C 1990 Constructing a pulsar timing array *Astrophys. J.* **361** 300
[155] Franciolini G, Racco D and Rompineve F 2024 Footprints of the QCD crossover on cosmological gravitational waves at pulsar timing arrays *Phys. Rev. Lett.* **132** 081001
[156] Freese K, Litsa A and Winkler M W 2024 Gravitational wave spectrum of chain inflation *Phys. Rev. D* **110** 103526
[157] Fu B, Ghoshal A, King S F and Rahat M H 2024 Type-I two-Higgs-doublet model and gravitational waves from domain walls bounded by strings *J. High Energy Phys.* JHEP08(2024)237
[158] Fujita T, Namba R, Tada Y, Takeda N and Tashiro H 2015 Consistent generation of magnetic fields in axion inflation models *J. Cosmol. Astropart. Phys.* JCAP05(2015)054
[159] Fumagalli G, Shaifullah G and Sesana A 2025 The impact of outliers on pulsar timing array signals *Astronomy & Astrophysics* **697** A25

[160] Fuskeland U *et al* 2023 Tensor-to-scalar ratio forecasts for extended LiteBIRD frequency configurations *Astron. Astrophys.* **676** A42
[161] Ghosh T, Ghoshal A, Guo H -K, Hajkarim F, King S F, Sinha K, Wang X and White G 2024 Did we hear the sound of the universe boiling? Analysis using the full fluid velocity profiles and NANOGrav 15-year data *J. Cosmol. Astropart. Phys.* JCAP05(2024)100
[162] Giovannini M 1998 Gravitational wave constraints on post-inflationary phases stiffer than radiation *Phys. Rev. D* **58** 083504
[163] Gold T 1968 Rotating neutron stars as the origin of the pulsating radio sources *Nature* **218** 731–2
[164] Goldstein S J and James J T 1969 Accurate dispersions for thirteen pulsars *Astrophys. J. Suppl. Lett.* **158** L179
[165] Goncharov B *et al* 2022 Consistency of the Parkes Pulsar Timing Array signal with a nanohertz gravitational-wave background *Astrophys. J. Suppl. Lett.* **932** L22
[166] Goncharov B *et al* 2021 On the evidence for a common-spectrum process in the search for the nanohertz gravitational-wave background with the Parkes Pulsar Timing Array *Astrophys. J. Suppl. Lett.* **917** L19
[167] Graham A W and Scott N 2013 The M_{BH}-$L_{spheroid}$ relation at high and low masses, the quadratic growth of black holes and intermediate-mass black hole candidates *Astrophys. J.* **764** 151
[168] Graham P W, Mardon J and Rajendran S 2016 Vector dark matter from inflationary fluctuations *Phys. Rev. D* **93** 103520
[169] Grishchuk L, Kulagin V, Rudenko V and Serdobolski A 2005 Geophysical studies with laser-beam detectors of gravitational waves *Class. Quantum Grav.* **22** 245–69
[170] Grishchuk L P 1975 Amplification of gravitational waves in an isotropic universe *Sov. J. Exp. Theor. Phys.* **40** 409 (available at: https://ui.adsabs.harvard.edu/abs/1975JETP..40..409G)
[171] Grishchuk L P 1974 Amplification of gravitational waves in an isotropic universe *Zh. Eksp. Teor. Fiz.* **67** 825–38 (available at: https://ui.adsabs.harvard.edu/abs/1974ZhETF..67..825G)
[172] Grojean C and Servant G 2007 Gravitational waves from phase transitions at the electroweak scale and beyond *Phys. Rev. D* **75** 043507
[173] Grunthal K *et al* 2025 The MeerKAT Pulsar Timing Array: maps of the gravitational wave sky with the 4.5-yr data release *Mon. Not. R. Astron. Soc.* **536** 1501–17
[174] Guo Y J, Li G Y, Lee K J and Caballero R N 2019 Studying the Solar System dynamics using pulsar timing arrays and the LINIMOSS dynamical model *Mon. Not. R. Astron. Soc.* **489** 5573–81
[175] Haasteren R *et al* 2011 Placing limits on the stochastic gravitational-wave background using European Pulsar Timing Array data *Mon. Not. R. Astron. Soc.* **414** 3117–28
[176] Handley W J, Hobson M P and Lasenby A N 2015 polychord: next-generation nested sampling *Mon. Not. R. Astron. Soc.* **453** 4385–99
[177] Hankins T H, Kern J S, Weatherall J C and Eilek J A 2003 Nanosecond radio bursts from strong plasma turbulence in the crab pulsar *Nature* **422** 141
[178] Harding A K, Muslimov A G and Zhang B 2002 Regimes of pulsar pair formation and particle energetics *Astrophys. J.* **576** 366
[179] Hazboun J S, Romano J D and Smith T L 2019 Realistic sensitivity curves for pulsar timing arrays *Phys. Rev. D* **100** 104028
[180] Hazboun J S *et al* 2022 Bayesian solar wind modeling with pulsar timing arrays *Astrophys. J.* **929** 39
[181] Hazboun J S, Simon J, Siemens X and Romano J D 2020 Model dependence of Bayesian gravitational-wave background statistics for pulsar timing arrays *Astrophys. J. Suppl. Lett.* **905** L6
[182] Hebel J and Lam M 2022 Timing Jitter from broadband radio observations of millisecond pulsars *American Astronomical Society Meeting (American Astronomical Society Meeting Abstracts)* vol 240 p 102.03 (available at: https://ui.adsabs.harvard.edu/abs/2022AAS...24010203H)
[183] Hee S, Handley W J, Hobson M P and Lasenby A N 2016 Bayesian model selection without evidences: application to the dark energy equation-of-state *Mon. Not. R. Astron. Soc.* **455** 2461–73
[184] Hellings R W and Downs G S 1983 Upper limits on the isotropic gravitational radiation background from pulsar timing analysis *Proc. 10th Int. Conf. on General Relativity and Gravitation* vol 1 p 963 (available at: https://ui.adsabs.harvard.edu/abs/1983grg1.conf..963H)
[185] Hemberger D A and Stinebring D R 2008 Time Variability of Interstellar Scattering and Improvements to Pulsar Timing *Astrophys. J. Suppl. Lett.* **674** L37

[186] Hessels J W T, Ransom S M, Stairs I H, Freire P C C, Kaspi V M and Camilo F 2006 A radio pulsar spinning at 716 Hz *Science* **311** 1901–4
[187] Hewish A and Ryle M 1955 The Cambridge radio telescope *Mem. R. Astron. Soc.* **67** 97 (available at: https://ui.adsabs.harvard.edu/abs/1955MmRAS..67...97H)
[188] Hewish A, Bell S J, Pilkington J D H, Scott P F and Collins R A 1968 Observation of a rapidly pulsating radio source *Nature* **217** 709–13
[189] Hindmarsh M, Huber S J, Rummukainen K and Weir D J 2015 Numerical simulations of acoustically generated gravitational waves at a first order phase transition *Phys. Rev. D* **92** 123009
[190] Hiramatsu T, Kawasaki M and Saikawa K 2014 On the estimation of gravitational wave spectrum from cosmic domain walls *J. Cosmol. Astropart. Phys.* JCAP02(2014)031
[191] Hobbs G, Lyne A G and Kramer M 2010 An analysis of the timing irregularities for 366 pulsars *Mon. Not. R. Astron. Soc.* **402** 1027–48
[192] Hobbs G *et al* 2012 Development of a pulsar-based time-scale *Mon. Not. R. Astron. Soc.* **427** 2780–7
[193] Hobbs G *et al* 2010 The International Pulsar Timing Array project: using pulsars as a gravitational wave detector *Class. Quantum Grav.* **27** 084013
[194] Hobbs G B, Edwards R T and Manchester R N 2006 TEMPO2, a new pulsar-timing package—I. An overview *Mon. Not. R. Astron. Soc.* **369** 655–72
[195] Hobbs G *et al* 2020 An ultra-wide bandwidth (704 to 4 032 MHz) receiver for the Parkes radio telescope *Publ. Astron. Soc. Aust.* **37** e012
[196] Hogan C J 1986 Gravitational radiation from cosmological phase transitions *Mon. Not. R. Astron. Soc.* **218** 629–36
[197] Hogan C 1984 Cosmology: Cosmic strings and galaxies *Nature* **310** 365–6
[198] Horndeski G W 1974 Second-order scalar-tensor field equations in a four-dimensional space *Int. J. Theor. Phys.* **10** 363–84
[199] Hotan A W, van Straten W and Manchester R N 2004 PSRCHIVE and PSRFITS: an open approach to radio pulsar data storage and analysis *Publ. Astron. Soc. Aust.* **21** 302–9
[200] Hu Y, Wang P -P, Tan Y-J and Shao C -G 2022 Full analytic expression of overlap reduction function for gravitational wave background with pulsar timing arrays *Phys. Rev. D* **106** 024005
[201] Huber S J and Konstandin T 2008 Gravitational wave production by collisions: more bubbles *J. Cosmol. Astropart. Phys.* JCAP09(2008)022
[202] Huguenin G R, Taylor J H and Troland T H 1970 The radio emission from pulsar MP 0031-07 *Astrophys. J.* **162** 727
[203] Inomata K, Kohri K, Nakama T and Terada T 2019 Enhancement of gravitational waves induced by scalar perturbations due to a sudden transition from an early matter era to the radiation era *Phys. Rev. D* **100** 043532
[204] Inui R, Jaraba S, Kuroyanagi S and Yokoyama S 2024 Constraints on non-Gaussian primordial curvature perturbation from the LIGO-Virgo-KAGRA third observing run *J. Cosmol. Astropart. Phys.* JCAP05(2024)082
[205] Iraci F *et al* 2024 Pulsar timing methods for evaluating dispersion measure time series *Astron. Astrophys.* **692** A170
[206] Iso S, Serpico P D and Shimada K 2017 QCD-electroweak first-order phase transition in a supercooled universe *Phys. Rev. Lett.* **119** 141301
[207] Issautier K, Skoug R M, Gosling J T, Gary S P and McComas D J 2001 Solar wind plasma parameters on Ulysses: detailed comparison between the URAP and SWOOPS experiments *J. Geophys. Res.* **106** 15665–76
[208] Izquierdo-Villalba D, Sesana A, Bonoli S and Colpi M 2022 Massive black hole evolution models confronting the n-Hz amplitude of the stochastic gravitational wave background *Mon. Not. R. Astron. Soc.* **509** 3488–503
[209] Jenet F *et al* 2009 The North American nanohertz observatory for gravitational waves (arXiv:0909.1058)
[210] Jenet F A, Lommen A, Larson S L and Wen L 2004 Constraining the properties of supermassive black hole systems using pulsar timing: application to 3C 66B *Astrophys. J.* **606** 799–803
[211] Jennings R J *et al* 2024 An unusual pulse shape change event in PSR J1713+0747 observed with the Green Bank Telescope and CHIME *Astrophys. J.* **964** 179
[212] Jinno R and Kume J 2024 Gravitational effects on fluid dynamics in cosmological first-order phase transitions (arXiv:2408.10770)

[213] Jinno R and Kume J 2025 Gravitational effects on fluid dynamics in cosmological first-order phase transitions *J. Cosmol. Astropart. Phys.* JCAP02(2025)057
[214] Johnson A D, Vigeland S J, Siemens X and Taylor S R 2022 Gravitational-wave statistics for pulsar timing arrays: examining bias from using a finite number of pulsars *Astrophys. J.* **932** 105
[215] Jones P B 1990 The generation of timing noise by superfluid rotation in pulsars *Mon. Not. R. Astron. Soc.* **246** 364
[216] Junior Iovino A 2025 Cosmic whispers of the early universe: gravitational waves and dark matter from primordial black holes (arXiv:2501.03065)
[217] Kamionkowski M, Kosowsky A and Turner M S 1994 Gravitational radiation from first-order phase transitions *Phys. Rev. D* **49** 2837–51
[218] Kanemura S, Tanaka M and Xie K -P 2024 Primordial black holes from slow phase transitions: a model-building perspective *J. High Energy Phys.* JHEP06(2024)036
[219] Kaplan D E, Mitridate A and Trickle T 2022 Constraining fundamental constant variations from ultralight dark matter with Pulsar Timing Arrays *Phys. Rev. D* **106** 035032
[220] Kaplan D L *et al* 2016 PSR J1024-0719: a millisecond pulsar in an unusual long-period orbit *Astrophys. J.* **826** 86
[221] Karnesis N, Katz M L, Korsakova N, Gair J R and Stergioulas N 2023 Eryn: a multipurpose sampler for Bayesian inference *Mon. Not. R. Astron. Soc.* **526** 4814–30
[222] Kaspi V M and Beloborodov A M 2017 Magnetars *Annu. Rev. Astron. Astrophys.* **55** 261
[223] Kazbegi A Z, Machabeli G Z and Melikidze G I 1991 Radio emission of pulsars as the result of cyclotron instability *Mon. Not. R. Astron. Soc.* **253** 377
[224] Kelley L Z, Blecha L, Hernquist L, Sesana A and Taylor S R 2017 The gravitational wave background from massive black hole binaries in Illustris: spectral features and time to detection with Pulsar Timing Arrays *Mon. Not. R. Astron. Soc.* **471** 4508–26
[225] Kerr M, Parthasarathy A and Cromartie T 2023 Upgrading the gamma-ray pulsar timing array: data release 2 *Proc. Sci.* **444** 1595
[226] Kerr M *et al* 2020 The Parkes Pulsar Timing Array project: second data release *Publ. Astron. Soc. Aust.* **37** e020
[227] Khmelnitsky A and Rubakov V 2014 Pulsar timing signal from ultralight scalar dark matter *J. Cosmol. Astropart. Phys.* JCAP02(2014)019
[228] Kibble T W B 1976 Topology of cosmic domains and strings *J. Phys. A: Math. Gen.* **9** 1387–98
[229] Kocsis B and Sesana A 2011 Gas-driven massive black hole binaries: signatures in the nHz gravitational wave background *Mon. Not. R. Astron. Soc.* **411** 1467–79
[230] Kormendy J and Ho L C 2013 Coevolution (or not) of supermassive black holes and host galaxies *Annu. Rev. Astron. Astrophys.* **51** 511–653
[231] Kosowsky A 1996 Cosmic microwave background polarization *Ann. Phys., NY* **246** 49–85
[232] Kosowsky A, Turner M S and Watkins R 1992 Gravitational radiation from colliding vacuum bubbles *Phys. Rev. D* **45** 4514–35
[233] Kosowsky A, Turner M S and Watkins R 1992 Gravitational waves from first-order cosmological phase transitions *Phys. Rev. Lett.* **69** 2026–9
[234] Kramer M, Lyne A G, O'Brien J T, Jordan C A and Lorimer D R 2006 A periodically active pulsar giving insight into magnetospheric physics *Science* **312** 549–51
[235] Kramer M and Champion D J 2013 The European Pulsar Timing Array and the Large European Array for Pulsars *Class. Quantum Grav.* **30** 224009
[236] Kramer M, Liu K, Desvignes G, Karuppusamy R and Stappers B W 2024 Quasi-periodic subpulse structure as a unifying feature for radio-emitting neutron stars *Nat. Astron.* **8** 230–40
[237] Kramer M, Xilouris K M, Lorimer D R, Doroshenko O, Jessner A, Wielebinski R, Wolszczan A and Camilo F 1998 The characteristics of millisecond pulsar emission. I. Spectra, pulse shapes and the beaming fraction *Astrophys. J.* **501** 270–85
[238] Krishnakumar M A *et al* 2021 High precision measurements of interstellar dispersion measure with the upgraded GMRT *Astron. Astrophys.* **651** A5
[239] Kuroyanagi S, Takahashi T and Yokoyama S 2021 Blue-tilted inflationary tensor spectrum and reheating in the light of NANOGrav results *J. Cosmol. Astropart. Phys.* JCAP01(2021)071
[240] Lam M T and Hazboun J S 2021 Precision timing of PSR J0437-4715 with the IAR observatory and implications for low-frequency gravitational wave source sensitivity *Astrophys. J.* **911** 137
[241] Lam M T, McLaughlin M A, Cordes J M, Chatterjee S and Lazio T J W 2018 Optimal frequency ranges for submicrosecond precision pulsar timing *Astrophys. J.* **861** 12

[242] Lam M T, Cordes J M, Chatterjee S, Jones M L, McLaughlin M A and Armstrong J W 2016 Systematic and stochastic variations in pulsar dispersion measures *Astrophys. J.* **821** 66
[243] Lam M T 2019 Optimizing pulsar timing array observational cadences for sensitivity to low-frequency gravitational wave sources *American Astronomical Society Meeting Abstracts (American Astronomical Society Meeting Abstracts)* vol 233 p 107.01 (available at: https://ui.adsabs.harvard.edu/abs/2019AAS...23310701L)
[244] Larsen B *et al* 2024 The NANOGrav 15 yr data set: chromatic Gaussian process noise models for six pulsars *Astrophys. J.* **972** 49
[245] Lasky P D *et al* 2016 Gravitational-wave cosmology across 29 decades in frequency *Phys. Rev. X* **6** 011035
[246] Lazarides G, Maji R and Shafi Q 2024 Quantum tunneling in the early universe: stable magnetic monopoles from metastable cosmic strings *J. Cosmol. Astropart. Phys.* JCAP05(2024)128
[247] Lazarus P, Karuppusamy R, Graikou E, Caballero R N, Champion D J, Lee K J, Verbiest J P W and Kramer M 2016 Prospects for high-precision pulsar timing with the new Effelsberg PSRIX backend *Mon. Not. R. Astron. Soc.* **458** 868–80
[248] Lee K J 2016 Prospects of gravitational wave detection using pulsar timing array for Chinese future telescopes *Frontiers in Radio Astronomy and FAST Early Sciences Symp. 2015 (Astronomical Society of the Pacific Conf. Series)* vol 502, ed L Qain and D Li p 19 (available at: https://ui.adsabs.harvard.edu/abs/2016ASPC..502...19L)
[249] Lee V S H, Mitridate A, Trickle T and Zurek K M 2021 Probing small-scale power spectra with pulsar timing arrays *J. High Energy Phys.* JHEP06(2021)028
[250] Lemke A -M, Mitridate A and Gersbach K A 2024 Detecting gravitational wave anisotropies from supermassive black hole binaries *Phys. Rev. D* **111** 063068
[251] Lentati L, Hobson M P and Alexander P 2014 Bayesian estimation of non-Gaussianity in pulsar timing analysis *Mon. Not. R. Astron. Soc.* **444** 3863–78
[252] Lentati L *et al* 2016 From spin noise to systematics: stochastic processes in the first International Pulsar Timing Array data release *Mon. Not. R. Astron. Soc.* **458** 2161–87
[253] Lentati L, Alexander P, Hobson M P, Feroz F, van Haasteren R, Lee K J and Shannon R M 2014 TEMPONEST: a Bayesian approach to pulsar timing analysis *Mon. Not. R. Astron. Soc.* **437** 3004–23
[254] Lentati L, Alexander P and Hobson M P 2013 How to take the interstellar weather with you in pulsar timing analysis (arXiv:1312.2403)
[255] Liang Q, Lin M -X, Trodden M and Wong S S C 2024 Probing parity violation in the stochastic gravitational wave background with astrometry *Phys. Rev. D* **109** 083028
[256] Liddle A R 2009 Statistical methods for cosmological parameter selection and estimation *Annu. Rev. Nucl. Part. Sci.* **59** 95–114
[257] Lifshitz E M 1946 On the gravitational stability of the expanding universe *Zh. Eksp. Teor. Fiz.* **16** 587–602 (available at: https://ui.adsabs.harvard.edu/abs/1946ZhETF..16..587L)
[258] Lin F X, Main R A, Verbiest J P W, Kramer M and Shaifullah G 2021 Discovery and modelling of broad-scale plasma lensing in black-widow pulsar J2051-0827 *Mon. Not. R. Astron. Soc.* **506** 2824–35
[259] Linde A D 1983 Decay of the false vacuum at finite temperature *Nucl. Phys. B* **216** 421
Linde A D 1983 *Nucl. Phys. B* **223** 544 (erratum)
[260] Liu J, Alexander S and Marciano A 2025 Birefringence in fermion-attenuated gravitational wave power spectrum (arXiv:2501.08240)
[261] Liu T, Lou X and Ren J 2023 Pulsar polarization arrays *Phys. Rev. Lett.* **130** 121401
[262] Lommen A N 2015 Pulsar timing arrays: the promise of gravitational wave detection *Rep. Prog. Phys.* **78** 124901
[263] Lorimer D R 2004 The galactic population and birth rate of radio pulsars *Young Neutron Stars and Their Environments (IAU Symp.)* vol 218, ed F Camilo and B M Gaensler p 105 (available at: https://ui.adsabs.harvard.edu/abs/2004IAUS..218..105L)
[264] Lorimer D R 2005 Binary and millisecond pulsars *Living Rev. Relativ.* **8** 7
[265] Lu J, Deng J and Zhang T 2025 Beyond the final layer: hierarchical query fusion transformer with agent-interpolation initialization for 3D instance segmentation (arXiv:2502.04139)
[266] Luo J *et al* 2021 PINT: a modern software package for pulsar timing *Astrophys. J.* **911** 45
[267] Lyne A and Graham-Smith F 2012 *Pulsar Astronomy* (Cambridge University Press)
[268] Lyne A, Hobbs G, Kramer M, Stairs I and Stappers B 2010 Switched magnetospheric regulation of pulsar spin-down *Science* **329** 408

[269] Maan Y, van Leeuwen J and Vohl D 2021 Fourier domain excision of periodic radio frequency interference *Astron. Astrophys.* **650** A80
[270] Madison D R *et al* 2019 The NANOGrav 11 yr data set: solar wind sounding through pulsar timing *Astrophys. J.* **872** 150
[271] Mahajan N, van Kerkwijk M H, Main R and Pen U -L 2018 Mode changing and giant pulses in the millisecond pulsar PSR B1957+20 *Astrophys. J. Suppl. Lett.* **867** L2
[272] Manchester R N 2013 The International Pulsar Timing Array *Class. Quantum Grav.* **30** 224010
[273] Manchester R N and Taylor J H 1972 Parameters of 61 pulsars *Astrophys. Lett.* **10** 67 (available at: https://ui.adsabs.harvard.edu/abs/1972ApL....10...67M)
[274] Manchester R N, Hobbs G B, Teoh A and Hobbs M 2005 The Australia telescope national facility pulsar catalogue *Astron. J.* **129** 1993–2006
[275] Manchester R N *et al* 2013 The Parkes Pulsar Timing Array Project *Publ. Astron. Soc. Aust.* **30** e017
[276] Manchester R N and Taylor J H 1977 *Pulsars* (W. H. Freeman and Company)
[277] Marcote B, Maan Y, Paragi Z and Keimpema A 2019 Probing the origin of the off-pulse emission from the pulsars B0525+21 and B2045-16 *Astron. Astrophys.* **627** L2
[278] Marsch E 2006 Kinetic physics of the solar corona and solar wind *Living Rev. Sol. Phys.* **3** 1
[279] Matarrese S, Mollerach S and Bruni M 1998 Relativistic second-order perturbations of the Einstein-de Sitter universe *Phys. Rev. D* **58** 043504
[280] Matt C, Gültekin K and Simon J 2023 The impact of black hole scaling relation assumptions on the mass density of black holes *Mon. Not. R. Astron. Soc.* **524** 4403–17
[281] Mazumdar A and White G 2019 Review of cosmic phase transitions: their significance and experimental signatures *Rep. Prog. Phys.* **82** 076901
[282] McConnell N J and Ma C -P 2013 Revisiting the scaling relations of black hole masses and host galaxy properties *Astrophys. J.* **764** 184
[283] McLaughlin M A 2013 The North American nanohertz observatory for gravitational waves *Class. Quantum Grav.* **30** 224008
[284] McLaughlin M A *et al* 2006 Transient radio bursts from rotating neutron stars *Nature* **439** 817–20
[285] McWilliams S T, Ostriker J P and Pretorius F 2014 Gravitational waves and stalled satellites from massive galaxy mergers at $z \leqslant 1$ *Astrophys. J.* **789** 156
[286] Melatos A and Link B 2014 Pulsar timing noise from superfluid turbulence *Mon. Not. R. Astron. Soc.* **437** 21–31
[287] Melikidze G I, Gil J and Pataraya A D 2000 On the generation of coherent radio emission in pulsars *Astrophys. J.* **544** 1081
[288] Melrose D B 1995 Models for coherent pulsar radio emission *J. Astrophys. Astron.* **16** 137
[289] Mereghetti S 2008 The strongest cosmic magnets: soft gamma-ray repeaters and anomalous x-ray pulsars *Astron. Astrophys. Rev.* **15** 225–87
[290] Middleton H, Del Pozzo W, Farr W M, Sesana A and Vecchio A 2016 Astrophysical constraints on massive black hole binary evolution from pulsar timing arrays *Mon. Not. R. Astron. Soc.* **455** L72–L76
[291] Mignani R P 2011 Optical, ultraviolet and infrared observations of isolated neutron stars *Adv. Space Res.* **47** 1281–93
[292] Miles M T, Shannon R M, Bailes M, Reardon D J, Buchner S, Middleton H and Spiewak R 2022 Mode changing in J1909-3744: the most precisely timed pulsar *Mon. Not. R. Astron. Soc.* **510** 5908–15
[293] Miles M T *et al* 2023 The MeerKAT Pulsar Timing Array: first data release *Mon. Not. R. Astron. Soc.* **519** 3976–91
[294] Miles M T *et al* 2025 The MeerKAT Pulsar Timing Array: the first search for gravitational waves with the MeerKAT radio telescope *Mon. Not. R. Astron. Soc.* **536** 1489–500
[295] Miller M C *et al* 2019 PSR J0030+0451 mass and radius from NICER data and implications for the properties of neutron star matter *Astrophys. J. Suppl. Lett.* **887** L24
[296] Miller M C *et al* 2021 The radius of PSR J0740+6620 from NICER and XMM-Newton data *Astrophys. J. Suppl. Lett.* **918** L28
[297] Milosavljević M and Merritt D 2003 The final parsec problem *AIP Conf. Proc.* **686** 201–10
[298] Mirshekari S, Yunes N and Will C M 2012 Constraining Lorentz-violating, modified dispersion relations with gravitational waves *Phys. Rev. D* **85** 024041
[299] Mitra D 2017 Understanding radio emission from pulsars *J. Astrophys. Astron.* **38** 52
[300] Mitridate A and Wright D 2023 *PTArcade* (Zenodo) (https://doi.org/10.5281/zenodo.7876429)

[301] Morello V, Rajwade K M and Stappers B W 2023 *IQRM: IQRM Interference Flagging Algorithm for Radio Pulsar and Transient Searches* (Astrophysics Source Code Library)
[302] Morello V *et al* 2019 The high time resolution universe survey—XIV. Discovery of 23 pulsars through GPU-accelerated reprocessing *Mon. Not. R. Astron. Soc.* **483** 3673–85
[303] Morozova V S, Ahmedov B J and Zanotti O 2012 Magnetar Radio Emission Induced by Twisted Magnetospheres *Mon. Not. R. Astron. Soc.* **419** 2147
[304] Nathan R S, Miles M T, Ashton G, Lasky P D, Thrane E, Reardon D J, Shannon R M and Cameron A D 2023 Improving pulsar-timing solutions through dynamic pulse fitting *Mon. Not. R. Astron. Soc.* **523** 4405–12
[305] Nice D, Demorest P, Stairs I, Manchester R, Taylor J, Peters W, Weisberg J, Irwin A, Wex N, Huang Y 2015 *Tempo: Pulsar Timing Data Analysis* (Astrophysics Source Code Library)
[306] Niikura H *et al* 2019 Microlensing constraints on primordial black holes with Subaru/HSC Andromeda observations *Nat. Astron.* **3** 524–34
[307] Nobleson K *et al* 2022 Low-frequency wideband timing of InPTA pulsars observed with the uGMRT *Mon. Not. R. Astron. Soc.* **512** 1234–43
[308] Oikonomou V K, Tsyba P and Razina O 2024 Red or blue tensor spectrum from GW170817-compatible Einstein-Gauss-Bonnet theory: a detailed analysis *Europhys. Lett.* **145** 49001
[309] Okounkova M, Farr W M, Isi M and Stein L C 2022 Constraining gravitational wave amplitude birefringence and Chern-Simons gravity with GWTC-2 *Phys. Rev. D* **106** 044067
[310] Olausen S A and Kaspi V M 2014 The McGill magnetar catalog *Astrophys. J. Suppl. Ser.* **212** 6
[311] Osłowski S, van Straten W, Bailes M, Jameson A and Hobbs G 2014 Timing, polarimetry and physics of the bright, nearby millisecond pulsar PSR J0437-4715—a single-pulse perspective *Mon. Not. R. Astron. Soc.* **441** 3148–60
[312] Özel F and Freire P 2016 Masses, radii and the equation of state of neutron stars *Annu. Rev. Astron. Astrophys.* **54** 401–40
[313] Pacini F 1967 Energy emission from a neutron star *Nature* **216** 567–8
[314] Pallis C 2025 T-model Higgs inflation and metastable cosmic strings *J. High Energy Phys.* JHEP01(2025)178
[315] Palliyaguru N T, Perera B B P, McLaughlin M A, Osłowski S and Siebert G L 2023 Single-pulse studies of three millisecond pulsars *Mon. Not. R. Astron. Soc.* **520** 2747–56
[316] Park R S, Folkner W M, Williams J G and Boggs D H 2021 The JPL planetary and lunar ephemerides DE440 and DE441 *Astron. J.* **161** 105
[317] Parthasarathy A *et al* 2021 Measurements of pulse jitter and single-pulse variability in millisecond pulsars using MeerKAT *Mon. Not. R. Astron. Soc.* **502** 407–22
[318] Pennucci T T 2019 Frequency-dependent template profiles for high-precision pulsar timing *Astrophys. J.* **871** 34
[319] Perera B B P *et al* 2019 The International Pulsar Timing Array: second data release *Mon. Not. R. Astron. Soc.* **490** 4666–87
[320] Petiteau A, Babak S, Sesana A and de Araújo M 2013 Resolving multiple supermassive black hole binaries with pulsar timing arrays. II. Genetic algorithm implementation *Phys. Rev. D* **87** 064036
[321] Petrova S A 2004 Toward explanation of microstructure in pulsar radio emission *Astron. Astrophys.* **417** L29–L32
[322] Philippov A A, Timokhin A N and Spitkovsky A 2020 Origin of pulsar radio emission in PIC simulations of unsteady pair discharges *Phys. Rev. Lett.* **124** 245101
[323] Phinney E S 2001 A practical theorem on gravitational wave backgrounds (arXiv:astro-ph/0108028)
[324] Phoroutan-Mehr M and Fetherolf T 2025 Probing superheavy dark matter with exoplanets (arXiv:2503.00125)
[325] Pi S 2024 Non-Gaussianities and primordial black holes Primordial Black Holes pp 155–200
[326] Pi S, Sasaki M, Wang A and Wang J 2024 Revisiting the ultraviolet tail of the primordial gravitational wave *Phys. Rev. D* **110** 103529
[327] Pilkington J D H, Hewish A, Bell S J and Cole T W 1968 Observations of some further pulsed radio sources *Nature* **218** 126–9
[328] Akrami Y *et al* (Planck Collaboration) 2020 Planck 2018 results. X. Constraints on inflation *Astron. Astrophys.* **641** A10
[329] Porayko N K *et al* 2025 Searches for signatures of ultralight axion dark matter in polarimetry data of the European Pulsar Timing Array *Phys. Rev. D* **111** 062005

[330] Porayko N K *et al* 2018 Parkes Pulsar Timing Array constraints on ultralight scalar-field dark matter *Phys. Rev. D* **98** 102002
[331] Preskill J, Wise M B, Trivedi S P and Wilczek F 1991 Cosmology and broken discrete symmetry *Nucl. Phys. B* **363** 207–20
[332] Ransom S M *et al* 2014 A millisecond pulsar in a stellar triple system *Nature* **505** 520–4
[333] Ransom S M 2008 Pulsars in Globular Clusters *Dynamical Evolution of Dense Stellar Systems (IAU Symp.)* vol 246, ed E Vesperini M Giersz A Sills pp 291–300
[334] Raveri M and Doux C 2021 Non-Gaussian estimates of tensions in cosmological parameters *Phys. Rev. D* **104** 043504
[335] Ravi V, Wyithe J S B, Shannon R M, Hobbs G and Manchester R N 2014 Binary supermassive black hole environments diminish the gravitational wave signal in the pulsar timing band *Mon. Not. R. Astron. Soc.* **442** 56–68
[336] Ray P S *et al* 2012 Radio searches of Fermi LAT sources and blind search pulsars: the Fermi pulsar search consortium (arXiv:1205.3089)
[337] Reardon D J *et al* 2016 Timing analysis for 20 millisecond pulsars in the Parkes Pulsar Timing Array *Mon. Not. R. Astron. Soc.* **455** 1751–69
[338] Reardon D J *et al* 2023 Search for an isotropic gravitational-wave background with the Parkes Pulsar Timing Array *Astrophys. J. Suppl. Lett.* **951** L6
[339] Reddy S H, Kudale S, Gokhale U, Halagalli I, Raskar N, de K, Gnanaraj S, Ajith Kumar B and Gupta Y 2017 A wideband digital back-end for the upgraded GMRT *J. Astron. Instrum.* **6** 1641011–336
[340] Rickett B J 1990 Radio propagation through the turbulent interstellar plasma *Annu. Rev. Astron. Astrophys.* **28** 561–605
[341] Roebber E 2019 Ephemeris errors and the gravitational-wave signal: harmonic mode coupling in pulsar timing array searches *Astrophys. J.* **876** 55
[342] Rosado P A, Sesana A and Gair J 2015 Expected properties of the first gravitational wave signal detected with pulsar timing arrays *Mon. Not. R. Astron. Soc.* **451** 2417–33
[343] Roshan R and White G 2025 Using gravitational waves to see the first second of the universe *Rev. Mod. Phys.* **97** 015001
[344] Rubakov V A, Sazhin M V and Veryaskin A V 1982 Graviton creation in the inflationary universe and the grand unification scale *Phys. Lett. B* **115** 189–92
[345] Ruderman M A and Sutherland P G 1975 Theory of pulsars: polar caps, sparks and coherent microwave radiation *Astrophys. J.* **196** 51
[346] Sachs R K and Wolfe A M 1967 Perturbations of a cosmological model and angular variations of the microwave background *Astrophys. J.* **147** 73
[347] Salvio A 2024 Pulsar timing arrays and primordial black holes from a supercooled phase transition *Phys. Lett. B* **852** 138639
[348] Sato-Polito G and Kamionkowski M 2022 Pulsar-timing measurement of the circular polarization of the stochastic gravitational-wave background *Phys. Rev. D* **106** 023004
[349] Sato-Polito G, Zaldarriaga M and Quataert E 2024 Where are the supermassive black holes measured by PTAs? *Phys. Rev. D* **110** 063020
[350] Sazhin M V 1978 Opportunities for detecting ultralong gravitational waves *Astron. Zh.* **55** 65 (available at: https://ui.adsabs.harvard.edu/abs/1978AZh....55...65S)
[351] Sesana A 2013 Gravitational wave emission from binary supermassive black holes *Class. Quantum Grav.* **30** 244009
[352] Sesana A 2013 Insights into the astrophysics of supermassive black hole binaries from pulsar timing observations *Class. Quantum Grav.* **30** 224014
[353] Sesana A 2013 Systematic investigation of the expected gravitational wave signal from supermassive black hole binaries in the pulsar timing band *Mon. Not. R. Astron. Soc.* **433** L1–L5
[354] Sesana A, Vecchio A and Volonteri M 2009 Gravitational waves from resolvable massive black hole binary systems and observations with pulsar timing arrays *Mon. Not. R. Astron. Soc.* **394** 2255–65
[355] Sesana A 2010 Self consistent model for the evolution of eccentric massive black hole binaries in stellar environments: implications for gravitational wave observations *Astrophys. J.* **719** 851–64
[356] Sesana A, Haardt F and Madau P 2008 Interaction of massive black hole binaries with their stellar environment. III. Scattering of bound stars *Astrophys. J.* **686** 432–47

[357] Sesana A and Khan F M 2015 Scattering experiments meet N-body—I. A practical recipe for the evolution of massive black hole binaries in stellar environments *Mon. Not. R. Astron. Soc.* **454** L66–L70
[358] Sesana A, Shankar F, Bernardi M and Sheth R K 2016 Selection bias in dynamically measured supermassive black hole samples: consequences for pulsar timing arrays *Mon. Not. R. Astron. Soc.* **463** L6–L11
[359] Shaifullah G *et al* 2016 21 year timing of the black-widow pulsar J2051-0827 *Mon. Not. R. Astron. Soc.* **462** 1029–38
[360] Shannon R M *et al* 2015 Gravitational waves from binary supermassive black holes missing in pulsar observations *Science* **349** 1522–5
[361] Shannon R M *et al* 2016 The disturbance of a millisecond pulsar magnetosphere *Astrophys. J. Suppl. Lett.* **828** L1
[362] Shannon R M and Cordes J M 2010 Assessing the role of spin noise in the precision timing of millisecond pulsars *Astrophys. J.* **725** 1607–19
[363] Shapiro-Albert B J, Hazboun J S, McLaughlin M A and Lam M T 2021 A study in frequency-dependent effects on precision pulsar timing parameters with the pulsar signal simulator *Astrophys. J.* **909** 219
[364] Siemens X, Ellis J, Jenet F and Romano J D 2013 The stochastic background: scaling laws and time to detection for pulsar timing arrays *Class. Quantum Grav.* **30** 224015
[365] Singha J *et al* 2021 Evidence for profile changes in PSR J1713+0747 using the uGMRT *Mon. Not. R. Astron. Soc.* **507** L57–L61
[366] Siwek M S, Kelley L Z and Hernquist L 2020 The effect of differential accretion on the gravitational wave background and the present-day MBH binary population *Mon. Not. R. Astron. Soc.* **498** 537–47
[367] Sorbo L 2011 Parity violation in the cosmic microwave background from a pseudoscalar inflaton *J. Cosmol. Astropart. Phys.* JCAP06(2011)003
[368] Sotiriou T P and Faraoni V 2010 $f(R)$ theories of gravity *Rev. Mod. Phys.* **82** 451–97
[369] Speri L, Porayko N K, Falxa M, Chen S, Gair J R, Sesana A and Taylor S R 2023 Quality over quantity: optimizing pulsar timing array analysis for stochastic and continuous gravitational wave signals *Mon. Not. R. Astron. Soc.* **518** 1802–17
[370] Spiewak R *et al* 2022 The MeerTime Pulsar Timing Array: a census of emission properties and timing potential *Publ. Astron. Soc. Aust.* **39** e027
[371] Springel V *et al* 2005 Simulations of the formation, evolution and clustering of galaxies and quasars *Nature* **435** 629–36
[372] Stamou I and Clesse S 2024 Primordial black holes without fine-tuning from a light stochastic spectator field *Phys. Rev. D* **109** 043522
[373] Stappers B W *et al* 2014 A state change in the missing link binary pulsar system PSR J1023+0038 *Astrophys. J.* **790** 39
[374] Starobinsky A A 1985 Multicomponent de Sitter (inflationary) stages and the generation of perturbations *ZhETF Pisma Redaktsiiu* **42** 124 (available at: https://ui.adsabs.harvard.edu/abs/1985ZhPmR..42..124S)
[375] Starobinsky A A 1979 Spectrum of relict gravitational radiation and the early state of the universe *Sov. J. Exp. Theor. Phys. Lett.* **30** 682 (available at: https://ui.adsabs.harvard.edu/abs/1979JETPL..30..682S)
[376] Starobinsky A A 1986 Stochastic de Sitter (inflationary) stage in the early universe *Field Theory, Quantum Gravity and Strings* vol 246, ed H J de Vega and N Sánchez p 107
[377] Stinebring D, Boriakoff V, Cordes J, Deich W and Wolszczan A 1984 Polarimetry of the two fastest pulsars *Birth and Evolution of Neutron Stars: Issues Raised by Millisecond Pulsars* ed S P Reynolds and D R Stinebring p 32 (available at: https://ui.adsabs.harvard.edu/abs/1984BAAS...16.1010S)
[378] Susarla S C *et al* 2024 Exploring the time variability of the solar wind using LOFAR pulsar data *Astron. Astrophys.* **692** A18
[379] Susobhanan A *et al* 2021 pinta: The uGMRT data processing pipeline for the Indian Pulsar Timing Array *Publ. Astron. Soc. Aust.* **38** e017
[380] Susobhanan A, Gopakumar A, Hobbs G and Taylor S R 2020 Pulsar timing array signals induced by black hole binaries in relativistic eccentric orbits *Phys. Rev. D* **101** 043022
[381] Suwa Y, Yoshida T, Shibata M, Umeda H and Takahashi K 2018 On the minimum mass of neutron stars *Mon. Not. R. Astron. Soc.* **481** 3305–12

[382] Tarafdar P *et al* 2022 The Indian Pulsar Timing Array: first data release *Publ. Astron. Soc. Aust.* **39** e053
[383] Tauris T M *et al* 2017 Formation of double neutron star systems *Astrophys. J.* **846** 170
[384] Taylor J H 1992 Pulsar timing and relativistic gravity *Phil. Trans. R. Soc. A* **341** 117–34
[385] Taylor S R, Lentati L, Babak S, Brem P, Gair J R, Sesana A and Vecchio A 2017 All correlations must die: assessing the significance of a stochastic gravitational-wave background in pulsar timing arrays *Phys. Rev. D* **95** 042002
[386] Taylor S R, Vallisneri M, Ellis J A, Mingarelli C M F, Lazio T J W and Haasteren R 2016 Are We There Yet? Time to Detection of Nanohertz Gravitational Waves Based on Pulsar-timing Array Limits *Astrophys. J. Suppl. Lett.* **819** L6
[387] Taylor S R *et al* 2015 Limits on anisotropy in the nanohertz stochastic gravitational wave background *Phys. Rev. Lett.* **115** 041101
[388] Taylor S R 2022 Nanohertz Gravitational Wave Astronomy 1st edn (CRC Press) pp 172
[389] Taylor S R and Gair J R 2013 Searching for anisotropic gravitational-wave backgrounds using pulsar timing arrays *Phys. Rev. D* **88** 084001
[390] Agazie G *et al* (The International Pulsar Timing Array Collaboration) Comparing recent PTA results on the nanohertz stochastic gravitational wave background (arXiv:2309.00693)
[391] Thorsett S E, Arzoumanian Z, Camilo F and Lyne A G 1999 The triple pulsar system PSR B1620-26 in M4 *Astrophys. J.* **523** 763–70
[392] Tiburzi C, Hobbs G, Kerr M, Coles W A, Dai S, Manchester R N, Possenti A, Shannon R M and You X P 2016 A study of spatial correlations in Pulsar Timing Array data *Mon. Not. R. Astron. Soc.* **455** 4339–50
[393] Tiburzi C *et al* 2019 On the usefulness of existing solar wind models for pulsar timing corrections *Mon. Not. R. Astron. Soc.* **487** 394–408
[394] Tiburzi C *et al* 2021 The impact of solar wind variability on pulsar timing *Astron. Astrophys.* **647** A84
[395] Timokhin A N 2010 A model for nulling and mode changing in pulsars *Mon. Not. R. Astron. Soc.: Lett.* **408** L41–L45
[396] Tomita K 1967 Non-linear theory of gravitational instability in the expanding universe *Prog. Theor. Phys.* **37** 831–46
[397] Tristram M *et al* 2022 Improved limits on the tensor-to-scalar ratio using BICEP and Planck data *Phys. Rev. D* **105** 083524
[398] Tuntsov A V 2014 Dense plasma dispersion of fast radio bursts *Mon. Not. R. Astron. Soc.* **441** L26–L30
[399] Turolla R 2009 Isolated Neutron Stars: The Challenge of Simplicity *Neutron Stars and Pulsars (Astrophysics and Space Science Library)* vol 357, ed W Becker p 141
[400] Vachaspati T and Vilenkin A 1985 Gravitational radiation from cosmic strings *Phys. Rev. D* **31** 3052–8
[401] Vagnozzi S 2021 Implications of the NANOGrav results for inflation *Mon. Not. R. Astron. Soc.* **502** L11–L15
[402] Vallisneri M *et al* 2020 Modeling the uncertainties of Solar System ephemerides for robust gravitational-wave searches with pulsar-timing arrays *Astrophys. J.* **893** 112
[403] van Haasteren R and Levin Y 2013 Understanding and analysing time-correlated stochastic signals in pulsar timing *Mon. Not. R. Astron. Soc.* **428** 1147–59
[404] van Straten W and Bailes M 2011 DSPSR: digital signal processing software for pulsar astronomy *Publ. Astron. Soc. Aust.* **28** 1–14
[405] Vasisht G and Gotthelf E V 1997 The discovery of an anomalous x-ray pulsar in the supernova remnant Kes 73 *Astrophys. J. Suppl. Lett.* **486** L129–32
[406] Verbiest J P W, Osłowski S and Burke-Spolaor S 2021 Pulsar Timing Array Experiments *Handbook of Gravitational Wave Astronomy* ed C Bambi S Katsanevas K D Kokkotas p 4
[407] Verbiest J P W *et al* 2016 The International Pulsar Timing Array: first data release *Mon. Not. R. Astron. Soc.* **458** 1267–88
[408] Verbiest J P W and Shaifullah G M 2018 Measurement uncertainty in pulsar timing array experiments *Class. Quantum Grav.* **35** 133001
[409] Verbiest J P W, Vigeland S J, Porayko N K, Chen S and Reardon D J 2024 Status report on global pulsar-timing-array efforts to detect gravitational waves *Results Phys.* **61** 107719
[410] Vilenkin A and Shellard E P S 2000 *Cosmic Strings and Other Topological Defects* (Cambridge University Press) (available at: https://ui.adsabs.harvard.edu/abs/2000csot.book.....V)

[411] Vilenkin A 1981 Gravitational field of vacuum domain walls and strings *Phys. Rev. D* **23** 852–7
[412] Vilenkin A 1981 Gravitational radiation from cosmic strings *Phys. Lett. B* **107** 47–50
[413] Wang J-C, Yuwen Z-Y, Hao Y-S and Wang S-J 2024 General bubble expansion at strong coupling *Phys. Rev. D* **109** 096012
[414] Wang S Q *et al* 2021 Unusual emission variations near the eclipse of black widow pulsar PSR J1720-0533 *Astrophys. J. Suppl. Lett.* **922** L13
[415] Wang S and Zhao Z-C 2024 Unveiling the graviton mass bounds through the analysis of 2023 Pulsar Timing Array data releases *Phys. Rev. D* **109** L061502
[416] Wang S, Zhao Z-C and Zhu Q -H 2024 Constraints on scalar-induced gravitational waves up to third order from a joint analysis of BBN, CMB and PTA data *Phys. Rev. Res.* **6** 013207
[417] Wang S, Zhao Z-C, Li J-P and Zhu Q -H 2024 Implications of Pulsar Timing Array data for scalar-induced gravitational waves and primordial black holes: Primordial non-Gaussianity f_NL considered *Phys. Rev. Res.* **6** L012060
[418] Weatherall J C 1998 Pulsar radio emission by soliton collapse in strong plasma turbulence *Astrophys. J.* **506** 341
[419] Weltevrede P, Edwards R T and Stappers B W 2006 The subpulse modulation properties of pulsars at 21 cm *Astron. Astrophys.* **445** 243–72
[420] Witten E 1984 Cosmic separation of phases *Phys. Rev. D* **30** 272–85
[421] Wu Y-M, Chen Z-C, Bi Y-C and Huang Q -G 2024 Constraining the graviton mass with the NANOGrav 15 year data set *Class. Quantum Grav.* **41** 075002
[422] Xu H *et al* 2021 A sustained pulse shape change in PSR J1713+0747 possibly associated with timing and DM events *Astron. Teleg.* **14642** 1 (available at: https://ui.adsabs.harvard.edu/abs/2021ATel14642....1X)
[423] Xu H *et al* 2023 Searching for the nano-hertz stochastic gravitational wave background with the Chinese pulsar timing array data release I *Res. Astron. Astrophys.* **23** 075024
[424] Xue X *et al* 2024 First pulsar polarization array limits on ultralight axion-like dark matter (arXiv:2412.02229)
[425] Xue X *et al* 2022 High-precision search for dark photon dark matter with the Parkes Pulsar Timing Array *Phys. Rev. Res.* **4** L012022
[426] You X P, Hobbs G B, Coles W A, Manchester R N and Han J L 2007 An improved solar wind electron density model for pulsar timing *Astrophys. J.* **671** 907–911
[427] Young S, Musco I and Byrnes C T 2019 Primordial black hole formation and abundance: contribution from the non-linear relation between the density and curvature perturbation *J. Cosmol. Astropart. Phys.* JCAP11(2019)012
[428] Yunes N and Siemens X 2013 Gravitational-wave tests of general relativity with ground-based detectors and pulsar-timing arrays *Living Rev. Relativ.* **16** 9
[429] Zheng H, Gao F, Bian L, Qin S and Liu Y 2025 Quantitative analysis of the gravitational wave spectrum sourced from a first-order chiral phase transition of QCD *Phys. Rev. D* **111** l021303
[430] Zhu M, Ye G and Cai Y 2023 Pulsar timing array observations as possible hints for nonsingular cosmology *Eur. Phys. J. C* **83** 816
[431] Zhu W W *et al* 2019 Tests of gravitational symmetries with pulsar binary J1713+0747 *Mon. Not. R. Astron. Soc.* **482** 3249–60
[432] Zic A *et al* 2022 Evaluating the prevalence of spurious correlations in Pulsar Timing Array data sets *Mon. Not. R. Astron. Soc.* **516** 410–20
[433] Zic A *et al* 2023 The Parkes Pulsar Timing Array third data release *Publ. Astron. Soc. Aust.* **40** e049